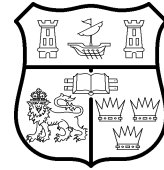


Title	Optically injected multi-mode semiconductor lasers
Authors	O'Shea, David
Publication date	2016
Original Citation	O'Shea, D. 2016. Optically injected multi-mode semiconductor lasers. PhD Thesis, University College Cork.
Type of publication	Doctoral thesis
Rights	© 2016, David O' Shea. - <a href="http://creativecommons.org/licenses/by-nc-nd/3.0/">http://creativecommons.org/licenses/by-nc-nd/3.0/</a>
Download date	2024-04-24 15:51:38
Item downloaded from	<a href="https://hdl.handle.net/10468/3096">https://hdl.handle.net/10468/3096</a>



# Optically Injected Multi-mode Semiconductor Lasers

David O' Shea  
BSc  
108349100



NATIONAL UNIVERSITY OF IRELAND, CORK  
DEPARTMENT OF APPLIED MATHEMATICS

**Thesis submitted for the degree of  
Doctor of Philosophy**

January 2016

Head of Department: Prof Sebastian Wieczorek

Supervisor: Dr Andreas Amann

Research supported by Irish Research Council

# Contents

List of Figures . . . . .	iii
List of Tables . . . . .	viii
Acknowledgements . . . . .	x
Abstract . . . . .	xi
<b>Publications</b>	<b>1</b>
<b>1 Introduction</b>	<b>1</b>
1.1 General Introduction . . . . .	1
1.2 Laser Types . . . . .	2
1.2.1 Use of Laser Devices in Society . . . . .	3
1.3 Historical Context . . . . .	4
<b>2 Background to the problem</b>	<b>7</b>
2.1 Derivation of Rate-equation model for Two-mode Laser . . . . .	7
2.1.1 Energy Transitions of an atom between states. . . . .	7
2.1.1.1 Stimulated Emission . . . . .	7
2.1.1.2 Stimulated Absorption . . . . .	9
2.1.1.3 Spontaneous Emission . . . . .	9
2.1.1.4 Relation of Einstein Coefficients. . . . .	10
2.2 Semi-classical Laser Theory . . . . .	11
2.2.1 Maxwell-Bloch . . . . .	17
2.2.2 Non-linear Gain Derivation. . . . .	23
2.2.3 Assembling the pieces . . . . .	29
2.2.4 Discussion of parameters . . . . .	31
2.2.4.1 $\alpha$ : Line width enhancement factor. . . . .	31
2.2.4.2 T . . . . .	31
2.2.4.3 P . . . . .	31
2.2.4.4 $\epsilon$ : gain compression factor . . . . .	32
2.3 Bifurcations and dynamical phenomena . . . . .	33
2.3.1 Transcritical Bifurcation . . . . .	35
2.3.2 Pitchfork Bifurcation . . . . .	37
2.3.2.1 Supercritical . . . . .	37
2.3.2.2 Subcritical . . . . .	37
2.4 Literature Review . . . . .	40
2.4.1 Theoretical Models . . . . .	40
2.4.2 Experimental Mapping Techniques . . . . .	43
2.4.3 Optical Rogue Waves . . . . .	44
<b>3 Dynamical classification of optically injected lasers</b>	<b>47</b>
3.1 Motivation . . . . .	48
3.2 Introduction . . . . .	49
3.3 Outline of experiment . . . . .	49
3.3.1 Measuring Threshold and Temperature Selection . . . . .	52
3.3.2 Free Space Optics . . . . .	54

3.3.3	Measuring Detuning . . . . .	54
3.4	Data Collection and Inspection . . . . .	55
3.4.1	Mean and Standard Deviation Thresholds . . . . .	57
3.5	State Identification . . . . .	64
3.6	Experimental Stability Diagram . . . . .	65
3.7	Lyapunov Exponents . . . . .	66
3.8	Single Mode Stability Analysis . . . . .	69
3.9	Lower $P$ . . . . .	70
3.10	Optical Bi-stability . . . . .	70
3.11	Conclusion . . . . .	75
<b>4</b>	<b>Origins of abnormally large 'Rogue Waves' in optically injected lasers.</b>	<b>76</b>
4.1	Background . . . . .	76
4.2	Model Comparison . . . . .	77
4.2.1	Dimensionless model . . . . .	77
4.2.2	Bifurcation Diagram . . . . .	79
4.3	Time-Trace Analysis . . . . .	81
4.4	Rogue Wave Mean-Time . . . . .	83
4.5	Rogue Wave Comparison . . . . .	85
4.6	Chimney and Spike Structure . . . . .	88
4.7	Poincaré Map . . . . .	91
4.7.1	Maximum $N$ Poincaré Section . . . . .	93
4.8	Fast-Slow Dynamics . . . . .	98
4.8.1	Slow Manifold . . . . .	98
4.9	Rogue Wave Dynamics in Two-Mode Laser . . . . .	103
4.9.1	$\epsilon = 0.01$ . . . . .	103
4.10	Effect of Small Additive Noise on Rogue Wave Occurrence . . . . .	105
4.11	Summary/Conclusion . . . . .	110
<b>5</b>	<b>Conclusion</b>	<b>111</b>
5.1	Future Work . . . . .	112
<b>Appendices</b>		<b>114</b>
<b>A</b>	<b>Dynamical Classification of Optically Injected Lasers</b>	<b>115</b>
A.1	Additional Plots:Bi-stability Analysis . . . . .	115
<b>B</b>	<b>Rogue Wave Analysis</b>	<b>117</b>
B.1	Source Code . . . . .	117
B.1.1	RW Integrator. . . . .	117
B.2	Python Code . . . . .	124
B.2.1	<code>do_process_data.py</code> . . . . .	124
B.3	Relation between $\Delta\omega$ and $\Delta\nu$ . . . . .	131

## List of Figures

2.1	Two-level laser system:(a) Atom is excited to an above-ground state energy level $E_1$ . (b) A photon with energy $h\nu = \Delta E$ is incident on the excited atom, relaxing the atom into the ground state. (c): The relaxing atom emits a second photon with energy of $h\nu = \Delta E$ and decays to the ground state. . . . .	8
2.2	Two-level laser system:(a) Atom is unexcited and in the ground state energy level $E_0$ . (b) A photon with energy $h\nu = \Delta E$ is incident on the excited atom, exciting the atom with exactly an energy of $\Delta E$ . (c): The excited atom is now in the above-ground state. The incident photon has been absorbed. . . . .	9
2.3	Two-level laser system:(a) Atom is in the higher energy level $E_1$ . (b) The atom spontaneously decays releasing a photon with energy $h\nu = \Delta E$ . (c): The atom is now in the ground state and the a photon travels off in a random spatial direction. . . . .	10
2.4	Cartoon of material gain due to population inversion of two-mode laser. . . . .	24
2.5	Three discrete states are available with six possible transitions between them: $N_1$ , $N_2$ and $N_3$ . Electron-hole pairs can move from state X to Y with a transition probability $T_{YX}$ . Electron-hole pairs in $N_1$ and $N_2$ also have a certain lasing rate. . . . .	25
2.6	Black arrows denote direction of flow of system, red circles denote fixed points of the system. . . . .	33
2.7	Shown are various trajectories of $N$ , depending on initial conditions. The legend on the right states the initial condition for each trajectory. . . . .	34
2.8	Phase portrait for $\dot{I}$ vs. $I$ . a) $N_0 < \frac{k}{G}$ b) $N_0 = \frac{k}{G}$ and c) $N_0 > \frac{k}{G}$ . Physically, a negative intensity (number of photons) is meaningless, but is included here to account for the stability exchange as $N_0$ is varied. The fixed points are marked with circles and their stability is noted with a solid red (stable), empty circle (unstable) or half-stable (half-fill). . . . .	35
2.9	[84, p.55]For $N_0 < \frac{k}{G}$ , the emitted photons behave like a lamp with a zero average intensity. At $N_c$ , the stable fixed point becomes non-zero due to the transcritical bifurcation. The arrows indicate the flow of the system, which is 'attracted' towards stable points. When a qualitative change occurs due to a variation of the control parameter, a bifurcation is said to have occurred. . . . .	36
2.10	Phase portrait with fixed points (and their stability indicated using the standard notation) as the control parameter $r$ is varied: a) $r < 0$ b) $r = 0$ and c) $r > 0$ respectively. . . . .	38

2.11	Bifurcation diagram for the pitchfork bifurcation. At $r = r_c = 0$ (critical value of $r$ , and is zero in the normalised form) a pitchfork bifurcation occurs and two stable non-zero fixed points occur. The previously stable fixed point at 0 is now unstable. The arrows indicate the flow of system and a qualitative change occurs at $r_c$ indicating the bifurcation has occurred. . . . .	38
2.12	Phase portrait with fixed points (and their stability indicated using the standard notation) as the control parameter $r$ is varied: a) $r < 0$ b) $r = 0$ and c) $r > 0$ respectively. . . . .	39
3.1	Diagram of Experiment: . . . . .	50
3.2	Optical Spectra of (a) Single-Mode and (b) Two-Mode laser . .	51
3.3	Threshold Current (Blue) and Two-Colour Point Current (Green) measured as the temperature is varied. The measurements were taken over the course of a day, providing the semiconductor laser ample time to stabilise after a temperature change. . . . .	53
3.4	Plot of $P$ versus temperature. The dashed line indicates how the temperature was selected to ensure a $P$ value of 0.5. . . . .	53
3.5	a) Recorded $K^2$ (injection strength) with fitted sine curve (white). b) Fitted $K$ . c) Sample time-trace at +2.7GHz detuning. The red and green vertical lines indicate the locations of the local maxima and minima of $K$ respectively. . . . .	56
3.6	a) - c): Experimentally recorded $K^2$ , fitted $K$ and experimentally recorded $ E ^2$ for the first upward sweep in $K^2$ . d) - f): Experimentally recorded $K^2$ , fitted $K$ and experimentally recorded $ E ^2$ for the first downward sweep in $K^2$ . . . . .	57
3.7	Experimentally measured average (top row) and standard deviation (bottom row) of injected (left column) and uninjected (right column) modes in the $K$ - $\Delta\omega$ plane. . . . .	59
3.8	a) Mean threshold for uninjected mode and b) Standard deviation threshold for Injected mode. Time trace from several different $\Delta\omega$ are plotted as a single threshold is used for the full two-dimensional plane. . . . .	60
3.9	Mean and Standard Deviation plots of two-dimensional sweep .	61
3.10	a) Hamming Window. b) FFT of Hamming Window. . . . .	61
3.11	Number of peaks present in the FFT of the experimentally obtained time traces as a function of $K$ and $\Delta\omega$ . . . . .	62
3.12	Top row: Sample time traces for various values of $K$ at $\Delta\omega = +2.7$ GHz. Bottom Row: FFT of time traces in Top Row, with detected peaks indicated by full circles. Colour fill represent the identified state as explained in the main text. The red dashed line indicates the intensity threshold used for peak detection. FFTs are shown on a log scale. . . . .	63
3.13	Automatically coloured Time-trace . . . . .	65

3.14 Left panels: experimental stability diagrams for the Two Mode laser at $P=0.5$ (upper) and the Single Mode laser at $P=0.5$ (lower). Right panels: corresponding theoretical stability diagrams based on numerical time-traces and Lyapunov exponents. Light (dark) colours indicate Two Mode (Single Mode) dynamics. Stable Fixed point (FP) states are green, stable limit cycles (LC) are grey, stable tori (TR) are blue and chaotic (CH) states are yellow and red.	66
3.15 Lyapunov Exponent diagram: An initial point $d_0$ is integrated forward to $d_0(t)$ . The initial point is perturbed by a small influence and ends up on black sphere. The sphere is integrated forward in time and maps onto the ellipse. The rates of stretching/compressing of the radii of the sphere/ellipse are the Lyapunov Exponents of the $E_{Re}, E_{Im}$ and $n$ dimensions respectively. If any of the Lyapunov Exponents are positive, the system is said to be chaotic as two trajectories, initially close, will diverge in finite time. . . . .	68
3.16 Left panel: Experimental stability diagram for the Two Mode laser at $P = 0.2$ . Lower panel: Theoretical stability diagram for the Two Mode laser at $P = 0.2$ . Locked, unlocked and complex dynamical states are identified using the same colour scheme as the Two Mode and Single Mode $P = 0.5$ configurations. . . . .	69
3.17 <b>a)</b> : Plot of the mean of $ E ^2$ as $K$ is increasing (blue) and decreasing (green). <b>b)</b> : Plot of the difference (subtracted) between the upward and downward means. . . . .	71
3.18 <b>a)</b> Corrected $K$ fit for $+2.75\text{GHz}$ detuning showing a much improved overlap. <b>b)</b> Plot of the difference (subtracted) between the upward and downward means showing no bi-stability at this $\Delta\omega$ .	72
3.19 <b>a)</b> Corrected $K$ fit for $-7\text{GHz}$ detuning showing a much improved overlap. <b>b)</b> Shows a correctly identified bi-stability using the difference of the corrected means. . . . .	73
3.20 A large bi-stability region is detected for negative detuning. This bistability occurs in the injected mode. . . . .	73
3.21 Combination of results of the bi-stability analysis for both the injected (left column) and uninjected mode (right column), as $K$ is swept upwards (top row) and downwards (middle row). The bi-stabilities detected are shown in the bottom row. . . . .	74
3.22 Numerical simulation of Bi-stability . . . . .	75
4.1 One-dimensional bifurcation diagram. The sweep is performed for varied $P$ . The vertical red line indicates the $P$ used for this investigation. Plotted along the y-axis are the local maxima found at a particular $P$ . . . . .	80
4.2 Histogram of $ E ^2$ time-trace. The RW limit (dashed red line) was calculated using Eq. 4.18 . . . . .	82
4.3 Time-trace segment of $ E ^2$ (Blue) with an optical rogue-wave event in (Red dot). The red dashed line indicates the RW-Limit. . . . .	82

4.4	Time-trace plot indicting the detection of RW events. 200 separate RW events were detected after integrating the system for $2.2 \times 10^6 ns$ ( $\approx 1.3 \times 10^{10}$ steps with a time-step of 0.1). . . . .	84
4.5	Histogram of time-between RW events. Blue bars are the binned observations. The green line is the least-squares fit of the Exponential Distribution. An error of the square-root of the numerical observation is assumed to be sufficient. The vertical red dashed line indicates the average time between observed events. . . . .	84
4.6	Time series of 4 RW events are plotted, aligned at the RW event. Plot of: <b>a)</b> $ E ^2$ in a log scale. <b>b)</b> $N$ (scaled $\times 30$ to make features clearer). <b>c)</b> Phase of $ E $ . A black dashed line at $2ns$ before the RW event and a dashed green line is used to indicate the time of the RW events. . . . .	86
4.7	3-D Chimney-Spike (green, blue respectively) structure with time-series ending with RW event (red). . . . .	90
4.8	Poincaré Mapping of $\theta = -\frac{\pi}{4}$ . The colour-bar indicates the number of times a point on the time-trace will have before an RW event. The circular points are the intersections of a sample time-trace with the map. . . . .	92
4.9	Saddle: $n = 0.41792$ . The red trace beginning (in forward time) at the green point will eventually lead to the red point (saddle). The green structure is the chimney which is shown to close near $n = P$ . The blue structure is the spike which is shown to become quite narrow near $n = P$ . . . . .	95
4.10	Saddle: $n = -0.00584$ . The red trace beginning (in forward time) at the green point will eventually lead to the red point (saddle). The blue structure is the spike which is shown to become quite narrow near $n = P$ . . . . .	96
4.11	Saddle: $n = 0.00245$ . The red trace beginning (in forward time) at the green point will eventually lead to the red point (saddle). The blue structure is the spike which is shown to become quite narrow near $n = P$ . . . . .	97
4.12	Combined figure of Slow Manifold (Blue), RW time-series and event (Red) and path to Saddle point (Green) . . . . .	99
4.13	Spike-structure, Chimney-structure and Slow-Manifold. . . . .	100
4.14	Plot of $\dot{N}$ against $N$ . The plot is coloured according to the sign of $\dot{N}$ . . . . .	102
4.15	Chimney coloured according to height in $N$ achieved. The highest 25% are shaded orange. The largest $N$ is shaded red. . . . .	103
4.16	One-dimensional bifurcation2 diagram of $E_2$ for the Two-Mode Laser. The sweep is performed over a varied $P$ . The red vertical line indicates the chosen $P$ for this investigation. . . . .	104
4.17	Integration of Two mode laser at for the same parameter space as the single mode laser. Top panel: $ E_1 ^2$ (uninjected mode). Bottom panel: $ E_2 ^2$ (injected mode) . . . . .	105

4.18 Poisson fit to mean-time between rogue waves. Small additive noise of the order of $10^{-5}$ has been added to the $Re$ at each integration step . . . . .	106
4.19 Poisson fit to mean-time between rogue waves. Small additive noise of the order of $10^{-4}$ has been added to the $E_{Real}$ at each integration step . . . . .	107
4.20 Poisson fit to mean-time between rogue waves. Small additive noise of the order of $10^{-3}$ has been added to the $E_{Real}$ at each integration step . . . . .	108
4.21 Mean-time between RW events versus noise . . . . .	108
A.1 No random noise for integration. Note that at 15000 ps the uninjected mode does not become non-zero. . . . .	116

## List of Tables

3.1	Table listing frequency detuning (GHz) and the corresponding wavelengths (nm) of the master laser. . . . .	55
3.2	State colour definitions, based on if the Mean (Mn) or Standard Deviation (SD) is Large (L) or Small (S) and the number of peaks detected in the injected mode. . . . .	63

I, David O' Shea, certify that this thesis is my own work and I have not obtained a degree in this university or elsewhere on the basis of the work submitted in this thesis.

*David O' Shea*

## Acknowledgements

Over the past 7 years I have come to befriend many people in UCC and in Tyndall National Institute, all who have contributed in some way to my experience and ultimately this thesis. If you are not mentioned by name, please see this as a failing on my part (absent-mindedness) and not yours. So in reverse-chronological order...

Firstly I would like to thank my supervisor, Dr Andreas Amann, for initially granting me an internship four years ago that evolved in this PhD. For his patience, advice and open-door policy during the time I have been fortunate to work with him and his methodological approach to problem solving that I have attempted to follow in the completion of this thesis.

I would like to thank Dr. Simon Osborne for his assistance with the experimental aspects of this thesis and Dr. David Goulding and Dr Bryan Kelleher for the many fruitful discussions on optically injected lasers.

To Prof Eoin O Reilly and Photonics (formerly PTG), Prof. Sebastian Wieczorek and School of Applied Mathematics researchers and administrators, thank you for the opportunity to work in such distinguished centres and for the everyday support you provided.

To my friends and colleagues who have in some form allowed themselves to be proof readers, even not by their own volition.

This project was funded by the Irish Research Council, without whom the possibility of pursuing a PhD would have been immeasurably difficult, if not possible at all.

## Abstract

As a device, the laser is an elegant conglomerate of elementary physical theories and state-of-the-art techniques ranging from quantum mechanics, thermal and statistical physics, material growth and non-linear mathematics. The laser has been a commercial success in medicine and telecommunication while driving the development of highly optimised devices specifically designed for a plethora of uses. Due to their low-cost and large-scale predictability many aspects of modern life would not function without the lasers. However, the laser is also a window into a system that is strongly emulated by non-linear mathematical systems and are an exceptional apparatus in the development of non-linear dynamics and is often used in the teaching of non-trivial mathematics. While single-mode semiconductor lasers have been well studied, a unified comparison of single and two-mode lasers is still needed to extend the knowledge of semiconductor lasers, as well as testing the limits of current model. Secondly, this work aims to utilise the optically injected semiconductor laser as a tool so study non-linear phenomena in other fields of study, namely 'Rogue waves' that have been previously witnessed in oceanography and are suspected as having non-linear origins. The first half of this thesis includes a reliable and fast technique to categorise the dynamical state of optically injected two mode and single mode lasers. Analysis of the experimentally obtained time-traces revealed regions of various dynamics and allowed the automatic identification of their respective stability. The impact of this method is also extended to the detection regions containing bi-stabilities. The second half of the thesis presents an investigation into the origins of Rogue Waves in single mode lasers. After confirming their existence in single mode lasers, their distribution in time and sudden appearance in the time-series is studied to justify their name. An examination is also performed into the existence of paths that make Rogue Waves possible and the impact of noise on their distribution is also studied.

# Publications

## Published Papers

- D. O' Shea, S. Osborne, N. Blackbeard, D. Goulding, B. Kelleher, A. Amann "Experimental classification of dynamical regimes in optically injected lasers." Optics Express 22 (18), 21701-21710

## Poster Presentations

- D. O' Shea, S. Osborne, N. Blackbeard, S. O' Brien, A. Amann "Bursting in an Optically Injected Two-Mode Laser: The Cusp-Pitchfork Bifurcation." CLEO, Munich, 2013
- D. O' Shea, S. Osborne, N. Blackbeard, B. Kellher, D. Goulding, A. Amann "Experimentally mapping the bifurcations of an optically injected laser." Photonics Ireland, Belfast, 2013

## Conference Papers

- Global Bifurcations Lead to Bursting in a Two-Mode Laser , SIAM Conference on Applications of Dynamical Systems, Snowbird, USA, 2013

## Talks

- Experimental classification of dynamical regimes in optically injected lasers, SIAM (Society for Industrial and Applied Mathematics) 2014, National University of Ireland, Galway.

# Chapter 1

## Introduction

### 1.1 General Introduction

Since the invention of Differential Calculus in the mid 17<sup>th</sup> century (somewhat co-dependently/independently by Sir Issac Newton and Gottfried Leibniz), the division between mathematics and the physical sciences has become blurred. It could be argued that, in this ambiguous area, the field of Applied Mathematics was first forged when the rigorous abstract concepts of 'pure mathematics' became entwined with the curiosities of the physical world.

Historically, applied mathematics has been a mix of mathematical sciences and specialised knowledge that is used in formulating and studying mathematical models in a plethora of related disciplines. Computer science, material physics, financial and actuarial sciences, population dynamics, laser physics, and computational biology are just a few of the disciplines that have emerged. They have been inspired by unavoidably interesting, real-world problems that at their core are governed by the seemingly abstract yet indisputable axioms of mathematics.

The story of the laser began in a 1917 as a physics paper by Einstein on spontaneous and stimulated emission [18]. It has evolved over the last century to become a problem of deep interest to applied mathematics as controllable, isolated, simple (straightforward in experimental setup) device that exhibits non-linear, complex behaviour that is accurately reproduced by the rate-equation model [94, 64]. The current state of the research allows for two directions of expansion: an experimental/theoretical study that analyses the semiconductor lasers regardless of the device type/number of modes [68], and the use of a semiconductor laser as a test-bed for dynamical systems theory [8]

The topic of this thesis is therefore two-fold, firstly to extend and further validate the appropriateness of the multi-mode model for single and two mode lasers

using experimentally observed data and numerical computations, and secondly, to utilise the laser itself as a window into an isolated, non-linear dynamical system for testing and verification of mathematical theories that have been formed for noisy and externally influenced systems.

Traditionally, lasers have been a test-bed for new physical theories since their experimental demonstration by Maiman [54]. The device itself, is experimental validation of several fundamental concepts beginning most notably with Einstein's work on spontaneous and stimulated emission [18] and Boson Statistics.

However, it is not sufficient to merely confirm the basic characteristics of light-matter interactions. To construct a laser, one needs to avail of leading technological achievements including growth methods to produce low-defect gain media. A quality gain media is required to provide a population-inversion where excited molecules would be continuously destabilised into emitting additional photons and re-excited by an external pump mechanism. The pump mechanism can be either optical (optical injection) or electrical (current). To achieve a population inversion in a 'cheap' way via pumping required multi-level atomic systems and took almost 30 years to achieve after Einstein's initial prediction. Since then, different types of lasers have emerged and can be categorised based on several of their structural properties, including the gain material used and the direction of propagation of the beam relative to the cavity.

## 1.2 Laser Types

From a purely fundamental view point, all lasers make use of the same basic underlying principles (population inversion of a many-state atomic/semiconductor/gas gain medium via pumping). However, lasers types can be subdivided based upon the type of gain medium utilised, operational lasing wavelength, number of wavelengths emitted and direction of light propagation (perpendicular/parallel to top surface). These categories can again be subdivided, but only an overview of the laser types will presented here.

The first functioning laser had a three-level ruby rod gain medium and operated in the deep red region ( $694.3\text{nm}$ ) [54]. The first gas laser invented in the following year [39] consisted of a Helium–neon gain medium.

### **Laser-Diode**

A laser-diode is an electrically (or optically) pumped semi-conductor laser that utilises a p-n junction as the gain medium. Many of everyday electronic devices

today that use a laser, will more often than not be a laser-diode.

## VCSEL vs Edge Emitting

Vertical-Cavity Surface-Emitting Laser(VCSEL) is a sub-group of laser diodes. These lasers can be tested at many points in the manufacturing process for correctness and usability of the device (unlike Edge-emitting). As VCSELs emit light from the top surface, thousands of VCSELs can be processed simultaneously from a single wafer.

A VCSEL has the optical cavity parallel to the direction of current flow, unlike Edge-Emitting lasers which have the optical cavity perpendicular to the current flow.

Edge-Emitting laser diodes can only be tested at the end of the manufacturing process. Therefore if any of the intermediate manufacturing steps fail (bad contacts, material growth, processing time, growing time etc), resources can be wasted unknowingly. Edge-Emitting lasers are the original form of the semiconductor laser, and are still widely used.

### 1.2.1 Use of Laser Devices in Society

Optically injected lasers have been the source of considerable interest and use in telecommunications since their creation as low powered, fast, small and efficient data communication devices [12, 69, 33]. With the ever evolving demand for data driven telecommunication and internet services, the semiconductor laser has been adapted for numerous uses already (CD/DVD players) in the drive towards environmentally conscious and energy-efficient photonics and away from their heat generating electronic counterparts.

Simultaneously, in applied mathematics the semiconductor laser has been of substantial interest as it has been shown to strongly emulate the properties of low-order, multidimensional, non-dimensionalized, complex, non-linear, coupled, time-dependant, first-order differential equations [97], and therefore a practical application of some of the more abstract areas of mathematics [98, 66]. The non-linear and chaotic behaviour of semiconductor lasers was first reported over 20 years ago and initially was of little interest and considered a nuisance. It is now well known to be a fundamental consequence of non-linear dynamics [44]. Since then the chaotic dynamics of lasers has found many areas of application including cryptography [13, 89, 57] and random number generation.

The subject of this thesis is optical injection of multi-mode semiconductor

lasers, and this allows for a broad and thorough study of single-mode and two-mode devices using numerous applied mathematical methods including: dynamical systems theory, time-series analysis, bifurcation theory, and stability analysis.

The main goals of this study are to analyse devices with different number of active modes [68] and to use these devices as tools to study dynamical phenomena in other areas such as 'Rogue Waves' in oceanography [8, 4, 82].

The next section places my work in historical context (Sec. 1.3). Chapter 2 provides some specific background information on the problem along with some required derivations of the multi-mode semiconductor laser model. Chapter 3 introduces the work previously published in Optics Express [68], with particular emphasis on the numerical and experimental comparison of single-mode and two-mode lasers. Additionally, previously unpublished work on the bi-stability analysis of two-mode lasers is also included. Chapter 4 discusses the applications of optically injected lasers as a test-bed for the dynamical theory in other fields, particularly in discussing the origins of 'Rogue Waves' that were originally observed in oceanography. Finally Chapter 5 provides a conclusion of the thesis and an outlook of future research directions.

### 1.3 Historical Context

Almost a century has passed since Einstein presented his theory of spontaneous and stimulated emission and emission of electromagnetic radiation [18] in 1917, which was the first step towards the invention of the laser. However it was thirty years later before the idea of using stimulated emission to amplify electromagnetic radiation make significant progress [32, 90]. In a close race Gorden et al. achieved the first ammonia MASER (Microwave Amplification by Stimulated Emission of Radiation). As the name implies, this device operated in the microwave range, and soon afterwards an extension to the MASER was delivered by Schawlow and Townes [76]. In Schawlow et al. [76] they suggested that the MASER can be made to operate in the visible and infrared part of the spectrum. However it was not until Maiman et al. [54] used a ruby gain medium that Light Amplification by Stimulated Emission of Radiation (LASER) was observed. This was the birth of the laser.

Since then, lasers have been refined and optimised to exhibit specific properties for a copious number of uses, all following a primary and fundamental goal: to produce a coherent light source (within the context of the specific application). For example, in the use for telecommunications, a coherent light source in the

$1500\text{nm}$  range is needed. Ideally the lasers have stable operation at room temperature (that is, in the absence of temperature control). The  $1500\text{nm}$  range is required as the currently employed optical fibres are made from silica, which is a cheap and reasonably flexible medium which has the lowest loss at  $1500\text{nm}$ .

It has been shown [31] that GaAs (Gallium arsenide) lasers operate predominately in the TE (Transverse-Electric) mode. The lasers studied in this thesis (and employed in telecommunications) are made from GaAs and InGaAs alloys that retain this property.

Soon after the inception of the laser, books on the theory of laser physics [75, 55, 84] were published for use as educational tools as the interest in lasers (and more specifically, semi-conductor lasers) grew. As theoretical models were developed to explain the complex, non-trivial laser behaviour, an interesting comparison was drawn by Haken [34] between the single-mode laser system and the famous atmospheric model studied by Lorenz [53]. This comparison predicted that multi-mode lasers could also become chaotic and reconciled experimental observations of complex dynamics with sensitivity to initial conditions [6, 91, 14].

Building upon this confirmation of chaotic dynamics, the interest in semi-conductor lasers for applied mathematics grew enormously. This is because the laser presented a device that was already of important use to engineers and physicists, but also provided an opportunity to demonstrate mathematical objects, such as bifurcations in a system that can be studied in isolation (compared to the examples of meteorological and financial markets that cannot account for all external influences). Therefore, many experiments and real-world validation of mathematical models can be performed with pre-existing infrastructure and technology (motivating the latter aspect of this thesis).

Thorough single-mode semiconductor laser studies have been conducted [93, 94, 95, 96, 97] and the single-mode laser is considered to be a well-known system, involving many experimental measurements of mathematical objects and predictions [67, 36, 60, 59, 11]. However, these works leave room for a comprehensive multi-mode (a two-mode laser is utilised in this thesis) comparison with the single-mode theory (motivating the former part of my thesis). Already it has been confirmed that there are additional structures present in two-mode devices, using a low order, coupled differential system of equations [66]. The system of ODE's for a multi-mode laser will be derived in Chap. 2.2. As a result of these additional structures, new applications of semiconductor lasers have been found, such as bi-stability and wavelength switching [67].

In the next chapter, the derivation of the rate equation model of the multi-

mode lasers is introduced, beginning with energy transition between a two-state atomic system and ending with semi-classical laser theory. The intermediate sections include a master equation approach to the gain derivation and Maxwell Bloch equations for a semi-conductor gain material.

# Chapter 2

## Background to the problem

### 2.1 Derivation of Rate-equation model for Two-mode Laser

In this chapter the model and application of multi-mode semiconductor lasers is introduced through the derivation of a rate equation model. The desired rate equation model should be a simple system of ordinary differential equations (ODE's) which will be studied in later parts. The derivation will be semi-classical in nature, and is designed to extend the current and experimentally validated model for lasers with a single longitudinal mode[80], where mode selection occurs as a consequence of the cavity length. For simplicity, I will first introduce an atomic model which is similar to a semiconductor laser model if the details of the gain medium can be neglected. As a laser operates on the basis of stimulated emission, it is natural to begin the introduction of lasers with a discussion on quantised energy transitions.

#### 2.1.1 Energy Transitions of an atom between states.

When discussing photons and their interaction with matter one must acknowledge the revolutionary foundations laid by Einstein[18], namely that given an atom with two discrete energy levels, there are three possible transitions between these energy levels: stimulated emission, stimulated absorption and spontaneous emission.

##### 2.1.1.1 Stimulated Emission

Stimulated emission was first predicted by Einstein in 1917[18] and later confirmed experimentally by Ladenburg[47] after 11 years when technology had ad-

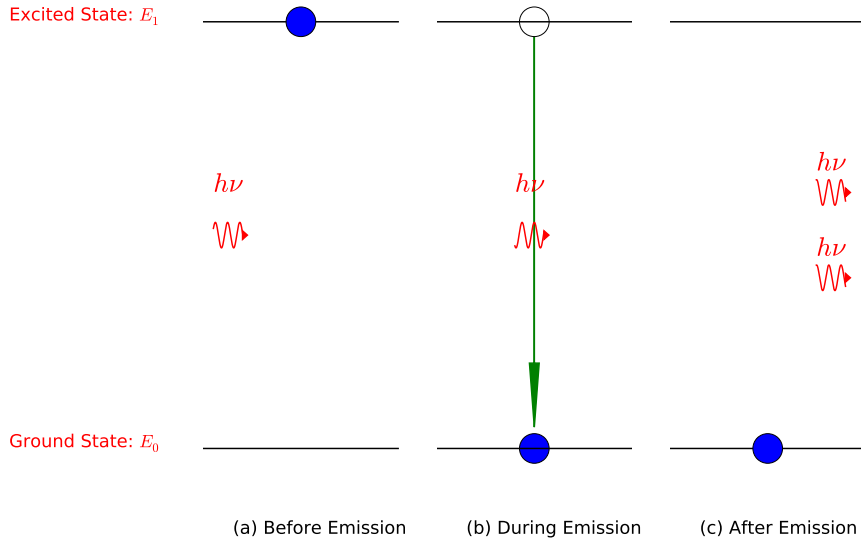


Figure 2.1: Two-level laser system:(a) Atom is excited to an above-ground state energy level  $E_1$ . (b) A photon with energy  $h\nu = \Delta E$  is incident on the excited atom, relaxing the atom into the ground state. (c): The relaxing atom emits a second photon with energy of  $h\nu = \Delta E$  and decays to the ground state.

vanced far enough. In his paper Einstein hypothesised that an excited atom can be *destabilised* by an incident photon and emit a second photon of identical energy.

Let us consider an atom with two discrete energy levels  $E_0$  (ground state) and  $E_1$  (excited state) with energy difference ( $\Delta E$ )  $E_1 - E_0 = \Delta E = h\nu$ , and  $E_1 > E_0$ . Here  $h$  is Planck's constant and  $\nu$  is the frequency of the photon emitted. This is a homogeneously broadened system with precisely one spectral line, that is atoms can only decay and produce a photon with an energy precisely matching the energy difference between the two states. If the atom was in the higher energy state, an incident photon with energy of  $h\nu$  could destabilise the atom and cause a photon with identical energy and momentum to be emitted by the atom. The atom would, at the time of stimulated photon emission, drop to the lower energy state as depicted in Fig. 2.1.

Let us write the rate of stimulated ( $R_{Stim}$ ) emission from the excited state ( $n_1$ ) as:

$$R_{Stim} = B\rho(\nu)n_1 \quad (2.1)$$

with  $B$  the Einstein coefficient of stimulated emission (from  $E_1$  to  $E_0$ ) and  $\rho(\nu)$  the spectral energy density (number of photons of frequency  $\nu$  per unit volume).

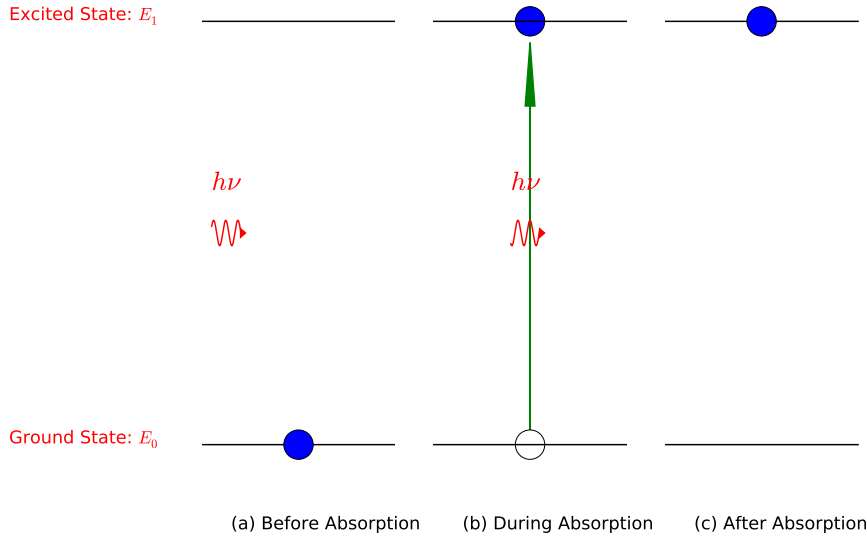


Figure 2.2: Two-level laser system:(a) Atom is unexcited and in the ground state energy level  $E_0$ . (b) A photon with energy  $h\nu = \Delta E$  is incident on the excited atom, exciting the atom with exactly an energy of  $\Delta E$ . (c): The excited atom is now in the above-ground state. The incident photon has been absorbed.

### 2.1.1.2 Stimulated Absorption

Similarly with stimulated emission, stimulated absorption can only occur when the incident photon's energy precisely matches the energy difference between the ground and the excited state, otherwise the material appears transparent to that wavelength. This is depicted in Fig. 2.2.

Let us write the rate of stimulated absorption ( $R_{Abs}$ ) from the ground state ( $n_0$ ) to be:

$$R_{Abs} = C\rho(\nu)n_0 \quad (2.2)$$

with  $C$  the Einstein coefficient of stimulated absorption.

### 2.1.1.3 Spontaneous Emission

Unlike stimulated absorption and emission, spontaneous emission does not involve an incident photon. An atom in the excited state (which may have occurred through stimulated absorption) can decay randomly to the ground state by emission of a photon of energy  $\Delta E = h\nu$  in a random direction. The spontaneous emission is quantum effect often attributed to zero-point energy in the radiation field[71, p355], as opposed to a classical interaction between the excited atom and the surrounding medium.

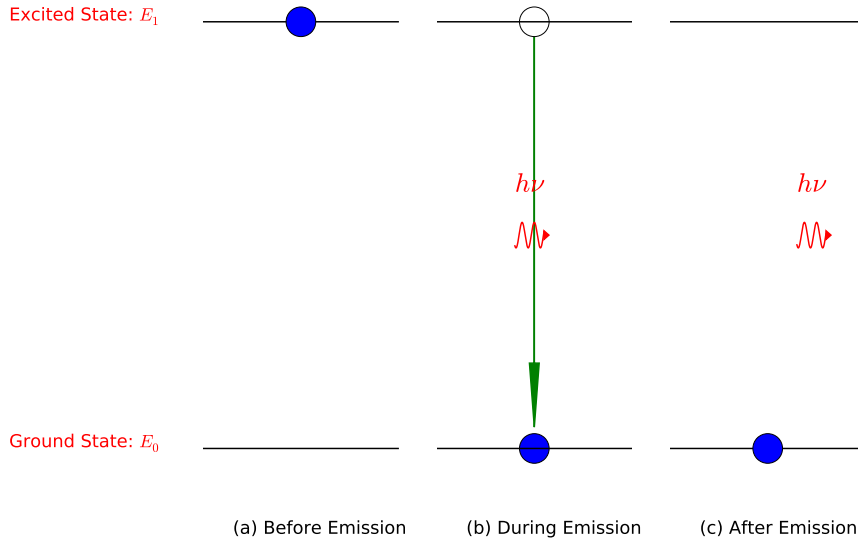


Figure 2.3: Two-level laser system:(a) Atom is in the higher energy level  $E_1$ . (b) The atom spontaneously decays releasing a photon with energy  $h\nu = \Delta E$ .(c): The atom is now in the ground state and the a photon travels off in a random spatial direction.

Let us write the probability for this transition ( $R_{Spon}$ ) with decay from the excited state ( $n_1$ ) to be:

$$R_{Spon} = An_1 \quad (2.3)$$

with  $A$  the Einstein coefficient of spontaneous emission.

#### 2.1.1.4 Relation of Einstein Coefficients.

In equilibrium, the number of transitions between states must be equal. Using (2.3), (2.1), (2.2), we can relate the transition rates:

$$R_{Stim} + R_{Spon} = R_{Abs} \quad (2.4)$$

$$n_1(B\rho(\nu) + A) = C\rho(\nu)n_0 \quad (2.5)$$

In solving for  $\rho(\nu)$  we obtain:

$$\rho(\nu) = \frac{\frac{A}{B}}{\frac{Cn_0}{Bn_1} - 1} \quad (2.6)$$

As the atoms are in thermal equilibrium, the ratio of the populations can be expressed using the Boltzmann factor  $n_m = g_m e^{-\frac{E_m}{k_B T}}$  with  $n_m, E_m, g_m$  the

population, energy and degeneracy of the  $m^{th}$  energy level.  $T$  temperature of the system Kelvin and  $k_B$  the Boltzmann constant. The population ratio is therefore:

$$\frac{n_1}{n_0} = e^{-\frac{h\nu}{k_B T}} \frac{g_1}{g_0} \quad (2.7)$$

$\rho(\nu)$  can be simplified:

$$\rho(\nu) = \frac{\frac{A}{B}}{\frac{Cg_0}{Bg_1} e^{\frac{h\nu}{k_B T}} - 1}. \quad (2.8)$$

Eq. (2.8) can be compared with Planck's Equation for Black Body radiation:

$$\rho(\nu) = \frac{8\pi\nu^2}{c^3} \frac{h\nu}{e^{\frac{h\nu}{k_B T}} - 1} \quad (2.9)$$

which must agree for all temperatures. Thus the prefactors are related by the following expressions:

$$\frac{A}{B} = \frac{8\pi h\nu^3}{c^3} \quad (2.10)$$

$$\frac{B}{C} = \frac{g_0}{g_1} \quad (2.11)$$

for the Einstein coefficients. A (trivial) consequence of these relations is that when  $n_0 = n_1$  and  $g_0 = g_1$  the likelihood of stimulated absorption and stimulated emission are equal.

## 2.2 Semi-classical Laser Theory

Next a semi-classical approach is introduced, extending the single-mode theory explored previously[48, 97] for semiconductor lasers with multiple longitudinal modes[77, Ch. 3.2]. The simplest construction of a laser consists of a multi-level atomic system placed in a laser cavity. For a semiconductor material, excited atoms are not utilised but electron-hole pairs.

These electron-hole pairs recombine to emit a photon, and are generated by pumping or incident photons. The generation of an electron-hole pair therefore corresponds to a transitions from ground to excited energy state in an atom. However, this analogy is not perfect, as the number of atoms in the ground state has no direct equivalent in the electron-hole pair description. This difference is

significant and its importance will be addressed later.

A homogeneous medium, such as the laser gain medium composed of identical two-level atoms, has a finite expected lifetime in an excited state. The length of the lifetime is inversely proportional to the width of the emission spectra in the frequency domain. Thus a semiconductor gain medium, with a relatively short carrier lifetime, can be subject to *homogeneous broadening* of the emission spectrum. However, electron-hole pairs in a laser gain medium do not necessarily have identical energy band gaps, due to the material composition and lattice structure. Therefore broadening of the emission spectra can also be influenced by *in-homogeneous broadening*. It has been shown that the interesting laser dynamics regarding saturation and broadening are a combination of the homogeneous and in-homogeneous properties of the semiconductor material[15].

To correctly describe the evolution of the electric field in the semiconductor laser cavity Maxwell's Equations are used in the following mks units:

$$\nabla \cdot \vec{B} = 0 \quad (2.12)$$

$$\nabla \times \vec{E} = -\dot{\vec{B}} \quad (2.13)$$

$$\nabla \times \vec{H} = \vec{j} + \dot{\vec{D}} \quad (2.14)$$

$$\nabla \cdot \vec{E} = \frac{\rho}{\epsilon_0} \quad (2.15)$$

with  $\vec{j} = (\sigma \vec{E})$  the current density,  $\vec{B} = \mu_0 \vec{H}$ ,  $\rho$  charge density and  $\vec{D} = \epsilon_0 \vec{E} + \vec{P}$ . Here  $\vec{B}$  is the magnetic field,  $\vec{H}$  is the magnetic field strength,  $\vec{D}$  is the electric displacement. The constants  $\mu_0$  and  $\sigma$  take the usual meanings of magnetic permeability and conductivity of the medium of the laser cavity and give rise to the loss terms in the spatial-temporal evolution of the wave.

The well-known wave-equation for the electric field can be found by taking the time derivative of Eq. (2.14):

$$\nabla \times \dot{\vec{H}} = \dot{\vec{j}} + \ddot{\vec{D}} \quad (2.16)$$

$$\nabla \times \left( \frac{1}{\mu_0} \dot{\vec{B}} \right) = \sigma \dot{\vec{E}} + \epsilon_0 \ddot{\vec{E}} + \ddot{\vec{P}} \quad (2.17)$$

$$\nabla \times (\nabla \times \vec{E}) = \sigma \mu_0 \dot{\vec{E}} + \epsilon_0 \mu_0 \ddot{\vec{E}} + \mu_0 \ddot{\vec{P}} \quad (2.18)$$

and using the well-known vector identity

$$\nabla \times (\nabla \times \vec{A}) = \nabla(\nabla \cdot \vec{A}) - \nabla^2 \vec{A} \quad (2.19)$$

and  $\nabla \cdot \vec{E} = 0$ , Eq. (2.18) becomes:

$$\nabla^2 \vec{E} - \sigma \mu_0 \dot{\vec{E}} - \epsilon_0 \mu_0 \ddot{\vec{E}} = \mu_0 \vec{P} \quad (2.20)$$

Eq. (2.20) is the same form of the wave equation as previously derived in [34, 97, 75] to include the material effects of the propagating radiation.

The spatial dependence can be separated from the time dependence[102] and the appropriate spatial boundary conditions, from the facets, can be imposed. I therefore expand  $\vec{E}$  and  $\vec{P}$  in the form:

$$\vec{E}(z, t) = \frac{1}{2} \sum_n \vec{\mathcal{A}}_n(t) U_n(z) \quad (2.21)$$

$$\vec{P}(z, t) = \frac{1}{2} \sum_n \vec{\mathcal{P}}_n(t) e^{-i[\nu_n t + \phi_n(t)]} U_n(z) \quad (2.22)$$

Denoting  $\vec{\mathcal{A}}_n$  as the complex electric field

$$\vec{\mathcal{A}}_n(t) = \vec{E}_n(t) e^{-i[\nu_n t + \phi_n(t)]} \quad (2.23)$$

where  $\vec{E}_n$  and  $\vec{\phi}_n(t)$  are slowly varying variables compared to the fast optical frequency oscillation. The evolution of the electric field  $\vec{E}_n$  and  $\vec{\mathcal{P}}_n$  (slow, real functions) can now be expressed in differential form. Having performed a separation of variables, and utilised boundary conditions that reduced the spatial dependence of the laser to a single axis, I now drop the vector notation for brevity, and consider the magnitude of the  $E_n$  and  $\mathcal{P}_n$  fields.

In an infinite medium with no facets, there exist a continuum of modes. However, the length  $L$  of the cavity is finite and well-defined, (formed using two highly reflective mirrors or facets cut into the gain medium[31]). This places boundary conditions on the electric field allowing only a discrete set of modes in the laser to achieve significant magnitude[75, Sec 21-2]. As a result only modes with a circular frequency:

$$\Omega_n = \frac{n\pi c}{L} = K_n c \frac{1}{\sqrt{\epsilon_r \mu_r}} \quad (2.24)$$

$$c = \frac{1}{\sqrt{\epsilon_0 \mu_0}} \quad (2.25)$$

are relevant. Here  $c$  is the speed of light in a vacuum,  $n$  is a large integer ,  $K_n$  is the corresponding wave number and  $\Omega_n$  is the eigenfrequency.  $\epsilon_0$  and  $\mu_0$

are the permittivity and permeability of the vacuum. The addition of  $\epsilon_r$  and  $\mu_r$  (relative permittivity and permeability) correct for the presence of the medium. Using a separation of variables, the spatial component of the wave equation is assumed to have the form (of a plane wave)

$$U(z) = \sin(K_n z) \quad (2.26)$$

as it satisfies the boundary conditions imposed by the cavity. Fox and Li[24] have shown that there is little variation in the  $X - Y$  plane in an optical wavelength and are therefore we can approximate the cavity as a strip existing in  $Z$  (The orientation of  $Z$  is transverse to the direction of optical propagation).

By taking the first and second time derivatives of Eq.(2.21) we arrive at

$$\dot{E} = \sum_n e^{-i(\nu_n t + \phi_n)} \{ \dot{E}_n(t) + E_n(t)[-i(\nu_n + \dot{\phi}_n)] \} U_n(z) \quad (2.27)$$

$$\begin{aligned} \ddot{E} = & \sum_n e^{-i(\nu_n t + \phi_n)} \{ \ddot{E}_n(t) + 2\dot{E}_n(t)(-i[\nu_n + \dot{\phi}_n]) + E_n(t)[(-i(\nu_n + \dot{\phi}_n))^2 - i\ddot{\phi}] \} \\ & \cdot U_n(z) \end{aligned} \quad (2.28)$$

with identical expressions for  $\dot{\mathcal{P}}_n$  and  $\ddot{\mathcal{P}}_n$  respectively. Substituting Eqs. (2.27), (2.28) and (2.26) into (2.20) we obtain:

$$\begin{aligned} & K_n^2 E_n + \mu_0 \sigma [\dot{E}_n - i(\nu_n + \dot{\phi}) E_n] \\ & + \mu_0 \epsilon \{ \ddot{E}_n - i\ddot{\phi} E_n + \dot{E}_n[-2i(\nu_n + \dot{\phi})] - E_n \{ (\nu_n + \dot{\phi})^2 \} \} \\ & = \mu_0 (\nu_n + \dot{\phi})^2 (\mathcal{P}_n) + \text{terms in } \dot{\mathcal{P}}_n \text{ and } \ddot{\mathcal{P}}_n \end{aligned} \quad (2.29)$$

after factoring out the multiplicative exponential and  $U(z)$  terms.

For our slowly varying complex fields, that vary by a negligible amount in an optical frequency period, I neglect second order time derivatives and mixed-first order time derivatives[75, p100],  $\dot{\mathcal{P}}_n, \ddot{\phi}_n, \ddot{E}_n, \dot{E}_n \dot{\phi}_n, \dot{\phi}_n^2$ . Under the property of Class B semiconductor lasers, the dipole-moments in the gain medium contribute to a slowly varying polarisation, and high reflectivity is achieved at the boundaries (required for signal amplification)  $\dot{\phi}_n \mathcal{P}_n$  and  $\dot{\mathcal{P}}_n$  are also neglected.

Finally we arrive at:

$$\begin{aligned} & k^2 E_n + \mu \sigma \{ 0 - i E_n (\nu_n + \dot{\phi}) \} \\ & + \mu \epsilon [0 - 0 - 2i \dot{E}_n (\nu_n + 0)] - E_n \{ (\nu_n + \dot{\phi})^2 \} \\ & = \mu (\nu_n + 0)^2 \mathcal{P}_n \end{aligned} \quad (2.30)$$

which relates the  $E_n$  and  $\mathcal{P}_n$  fields.

By separating the real and imaginary parts of  $\mathcal{P}_n$ , we obtain for the imaginary part:

$$\begin{aligned} -\mu\sigma\{E_n(\nu_n + \dot{\phi})\} - 2\mu\epsilon\dot{E}_n\nu_n &= \mu(\nu_n)^2 Im\{\mathcal{P}_n\} \\ \dot{E}_n\{-2\mu\epsilon\nu_n\} &= \mu\sigma\{E_n(\nu_n + \dot{\phi})\} + \mu(\nu_n)^2 Im\{\mathcal{P}_n\} \\ \dot{E}_n &= -\frac{1}{2}\Gamma_E E_n - \frac{1}{2}\frac{\nu}{\epsilon}Im\{\mathcal{P}_n\} \end{aligned} \quad (2.31)$$

and for the real part

$$\begin{aligned} k^2 E_n - \mu\epsilon E_n\{(\nu_n + \dot{\phi})^2\} &= \mu(\nu_n)^2 Re\{\mathcal{P}_n\} \\ E_n(k^2 - \mu\epsilon\{(\nu_n + \dot{\phi})^2\}) &= \mu(\nu_n)^2 Re\{\mathcal{P}_n\} \\ (\Omega_n^2 - \{(\nu_n + \dot{\phi})^2\}) &= \frac{(\nu_n)^2}{\epsilon E_n} Re\{\mathcal{P}_n\} \end{aligned} \quad (2.32)$$

using  $\Gamma_E = \frac{\sigma}{\epsilon}$  and  $\sigma = \epsilon\frac{\nu}{\Omega_n}$ , where  $\nu$  is understood to be a good approximation of the passive modal frequencies when the difference between the  $\nu_n$ 's is small.

Traditionally [75, p100],  $(\nu_n)^2$  is approximated by  $\nu_n\nu$ , where  $\nu$  closely represents the passive modal frequency when there is little variation between the  $\nu_n$ 's across  $n$ . In this approximation (and that in the absence of a field  $\mathcal{P}_n$ ,  $\Omega_n = \nu_n + \dot{\phi}_n$ ),  $(\Omega_n^2 - \{(\nu_n + \dot{\phi})^2\})$  becomes  $2\nu_n(\Omega_n - \{(\nu_n + \dot{\phi})\})$ .

Eq (2.32) becomes Eq. (2.33)

$$\begin{aligned} 2\nu_n(\Omega_n - \{\nu_n + \dot{\phi}\}) &= \frac{\nu_n\nu}{\epsilon E_n} Re\{\mathcal{P}_n\} \\ (\Omega_n - \{\nu_n + \dot{\phi}\}) &= \frac{\nu}{2\epsilon E_n} Re\{\mathcal{P}_n\} \\ \{\nu_n + \dot{\phi}\} &= \Omega - \frac{\nu}{2\epsilon E_n} Re\{\mathcal{P}_n\} \end{aligned} \quad (2.33)$$

Eq. 2.31 and 2.33 are known as the self-consistency equations, having combined classical- and statistical mechanics to obtain them[75, 97]. They also require that the microscopic polarisation, due to the electron-hole pairs, be equal to the macroscopic polarisation. This will be addressed shortly.

Eq. 2.31 is also recognisable as one of the Maxwell-Bloch Equations, which depends on the polarisation of the medium  $\mathcal{P}_n$ . Let us consider the physical meaning of Eq. ( 2.31) and ( 2.33). In the absence of  $\mathcal{P}_n$ (no active medium), we have an exponentially decaying  $E_n$  field with the appropriately named constant  $\frac{1}{2}\Gamma_E$ , the inverse lifetime of the electric field. However, for a homogeneous and isotropic dielectric medium, such as the semiconductor laser gain medium, a

polarisation exists (due to the electron-hole pairs) and is aligned with  $E_n$ [22, Chapter 10].

$$\mathcal{P}_n = \epsilon(\chi' + i\chi'')E_n \quad (2.34)$$

Therefore 2.31 and 2.33 can be written as:

$$\dot{E}_n = -\frac{1}{2}\Gamma_E E_n + \frac{1}{2}\nu\chi'' E_n \quad (2.35)$$

$$\{v_n + \dot{\phi}\} = \Omega - \frac{\nu}{2}\chi' \quad (2.36)$$

The first and second terms of Eq 2.35 are frequently identified as the field decay and gain terms. Hence  $\chi''$  is referred to as the material gain due to the electric field and population inversion.  $\chi'$  is referred to as the population-induced refractive index change. The following definitions are used to represent the modal gain and the population induced refractive index ( $\delta n$ ).

$$\nu\chi'' = \frac{c}{n_b}g(N, \nu, E_1, E_2) \quad (2.37)$$

$$\chi' = \frac{1}{n_b}\delta n \quad (2.38)$$

Eq (2.37) is defined here for a semiconductor laser with two primary modes, but  $g(N, \nu, E_1, E_2)$  can be arbitrarily extended for additional modes. Here the spectral component  $\nu$  is unimportant[16] and is absorbed in the prefactor of the  $g(N, \nu, E_1, E_2)$  and  $\delta n$  functions. The exact form of  $g(N, \nu, E_1, E_2)$  will be derived later. The complex (passive) refractive index of the gain medium, in the absence of a pumping or population inversion, is defined as  $n_b = \frac{\sqrt{\epsilon_0\mu_0\epsilon_r\mu_r}}{c}$ .  $\delta n$  and  $g(N, \nu, E_1, E_2)$  can be related through the Kramers-Kronig relation[45] and the well-known  $\alpha$  factor (line-width enhancement factor) can be defined through their relation

$$\begin{aligned} \alpha &= -\frac{\frac{\partial\chi'}{\partial N}}{\frac{\partial\chi''}{\partial N}} \\ &= -\frac{\frac{\partial(\delta n)}{\partial N}}{\frac{\frac{c}{\nu}\frac{\partial g(N, \nu, E_1, E_2)}{\partial N}}{\partial N}}. \end{aligned} \quad (2.39)$$

Although the gain function and refractive index change do not vary linearly, a good linearisation of the gain can be made around lasing threshold[1, p36 and

191], hence I can write  $g$  and  $\delta n$  in as dependant on  $N$  and  $N_{Thr}$  while neglecting the spectral dependence.::

$$g(N - N_{Thr}, E_1, E_2) = \frac{n_b}{2c} [\Gamma_E + \zeta(N - N_{Thr}, E_1, E_2)] \quad (2.40)$$

$$\delta n = -\frac{n_b}{\nu} [B_0 + \frac{\alpha}{2} \zeta(N - N_{Thr}, E_1, E_2)] \quad (2.41)$$

where  $N_{Thr}$  is  $N$  at the onset of a population inversion.  $B_0$  is a constant of integration which will be determined later and  $\zeta$  is the non-linear differential gain function. The exact form of  $\zeta$  will be investigated later. The additional  $\Gamma_E$  term in Eq.(2.40) comes from knowing that at  $N = N_{Thr}$ , the net gain of  $E_n$  should be zero, as well as  $\dot{E}$ . That is, the gain should equal the cavity losses at threshold. Eq.(2.40) and Eq.(2.41) are still related through the  $\alpha$  parameter as defined in Eq.(2.39).

Next a formulation for  $N$  and  $\mathcal{P}_n$  is required in order to fully understand  $\alpha$ , as well as the full temporal evolution of our system. I will now motivate their corresponding Maxwell-Bloch forms.

### 2.2.1 Maxwell-Bloch

In this section I will motivate an expression for the macroscopic polarisation of the medium which are obtained by a statistical summation of the microscopic polarisation. The atom laser was introduced as simple description of a functioning laser, however I now have reached the point where the differences between a semiconductor gain medium and atomic laser gain medium must be addressed. The atom laser requires a minimum of three distinct energy levels to achieve a population inversion. However, in a semiconductor laser, electron-hole pairs are the excited state of the gain medium. The differences between semiconductor and atomic gain media in the quantum picture are irreconcilable, given that it is not trivial to model the ground state of the semiconductor laser by counting the number of annihilated election-hole pair. I will quickly derive the Maxwell-Bloch equations for two-level atom laser and discuss the restrictions.

In the atom laser, a wave function describing the atom's probability of existing in either of two states is trivial. Using the well-known Schrödinger Equation[55], for two-level atom, the wave-function  $|\Psi(t)\rangle$  is modelled by:

$$i\hbar \frac{\partial |\Psi(t)\rangle}{\partial t} = H |\Psi(t)\rangle \quad (2.42)$$

$$H = H_0 + V \quad (2.43)$$

with  $H$  is the Hamiltonian operator, describing the total energy of the system as a linear combination of the atoms energy at the state plus the contribution of the present  $E_n$  field:  $V = e\vec{r} \cdot \vec{e}_E E$ . Here  $E_n$  is the scalar magnitude of the electric field,  $\vec{r} \cdot \vec{e}_E$  are the unit vectors acting in the  $r$  and  $E$  directions respectively.  $e$  is the electron charge.

The wave-function  $|\Psi(t)\rangle$  for the atom (with normalised population  $|A^2| + |B^2| = 1$ ) is a linear combination of the wave-functions of the individual states (absorbing the time dependence for brevity):

$$|\Psi\rangle = A |\psi_0\rangle + B |\psi_1\rangle \quad H_0 \psi_j = \hbar \omega_j \psi_j, \quad j = 0, 1 \quad (2.44)$$

The evolution of the population in each state evolves according to[55, p.2]:

$$\begin{aligned} i \frac{\partial A}{\partial t} &= \omega_0 A + \frac{\mu E_n}{\hbar} B + \frac{\nu_0 E_n}{\hbar} \overset{0}{A} \\ i \frac{\partial B}{\partial t} &= \omega_1 B + \frac{\mu E_n}{\hbar} A + \frac{\nu_1 E_n}{\hbar} \overset{0}{B} \end{aligned} \quad (2.45)$$

with  $A, B$  the population in the ground states and excited respectively.

In Eq. (2.45)  $\mu$  is introduced as an approximation of the dipole[55, p.2] and  $\nu_0$  and  $\nu_1$  vanish when the gain medium is invariant under a relaxation under a reflection symmetry. Other atom specific approximations, including neglecting the centre of mass are also used.

Using angle-brackets, I denote the ensemble average taken over all atoms, for two useful quantities  $A^*B$  (microscopic polarisation due to a single excited atom) and  $|A|^2$  (probability that the atom is in state  $A$ ).  $*$  is the complex conjugation operator.

$$\begin{aligned} \frac{\partial \langle A^* B \rangle}{\partial t} &= -i(\omega_1 - \omega_0) \langle A^* B \rangle + i \frac{\mu}{\hbar} [\langle E_n | B^2 | \rangle - \langle E_n | A^2 | \rangle] \\ \frac{\partial \langle |A^2| \rangle}{\partial t} &= -\frac{\partial \langle |B^2| \rangle}{\partial t} = i \frac{\mu}{\hbar} [\langle E_n A B^* \rangle - \langle E_n A^* B \rangle] \end{aligned} \quad (2.46)$$

Defining  $D$  as the difference  $\langle |A^2| \rangle - \langle |B^2| \rangle$ , (normalised population difference) and  $P = \langle A^* B \rangle$ (complex polarisation) we obtain the Maxwell-Bloch equations

for  $D$  and  $P_n$

$$\frac{\partial D}{\partial t} = -2i\frac{\mu E_n}{\hbar}[P_n - P_n^*] \quad (2.47)$$

$$\frac{\partial P_n}{\partial t} = -i(\omega_1 - \omega_0)P_n - i\frac{\mu E_n}{\hbar}D \quad (2.48)$$

It should be noted that  $P_n$  and  $E_n$  here are slow variables, thanks to the same expansion utilised in (2.22). As  $P_n$  is complex,  $P_n - P_n^*$  becomes:

$$P_n - P_n^* = i2Im\{P_n\} \quad (2.49)$$

Next I re-normalise the population inversion to  $N$ , such that the value of  $N = 0$  will correspond to a zero population inversion.

$$N = \frac{-D + 1}{2}$$

$$N = \frac{\langle |B^2| \rangle - \langle |A^2| \rangle + 1}{2} \quad (2.50)$$

Now, substituting Eq. (2.49) and (2.50) into Eqns. (2.47) and (2.48) yield the re-normalised, simplified Maxwell-Bloch equations for a two-level atom:

$$\frac{\partial N}{\partial t} = -4\frac{\mu E_n}{\hbar}[Im\{P_n\}] \quad (2.51)$$

$$\frac{\partial P_n}{\partial t} = -i(\omega_1 - \omega_0)P_n + i\frac{\mu E_n}{\hbar}(2N - 1) \quad (2.52)$$

Regrettably, many of the atomic specific properties used in deriving the classical Maxwell-Bloch equations make it difficult to justify their use for semiconductor lasers. Issues can be seen immediately when a Hamiltonian is sought to model the microscopic semiconductor behaviour. Simply put, in the excited state, a semiconductor material has an electron-hole pair, whereas in the ground state, the electron-hole pair has annihilated to produce a photon. Thus the first challenge begins with accounting for the changing number of particles between states. In 1995, the search, spanning over a decade[51], for Semiconductor Maxwell-Bloch Equations(SBE's)[9, 58] with a similar representation to that of Eqns (2.51), (2.52) came to a satisfactory end.

Beginning with the Hamiltonian for a two-level semiconductor, which includes

direct Coulomb interactions is:

$$H = \sum_k \epsilon_c(k) a_{c,k}^\dagger a_{c,k} + \sum_k \epsilon_v(k) a_{v,k}^\dagger a_{v,k} + V + H_F, \quad (2.53)$$

$$\begin{aligned} V = & \frac{1}{2} \sum_{k,k';q \neq 0} v(q) [a_{c,k+q}^\dagger a_{c,k'-q}^\dagger a_{c,k'}^\dagger a_{c,k} \\ & + a_{v,k+q}^\dagger a_{v,k'-q}^\dagger a_{v,k'}^\dagger a_{v,k} \\ & + 2a_{c,k+q}^\dagger a_{v,k'-q}^\dagger a_{v,k'}^\dagger a_{c,k'}^\dagger], \end{aligned} \quad (2.54)$$

$$H_F = - \sum_k [\mu_k E_L(t) a_{c,k}^\dagger a_{v,k}^\dagger + \mu^* E_L^* a_{v,k}^\dagger a_{c,k}^\dagger] \quad (2.55)$$

where  $\epsilon_c(k)$  and  $\epsilon_v(k)$  are the momentum specific energies in the conduction and valence bands respectively,  $E_L$  is the microscopic field that couples with the dipole and  $v(q)$  are the Coulomb-exchange interaction coefficients.

$$\begin{aligned} v(q) &= \hbar\omega_x \frac{8\pi a_0}{\kappa_b q^2}, & \epsilon_c(k) &= E_g + \frac{\hbar^2 k^2}{2m_e}, \\ \epsilon_v(k) &= -\frac{\hbar^2 k^2}{2m_e}. \end{aligned} \quad (2.56)$$

$E_g$  is the unperturbed band gap energy,  $a_0$  is the Bohr radius, the Coulomb-exchange interaction coefficients are given in terms of the excitation energies  $\hbar\omega_x$ . The methodology followed in [9] is too detailed to repeat here completely. However, similar to the approach for the atomic laser,  $E$  and  $P$  are expanded as the slowly varying variables  $E_n$  and  $P_n$  respectively. The key points of the derivation include the calculation of the occupation and transition probabilities  $n_k = \langle a_{c,k}^\dagger a_{c,k} \rangle$ ,  $p_k = \langle a_{c,k}^\dagger a_{v,k} \rangle$  and the use of the relation  $\langle a_{c,k}^\dagger a_{c,k} \rangle + \langle a_{v,k}^\dagger a_{v,k} \rangle = 1$  to reduce the order of the equations by eliminating the need to calculate the equation of motion for valence-band electrons. The macroscopic (Maxwell)  $E_n$  and  $P_n$  fields are due to an average over a density of states of the microscopic electric and polarisation fields. By calculating the density of states average to the  $\frac{\partial p_k}{\partial t}$ , as  $p_k$  is a slowly varying variable, the macroscopic equation for  $\frac{\partial P_n}{\partial t}$  is shown to be identical to Eq. 2.52, up to a correction of the prefactors. Therefore, I can continue to use Eq. 2.52 in my discussion of the Semiconductor Maxwell-Bloch equations.

Additionally, I add decay terms to Eqns (2.51, 2.52) phenomenologically, to represent the fields' decay  $\Gamma_N N$ ,  $\Gamma_P P$ , and the pump driving the normalised

population difference,  $\Lambda$ .

$$\frac{\partial N}{\partial t} = -4 \frac{\mu E_n}{\hbar} [Im\{P_n\}] - \Gamma_N N + \Lambda \quad (2.57)$$

$$\frac{\partial P_n}{\partial t} = -i(\omega_1 - \omega_0)P_n + i \frac{\mu E_n}{\hbar} (2N - 1) - \Gamma_P P_n \quad (2.58)$$

Different classes of lasers can be distinguished by the relative magnitude of  $\Gamma_P$ ,  $\Gamma_N$  and  $\Gamma_E$ [6]. In the approximation, where  $\Gamma_P \gg \Gamma_N, \Gamma_E$ , the polarisation appears constant. As a result, the four-dimensional phase-space  $(E, Re\{P\}, Im\{P\}, N)$  reduces to two dimensions, and the system evolves on the slow manifold, where  $P_n$  has the form shown in Eq. (2.60) below.

The time-scale magnitude of  $P_n$  is one of the first device-specific approximations introduced in this derivation. The devices studied in this thesis are Class B devices [88, p. 48], where the polarisation amplitude is well approximated as constant and the phase is still a fast varying quantity. The polarisation and electric fields can be expanded using (2.22) and (2.49). I consider the fixed point solution of the polarisation amplitude:

$$\frac{\partial P_n}{\partial t} = 0 \quad (2.59)$$

$$\begin{aligned} [+i(\omega_1 - \omega_0) + \Gamma_{\mathcal{P}}] \mathcal{P} &= i \frac{\mu E_n}{\hbar} (2N - 1) \\ P_n &= \frac{i \mu E_n (2N - 1)}{\hbar [+i(\omega_1 - \omega_0) + \Gamma_{\mathcal{P}}]} \\ P_n &= \frac{i \mu E_n (2N - 1)}{\hbar [+i(\omega_1 - \omega_0) + \Gamma_{\mathcal{P}}]} \frac{[-i(\omega_1 - \omega_0) + \Gamma_{\mathcal{P}}]}{[-i(\omega_1 - \omega_0) + \Gamma_{\mathcal{P}}]} \\ P_n &= \frac{\mu E_n (2N - 1)}{1} \frac{[+(\omega_1 - \omega_0) + i \Gamma_{\mathcal{P}}]}{[(\omega_1 - \omega_0)^2 + \Gamma_{\mathcal{P}}^2]} \end{aligned} \quad (2.60)$$

Therefore, the imaginary and real parts of  $P$  are now:

$$Im\{P_n\} = \frac{\mu(2N - 1)\Gamma_{\mathcal{P}}}{\hbar[(\omega_1 - \omega_0)^2 + \Gamma_{\mathcal{P}}^2]} E_n \quad (2.61)$$

$$Re\{P_n\} = \frac{\mu(2N - 1)(\omega_1 - \omega_0)}{\hbar[(\omega_1 - \omega_0)^2 + \Gamma_{\mathcal{P}}^2]} E_n \quad (2.62)$$

The Lorentzian profile, defined as:

$$\mathcal{L}(\omega_0 - \omega_1) = \frac{\Gamma_P^2}{(\omega_0 - \omega_1)^2 + \Gamma_P^2} \quad (2.63)$$

simplifies the gain and population-induced refractive index change expressions. The gain and population-induced refractive index change are:

$$g(N, E_1, E_2) = \frac{\mu}{\hbar\Gamma_{\mathcal{P}}}(2N - 1)\mathcal{L}(\omega_0 - \omega_1) \quad (2.64)$$

$$\delta n = \frac{\mu}{\hbar\Gamma_{\mathcal{P}}^2}\mu(2N - 1)(\omega_1 - \omega_0)\mathcal{L}(\omega_0 - \omega_1) \quad (2.65)$$

In this form, it is shown that with the presence of the Lorentzian profile, that the  $g$  and therefore  $\partial n$  have a nonlinear dependence on the square of the difference of the photons energy  $(\omega_0 - \omega_1)^2$  (up to an additional  $\hbar$  in the denominator). It is desirable to derive a relation based upon the amplitudes of the lasing electric fields (the  $\zeta$  function introduced earlier). This will be addressed in the next section. Again, in this form, both  $g$  and therefore  $\partial n$  can be seen to be related through the  $\alpha$  factor, however these functions have been derived for the case of a single electron-hole pair.

$$\dot{N} = \Lambda - \Gamma_N N - \frac{2c\mu}{\epsilon n_b}[g(N, E_1, E_2)|E_1^2| + g(N, E_2, E_1)|E_2^2|] \quad (2.66)$$

$$\dot{N} = \Lambda - \Gamma_N N - \frac{2c\mu n_b}{\epsilon n_b 2c}[\hat{g}(N, E_1, E_2)|E_1^2| + \hat{g}(N, E_2, E_1)|E_2^2|]$$

$$\dot{N} = \Lambda - \Gamma_N N - \frac{\mu}{\epsilon}[\hat{g}(N, E_1, E_2)|E_1^2| + \hat{g}(N, E_2, E_1)|E_2^2|] \quad (2.67)$$

where  $\hat{g}(N, E_1, E_2) = \frac{2c}{n_b}g(N, E_1, E_2)$ .

Next, a rescaling of both  $N$  and  $E$  is needed to transform the rate equation model into a more desirable form. Therefore for population inversion  $n$  is introduced in terms of  $N$  and  $N_{Thr}$  (the lasing threshold value of  $N$ ):

$$n = \frac{N - N_{Thr}}{2N_{Thr}} \quad (2.68)$$

This can be rewritten as:

$$(2n + 1)N_{Thr} = N$$

$$2\dot{n}N_{Thr} = \dot{N} \quad (2.69)$$

Substituting Eqs. (2.68) and (2.69) into Eq. (2.67) yields:

$$\begin{aligned} 2N_{Thr}\dot{n} = & \Lambda - \Gamma_N(2n + 1)N_{Thr} \\ & - \frac{\mu}{\epsilon}[\hat{g}((2n + 1)N_{Thr}, E_1, E_2)|E_1^2| \\ & + \hat{g}((2n + 1)N_{Thr}, E_2, E_1)|E_2^2|] \end{aligned} \quad (2.70)$$

$$\begin{aligned} 2N_{Thr}\dot{n} = & \Lambda - \Gamma_N N_{Thr} - \Gamma_N(2n) \\ & - \frac{\mu}{\epsilon}[\hat{g}((2n + 1)N_{Thr}, E_1, E_2)|E_1^2| \\ & + \hat{g}((2n + 1)N_{Thr}, E_2, E_1)|E_2^2|] \end{aligned} \quad (2.71)$$

At this point in the rescaling, a derivation of  $\hat{g}$  in terms of  $N, E_1$  and  $E_2$  is required before any further simplifications can be made.

To accurately describe the behaviour of the many electron-hole pairs with this approach would require considering a Fermi-Dirac distribution of the entire volume. Fortunately, it has been shown[16] that the gain peak and population induced refractive index functions are linear in  $N$  around threshold. Therefore, only an understanding of the gain function's dependence on  $E_1$  and  $E_2$  remain.

### 2.2.2 Non-linear Gain Derivation.

Next a more complete understanding of the material gain function is required. As presented in Sec.2.2.1 the gain is expected to have a dependence on  $N$  and  $E_1, E_2$ . As stimulated emission depletes electron-hole pairs, with a specific energy, it is anticipated that nearby electron-hole pairs (that have similar  $h\nu$ ) will attempt to fill in energetically attractive vacancies left behind.

In Fig.2.4 I assume a simple model for gain picture: There exists a single global carrier population  $N$ , which consists of all possible electron-hole pairs in the gain medium.  $N$  is the sum of all electron-hole pair populations  $N_k$  with energy gap:  $h\nu_k$ . In this model, for our two-mode devices, there exist two carrier populations  $N_1$  and  $N_2$ , that contribute to  $N$ , but represent the electron-hole pairs that are predominately responsible for the lasing of their respective modes  $E_1$  and  $E_2$ .  $N_n$  represent the populations of electron-hole pairs that do not (directly) achieve stimulated emission.

To completely understand the modal gain would require an exceedingly long and thorough study of *Free Carrier Theory*[16, Chapter 2]. Therefore I present a Master Equation Approach of the gain derivation where we consider the transition of excited electron-hole pairs between three allowable states:  $N_1, N_2$  and  $N_n$  which are the population sizes of electron-hole pairs in states 1, 2 and  $n$ , which

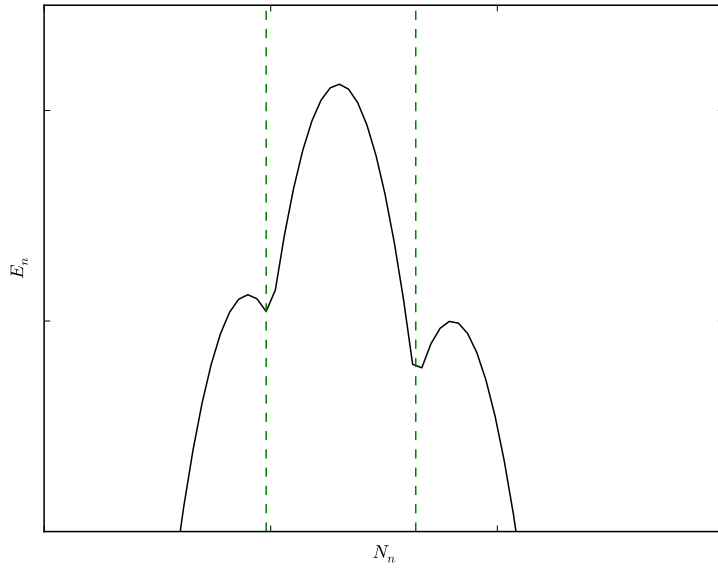


Figure 2.4: Cartoon of material gain due to population inversion of two-mode laser.

correspond to the two lasing modes (1, 2), and a general population ( $n$ ) that does not achieve lasing. Fig. 2.5 shows the allowed transitions of the electron-hole pairs, namely an electron-hole pair can move from state  $X$  to  $Y$  with a transition (coupling) rate  $T_{YX}$  if it the transition is favourable. An electron-hole pair in  $N_1$  or  $N_2$  can also reach the ground state by stimulated emission.

The basis of this model will be a paradigmatic rate equation for the discrete  $N$  populations similar to Eq.(2.71).

$$\dot{N}_1 = -(\Gamma_1 + |E_1^2|)N_1 - (T_{21} + T_{n1})N_1 + T_{12}N_2 + T_{1n}N_n \quad (2.72)$$

$$\dot{N}_2 = -(\Gamma_2 + |E_2^2|)N_2 - (T_{12} + T_{n2})N_2 + T_{21}N_1 + T_{2n}N_n \quad (2.73)$$

$$\dot{N}_n = P - \Gamma_n N_n + T_{n1}N_1 + T_{n2}N_2 - (T_{1n} + T_{2n})N_n \quad (2.74)$$

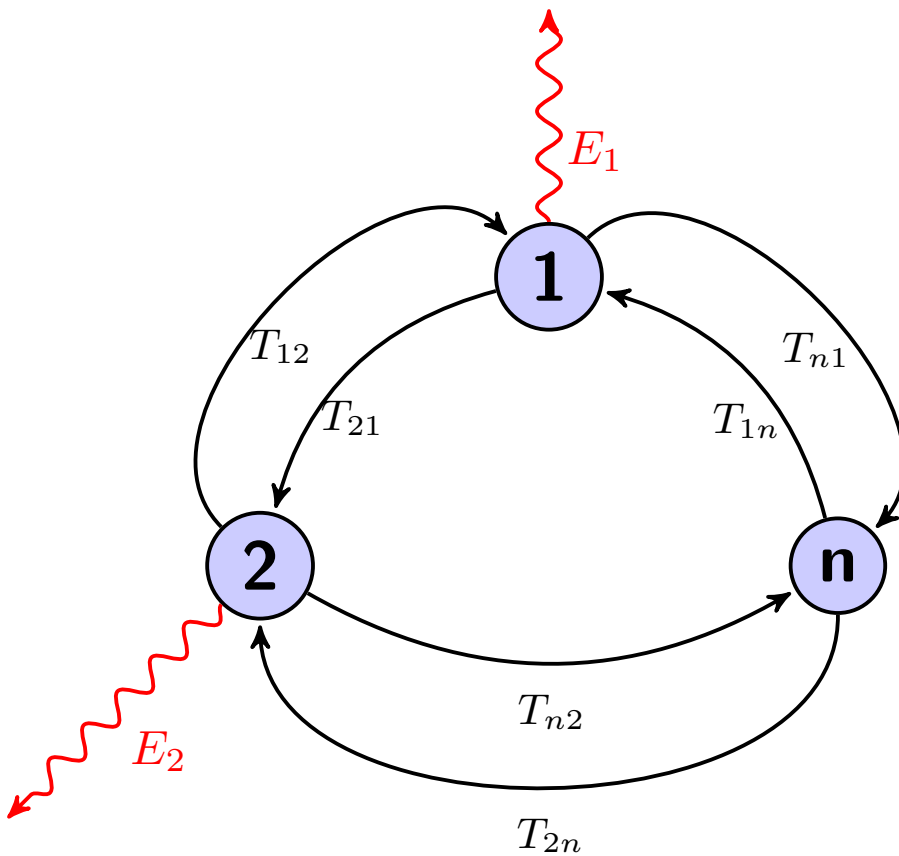


Figure 2.5: Three discrete states are available with six possible transitions between them:  $N_1$ ,  $N_2$  and  $N_n$ . Electron-hole pairs can move from state X to Y with a transition probability  $T_{YX}$ . Electron-hole pairs in  $N_1$  and  $N_2$  also have a certain lasing rate.

Which can be written in matrix form as:

$$\frac{d}{dt} \begin{pmatrix} N_1 \\ N_2 \\ N_n \end{pmatrix} = \begin{pmatrix} 0 \\ 0 \\ P \end{pmatrix} - \begin{pmatrix} \Gamma_1 + |E_1|^2 & 0 & 0 \\ 0 & \Gamma_2 + |E_2|^2 & 0 \\ 0 & 0 & \Gamma_n \end{pmatrix} \begin{pmatrix} N_1 \\ N_2 \\ N_n \end{pmatrix} + \begin{pmatrix} -(T_{21} + T_{n1}) & T_{12} & T_{1n} \\ T_{21} & -(T_{12} + T_{n2}) & T_{2n} \\ T_{n1} & T_{n2} & -(T_{1n} + T_{2n}) \end{pmatrix} \begin{pmatrix} N_1 \\ N_2 \\ N_n \end{pmatrix} \quad (2.75)$$

Now, a model using a single population  $N$  is preferred as it reduces complexity and uses the idea of a single common electron-hole population. Therefore  $N_1$  and

$N_2$  are removed adiabatically by locating their fixed points in terms of  $N_n$ :

$$\begin{aligned} \begin{pmatrix} 0 \\ 0 \end{pmatrix} &= \begin{pmatrix} 0 \\ 0 \end{pmatrix} - \begin{pmatrix} \Gamma_1 + |E_1|^2 & 0 & 0 \\ 0 & \Gamma_2 + |E_2|^2 & 0 \end{pmatrix} \begin{pmatrix} N_1 \\ N_2 \\ N_n \end{pmatrix} \\ &\quad + \begin{pmatrix} -(T_{21} + T_{n1}) & T_{12} & T_{1n} \\ T_{21} & -(T_{12} + T_{n2}) & T_{2n} \end{pmatrix} \begin{pmatrix} N_1 \\ N_2 \\ N_n \end{pmatrix} \\ \begin{pmatrix} 0 \\ 0 \end{pmatrix} &= - \begin{pmatrix} \Gamma_1 + |E_1|^2 & 0 \\ 0 & \Gamma_2 + |E_2|^2 \end{pmatrix} \begin{pmatrix} N_1 \\ N_2 \end{pmatrix} \\ &\quad + \begin{pmatrix} -(T_{21} + T_{n1}) & T_{12} \\ T_{21} & -(T_{12} + T_{n2}) \end{pmatrix} \begin{pmatrix} N_1 \\ N_2 \end{pmatrix} + \begin{pmatrix} T_{1n} \\ T_{2n} \end{pmatrix} N_n \end{aligned}$$

In the above equation, only terms contributing to  $\dot{N}_1$  and  $\dot{N}_2$  have been kept.

$$\begin{aligned} \begin{pmatrix} 0 \\ 0 \end{pmatrix} &= - \begin{pmatrix} \Gamma_1 + |E_1|^2 + T_{21} + T_{n1} & -T_{12} \\ -T_{21} & \Gamma_2 + |E_2|^2 + T_{12} + T_{n2} \end{pmatrix} \begin{pmatrix} N_1 \\ N_2 \end{pmatrix} + \begin{pmatrix} T_{1n} \\ T_{2n} \end{pmatrix} N_n \\ \begin{pmatrix} \Gamma_1 + |E_1|^2 + T_{21} + T_{n1} & -T_{12} \\ -T_{21} & \Gamma_2 + |E_2|^2 + T_{12} + T_{n2} \end{pmatrix} \begin{pmatrix} N_1 \\ N_2 \end{pmatrix} &= \begin{pmatrix} T_{1n} \\ T_{2n} \end{pmatrix} N_n \end{aligned} \quad (2.76)$$

Using the usual formula for the inversion of a square matrix with non-zero determinant:

$$\begin{pmatrix} a & b \\ c & d \end{pmatrix} = \frac{1}{ad - cb} \begin{pmatrix} d & -b \\ -c & a \end{pmatrix}$$

and introducing the short-hands

$$\begin{aligned} Q_1 &= \Gamma_1 + |E_1|^2 + T_{21} + T_{n1} \\ Q_2 &= \Gamma_2 + |E_2|^2 + T_{12} + T_{n2} \end{aligned}$$

we have

$$\begin{pmatrix} Q_1 & -T_{12} \\ -T_{21} & Q_2 \end{pmatrix}^{-1} = \frac{1}{Q_1 Q_2 - T_{21} T_{12}} \begin{pmatrix} Q_2 & T_{12} \\ T_{21} & Q_1 \end{pmatrix}$$

and thus

$$\begin{pmatrix} N_1 \\ N_2 \end{pmatrix} = \frac{1}{Q_1 Q_2 - T_{21} T_{12}} \begin{pmatrix} Q_2 & T_{12} \\ T_{21} & Q_1 \end{pmatrix} \begin{pmatrix} T_{1n} \\ T_{2n} \end{pmatrix} N_n \quad (2.77)$$

We now assume that the intraband relaxations are much quicker than the interband and stimulated emission, i.e.

$$T_{21}, T_{12}, T_{n1}, T_{n2} \gg \Gamma_1, \Gamma_2, \Gamma_n, |E_1|^2, |E_2|^2.$$

We can obtain this by formally introducing a factor  $\epsilon$  as follows

$$T_{xy} = \frac{t_{xy}}{\epsilon}$$

and then expand our results in first order of  $\epsilon$ . We get for

$$\begin{aligned} \epsilon Q_1 &= \epsilon (\Gamma_1 + |E_1|^2) + t_{21} + t_{n1} \\ \epsilon Q_2 &= \epsilon (\Gamma_2 + |E_2|^2) + t_{12} + t_{n2} \end{aligned}$$

Then we obtain for the denominator in (2.77)

$$\begin{aligned} \epsilon^2 [Q_1 Q_2 - T_{21} T_{12}] &= \epsilon Q_1 \epsilon Q_2 - t_{21} t_{12} \\ &= (\epsilon (\Gamma_1 + |E_1|^2) + t_{21} + t_{n1}) (\epsilon (\Gamma_2 + |E_2|^2) + t_{12} + t_{n2}) - t_{21} t_{12} \\ &\approx (t_{21} + t_{n1})(t_{12} + t_{n2}) - t_{21} t_{12} \\ &\quad + \epsilon \left\{ (t_{21} + t_{n1})(\Gamma_2 + |E_2|^2) + (t_{12} + t_{n2})(\Gamma_1 + |E_1|^2) \right\} \\ &= (t_{n1} t_{n2} + t_{21} t_{n2} + t_{n1} t_{12}) \\ &\quad \cdot \left[ 1 + \epsilon \frac{(t_{21} + t_{n1})(\Gamma_2 + |E_2|^2) + (t_{12} + t_{n2})(\Gamma_1 + |E_1|^2)}{t_{n1} t_{n2} + t_{21} t_{n2} + t_{n1} t_{12}} \right] \end{aligned}$$

and for (2.77) itself

$$\begin{aligned} \begin{pmatrix} N_1 \\ N_2 \end{pmatrix} &= \frac{1}{\epsilon Q_1 \epsilon Q_2 - t_{21} t_{12}} \begin{pmatrix} \epsilon Q_2 & t_{12} \\ t_{21} & \epsilon Q_1 \end{pmatrix} \begin{pmatrix} t_{1n} \\ t_{2n} \end{pmatrix} N_n \\ &= \frac{1}{\epsilon Q_1 \epsilon Q_2 - t_{21} t_{12}} \begin{pmatrix} \epsilon Q_2 t_{1n} + t_{12} t_{2n} \\ t_{21} t_{1n} + \epsilon Q_1 t_{2n} \end{pmatrix} N_n \\ &= \frac{1}{\epsilon Q_1 \epsilon Q_2 - t_{21} t_{12}} \begin{pmatrix} \epsilon (\Gamma_2 + |E_2|^2) t_{1n} + (t_{12} + t_{n2}) t_{1n} + t_{12} t_{2n} \\ \dots \end{pmatrix} N_n \end{aligned}$$

$$\begin{aligned}
\epsilon \left( \Gamma_2 + |E_2|^2 \right) t_{1n} + (t_{12} + t_{n2}) t_{1n} + t_{12} t_{2n} &= [(t_{12} + t_{n2}) t_{1n} + t_{12} t_{2n}] \\
&\quad \cdot \left[ 1 + \epsilon \left( \Gamma_2 + |E_2|^2 \right) \frac{t_{1n}}{(t_{12} + t_{n2}) t_{1n} + t_{12} t_{2n}} \right] \\
&\approx [(t_{12} + t_{n2}) t_{1n} + t_{12} t_{2n}] \frac{1}{1 - \epsilon \frac{\Gamma_2 + |E_2|^2}{t_{12} + t_{n2} + t_{12} \frac{t_{2n}}{t_{1n}}}}
\end{aligned}$$

$$\begin{aligned}
N_1 &= N_n \frac{(t_{12} + t_{n2}) t_{1n} + t_{12} t_{2n}}{t_{n1} t_{n2} + t_{21} t_{n2} + t_{n1} t_{12}} \\
&\quad \cdot \frac{1}{1 + \epsilon \frac{(t_{21} + t_{n1})(\Gamma_2 + |E_2|^2) + (t_{12} + t_{n2})(\Gamma_1 + |E_1|^2)}{t_{n1} t_{n2} + t_{21} t_{n2} + t_{n1} t_{12}}} \left[ \frac{\Gamma_2 + |E_2|^2}{1 - \epsilon \frac{\Gamma_2 + |E_2|^2}{t_{12} + t_{n2} + t_{12} \frac{t_{2n}}{t_{1n}}}} \right] \\
&\approx N_n \frac{(t_{12} + t_{n2}) t_{1n} + t_{12} t_{2n}}{t_{n1} t_{n2} + t_{21} t_{n2} + t_{n1} t_{12}} \\
&\quad \cdot \frac{1}{1 + \epsilon \left\{ \frac{(t_{21} + t_{n1})(\Gamma_2 + |E_2|^2) + (t_{12} + t_{n2})(\Gamma_1 + |E_1|^2)}{t_{n1} t_{n2} + t_{21} t_{n2} + t_{n1} t_{12}} - \frac{\Gamma_2 + |E_2|^2}{t_{12} + t_{n2} + t_{12} \frac{t_{2n}}{t_{1n}}} \right\}}
\end{aligned}$$

This is of the desired form

$$N_1 = N_n \frac{c_1}{1 + \hat{\epsilon}_1 (|E_1|^2 + \beta_1 |E_2|^2)} \quad (2.78)$$

where the relative magnitude of the timescales determine the coefficients  $c, \epsilon, \beta$ . An identical expression is found for  $N_2$ :

$$N_2 = N_n \frac{c_2}{1 + \hat{\epsilon}_2 (|E_2|^2 + \beta_2 |E_1|^2)} \quad (2.79)$$

The expressions in Eqns. (2.78)(2.79) are fixed points of the  $N_1$  and  $N_2$  populations respectively, due to the material gain. Therefore I define the normalised gain function as:

$$\hat{g}(N, E_i, E_j) = \frac{N c_i}{1 + \epsilon (|E_i^2| + \beta |E_j^2|)} \quad (2.80)$$

$$N g(E_i, E_j) = N \frac{c_i}{1 + \epsilon (|E_i^2| + \beta |E_j^2|)} \quad (2.81)$$

In this form, it is clear that the  $N$  contribution can be factored out, which will allow further simplification of Eq. (2.71). The hats are dropped from  $g$  for simplification.

### 2.2.3 Assembling the pieces

Using eq. 2.80 and the newly rescaled  $n$ , Eq (2.71) becomes:

$$\begin{aligned} 2N_{Thr}\dot{n} = & \Lambda - \Gamma_N N_{Thr} - \Gamma_N(2n)N_{Thr} \\ & - (2n + 1)N_{Thr}\frac{\mu}{\epsilon}[\hat{g}(E_1, E_2)|E_1^2| + \hat{g}(E_2, E_1)|E_2^2|] \end{aligned} \quad (2.82)$$

$$\begin{aligned} \dot{n} = & \frac{\Lambda - \Gamma_N N_{Thr}}{2N_{Thr}}\frac{\Gamma_N}{\Gamma_N} - \Gamma_N\frac{(2n)N_{Thr}}{2N_{Thr}} \\ & - (2n + 1)\frac{N_{Thr}\Gamma_N}{\Gamma_N 2N_{Thr}}\frac{\mu}{\epsilon}[\hat{g}(E_1, E_2)|E_1^2| + \hat{g}(E_2, E_1)|E_2^2|] \end{aligned} \quad (2.83)$$

$$\dot{n} = \Gamma_N[P - n - (2n + 1)\frac{1}{\Gamma_N 2}\frac{\mu}{\epsilon}[\hat{g}(E_1, E_2)|E_1^2| + \hat{g}(E_2, E_1)|E_2^2|]] \quad (2.84)$$

where the following variables have been introduced for simplification purposes:

$$\Lambda_{Thr} = \Gamma_N N_{Thr} \quad (2.85)$$

$$P = \frac{\Lambda - \Lambda_{Thr}}{2\Lambda_{Thr}} \quad (2.86)$$

$$(2.87)$$

In Eq. (2.84),  $E_n$  should now be rescaled by a factor of  $\sqrt{\frac{\mu}{2\epsilon\Gamma_N}}$ . The system is normalised such that at  $P = 0.5$  (twice  $\Lambda_{Thr}$ ) corresponds to the two-colour point, that is both modes of the laser are lasing with equal intensity. Further suitable rescaling of  $E_n$  and  $g$  is performed to absorb the frequency information in Eq. (2.36), as well with the rescaling of time as

$$\frac{\hat{t}}{\Gamma_E} = t \quad (2.88)$$

Propagating this time rescaling the  $E_n$  equation leads to a multiplicative  $\frac{1}{\Gamma_E}$  factor. Multiplying both  $E_n$  and Eq. (2.84) by  $\Gamma_E$ , and introducing:

$$\Gamma = \frac{\Gamma_E}{\Gamma_N} \quad (2.89)$$

produces the desired form of the two-mode semiconductor model.

$$\dot{E}_1 = E_1 \left[ \frac{1}{2} (1 + i\alpha) \{g(E_1, E_2)(2n + 1) - 1\} \right] \quad (2.90)$$

$$\dot{E}_2 = E_2 \left[ \frac{1}{2} (1 + i\alpha) \{g(E_2, E_1)(2n + 1) - 1\} \right] \quad (2.91)$$

$$T\dot{n} = P - n - g(E_1, E_2)(2n + 1)|E_1^2| - g(E_2, E_1)(2n + 1)|E_2^2| \quad (2.92)$$

Also, phenomenologically, a time-varying electric field is injected into  $E_2$  with the form:

$$E_{Inj} = K e^{-i\omega_{Inj}t} \quad (2.93)$$

and the frequency detuning  $\Delta\omega$  is defined as:

$$\Delta\omega = \omega_{Inj} - \Omega_{Thr} \quad (2.94)$$

are added to the rate equation model.

$$\dot{E}_1 = E_1 \frac{1}{2} (1 + i\alpha) \{g(E_1, E_2)(2n + 1) - 1\} \quad (2.95)$$

$$\dot{E}_2 = E_2 \left[ \frac{1}{2} (1 + i\alpha) \{g(E_2, E_1)(2n + 1) - 1\} - i\Delta\omega \right] + K \quad (2.96)$$

$$T\dot{n} = P - n - g(E_1, E_2)(2n + 1)|E_1^2| - g(E_2, E_1)(2n + 1)|E_2^2| \quad (2.97)$$

Traditionally, since there is a single injection into one mode, it is often useful to simplify Eqns. (2.95), (2.96), (2.97) as:

$$|\dot{E}_1| = \frac{1}{2} (g_1(2n + 1) - 1) |E_1| \quad (2.98)$$

$$\dot{E}_2 = \left[ \frac{1}{2} (1 + i\alpha) (g_2(2n + 1) - 1) - i\Delta\omega \right] E_2 + K_T \quad (2.99)$$

$$T\dot{n} = P - n - (1 + 2n) (g_1|E_1|^2 + g_2|E_2|^2) \quad (2.100)$$

$g_{1/2} = [1 + \epsilon (|E_{1/2}|^2 + \beta |E_{2/1}|^2)]^{-1}$ . Typical parameters for the numerical simulations (for example of size) are  $\alpha = 2.6$ ,  $P = 0.5$ ,  $T = 800$ ,  $\beta = 2/3$ , and  $\epsilon = 0.01$ . The experimental parameters have been established by previous work [66, 64].

Previously a rate equation model was derived for a single-mode optically injected semi-conductor laser[97]. In the absence of a second mode ( $E_1 = 0$ , implies  $\dot{E}_1 = 0$ ) the cross-saturation terms become 0 so the non-linear gain reduces to 1.

The system 2.99 reduces to:

$$\frac{d}{dt}E = (1 + i\alpha)NE - i\Delta\omega E + K \quad (2.101)$$

$$T\frac{d}{dt}N = P - N - (2N + 1)|E|^2 \quad (2.102)$$

as derived in [97], which is the well-known rate equation for single mode semiconductor laser undergoing optical injection.

### 2.2.4 Discussion of parameters

Among the several parameters used in the multi-mode laser model, are  $K$  and  $\Delta\omega$  which are arguably two of the more important parameters of the system. These parameters are directly controlled during experiments and have direct physical counterparts that we can perturb, interfere with and control completely. They allow us to create a window into the dynamical system of the optically injected semiconductor window.

#### 2.2.4.1 $\alpha$ : Line width enhancement factor.

The phase-amplitude coupling is introduced through the detuning parameter  $\alpha$ , or line-width enhancement factor. This value of the  $\alpha$  factor is representative of various physical properties of the semiconductor material including the refractive index.

#### 2.2.4.2 $T$

$T$  is the ratio of the electric field/carrier relaxation times. Analysing the limiting case of  $T \rightarrow 0$  allows the separation of the electric field from the population inversion. This will become important later on when fast-slow dynamics is important.

#### 2.2.4.3 $P$

The pump parameter  $P$

$$P = \frac{\Lambda - \Lambda_{Thr}}{2\Lambda_{Thr}} \quad (2.103)$$

can be determined experimentally by measuring the  $\Lambda_{thr}$  threshold current of the semiconductor laser, which is dependant on the temperature of the laser. This will be examined more thoroughly in Chap 3.

#### 2.2.4.4 $\epsilon$ : gain compression factor

This quantity controls the non-linear element of the modal-gain. At  $\epsilon = 0$ , the two-mode stability of the running laser does not exist and reduces to the single-mode system.

For finite  $\epsilon$  the non-linear gain allows the model to support the two-mode stability point in the free running laser ( $K = 0$ ). An extensive experimental study has already been carried out in [10, Chap. 3] and stability analysis has been conducted in[50] on the appropriate values of  $\beta$  for the cross saturation effect.

## 2.3 Bifurcations and dynamical phenomena

In the previous sections much emphasis was placed on the physics behind the behaviour of electron-hole pairs, population inversion and lasing in the semiconductor laser. Having motivated a system of differential equations to model the dynamical evolution of optically injected semiconductor laser, it is now appropriate to consider more rigorously the mathematical properties of these equations.

Let us therefore begin with an informal discussion of Eq. (2.100), which describes the time-evolution of the normalised population inversion. As this is a population evolution, one can expect certain (mathematical) similarities between our inversion population and other modelled populations, some of which are described below.

$$\dot{N} = N^2 - 1 \quad (2.104)$$

Eq (2.104) is a simplified equation that represents the flow of a population in time. This is a first-order (first time-derivative equation), non-linear ( $N^2$  term is non-linear) equation. The explicit time-dependence of the system has been removed (no  $t$  present in the equation) and therefore the system is called autonomous, as time is now considered as a separate variable.

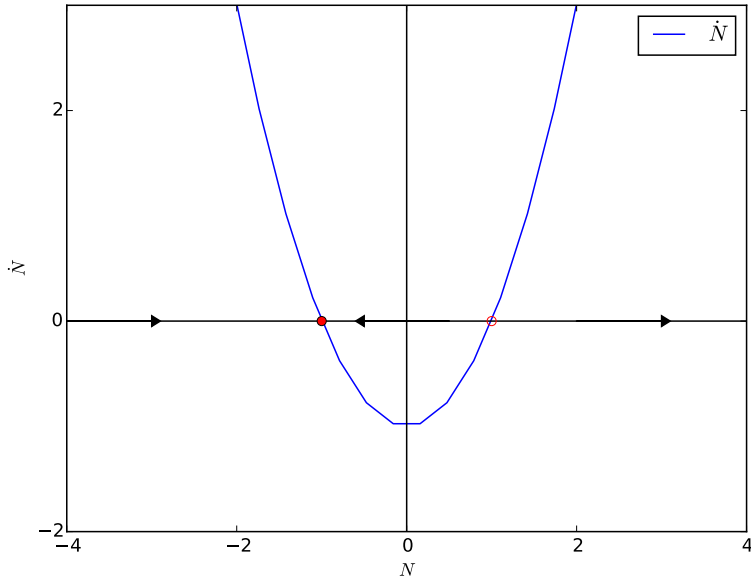


Figure 2.6: Black arrows denote direction of system, red circles denote fixed points of the system.

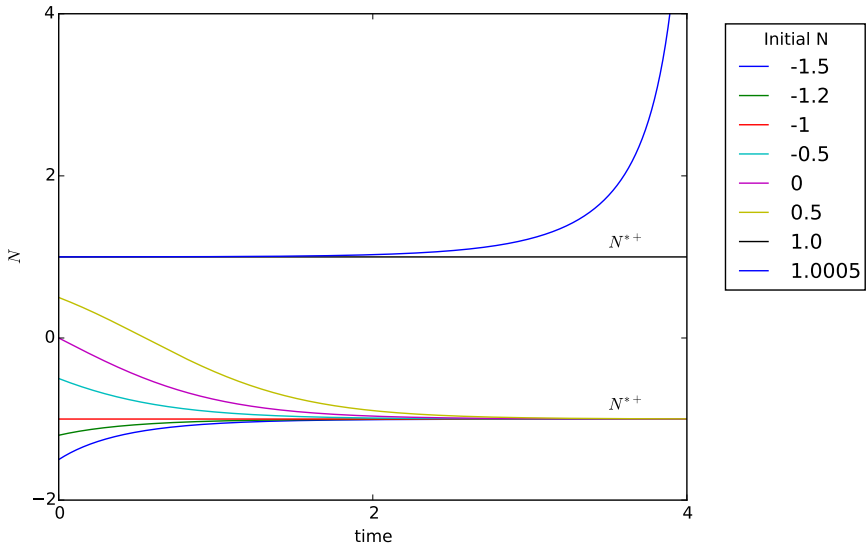


Figure 2.7: Shown are various trajectories of  $N$ , depending on initial conditions. The legend on the right states the initial condition for each trajectory.

In the study on non-linear differential equations, graphical aids, such as phase portraits are easier to consider than equations alone. Therefore I use Fig. 2.6, which depicts the *phase portrait* of our 1-dimensional system. In this diagram, it is imagined that our  $N$  flows along the real line with some velocity  $\dot{N}$ . The arrows denote the direction of the velocity. It is observed that the velocity (indicated in blue), passes through zero twice. In this set-up, the flow has both positive and negative velocities along the real line. The flow is said to be to the right while  $\dot{N} > 0$ , and to the left when  $\dot{N} < 0$ . When  $\dot{N} = 0$ , there is no velocity of the flow, and the population size does not change in time. This is called a fixed point. In Fig. 2.6, there are two such points, indicated with red circles (denoted as  $N^{*-}$  and  $N^{*+}$ , for the fixed points occurring at  $N = -1$  and  $N = +1$  respectively). However these fixed points have different stability, and their stability is perhaps best understood with reference to Fig 2.7. In Fig. 2.7 a number of trajectories are shown for various initial  $N$ .

The first observation made should be that trajectories near  $N^{*-}$  are attracted to the same trajectory as  $N^{*-}$  in finite time. In contrast, a trajectory starting very close to  $N^{*+}$  is repelling and the nearby trajectory moves away quickly without return. This concept of attractiveness, where we consider time as  $t \rightarrow \infty$ , is called *Lyapunov stable*[84, p.129], if all trajectories starting sufficiently close to  $N^{*-}$  remain close to  $N^{*-}$  for all time. By the opposite argument,  $N^{*+}$  is called unstable, as nearby trajectories do not remain close by for all times.

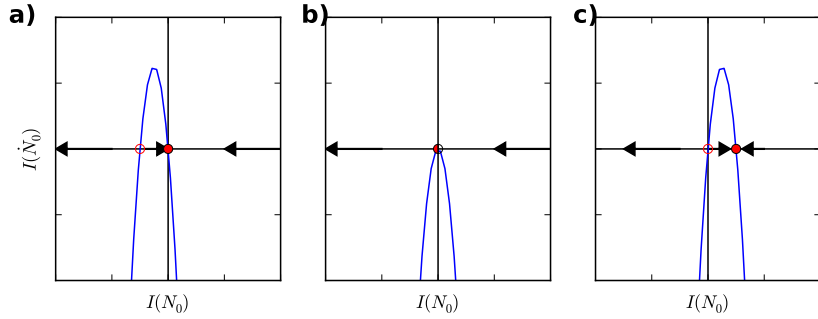


Figure 2.8: Phase portrait for  $\dot{I}$  vs.  $I$ . a)  $N_0 < \frac{k}{G}$  b)  $N_0 = \frac{k}{G}$  and c)  $N_0 > \frac{k}{G}$ . Physically, a negative intensity (number of photons) is meaningless, but is included here to account for the stability exchange as  $N_0$  is varied. The fixed points are marked with circles and their stability is noted with a solid red (stable), empty circle (unstable) or half-stable (half-fill).

### 2.3.1 Transcritical Bifurcation

Let us now consider a more complicated equation. In the laser system, there are other time-varying quantities to consider. Our model has been normalised such that the population inversion occurs at  $N = 0$ . For the sake of generality, let us assume an unnormalised rate equation for  $I$  (photon intensity,  $E = \sqrt{I}$ ) and  $N$ :

$$\begin{aligned}\dot{I} &= \text{Gain} - \text{Loss} \\ &= GIN - kI\end{aligned}\tag{2.105}$$

and

$$N(t) = N_0 - \alpha I\tag{2.106}$$

Substituting Eq. (2.106) into (2.105) yields a first order equation which can be analysed graphically.

$$\dot{I} = (GN_0 - k)I - (\alpha G)I^2\tag{2.107}$$

Previously, Eq. (2.104) had two fixed points defined as  $\pm 1$ . While Eq. (2.107) also has two fixed points:  $I = 0$  and  $I = \frac{GN_0 - k}{\alpha G}$ , one of which depends on non-specified constants. This leads us to three separate phase portraits for Eq (2.107) which depend on  $N_0$ .

Depending on the value of  $N_0$ , three different scenarios arise. For  $N_0 < \frac{k}{G}$ , the phase portrait says the non-trivial fixed point is negative and unstable. For  $N_0 = \frac{k}{G}$ , the system has a two-fixed points at 0 and c)  $N_0 > \frac{k}{G}$  shows that the

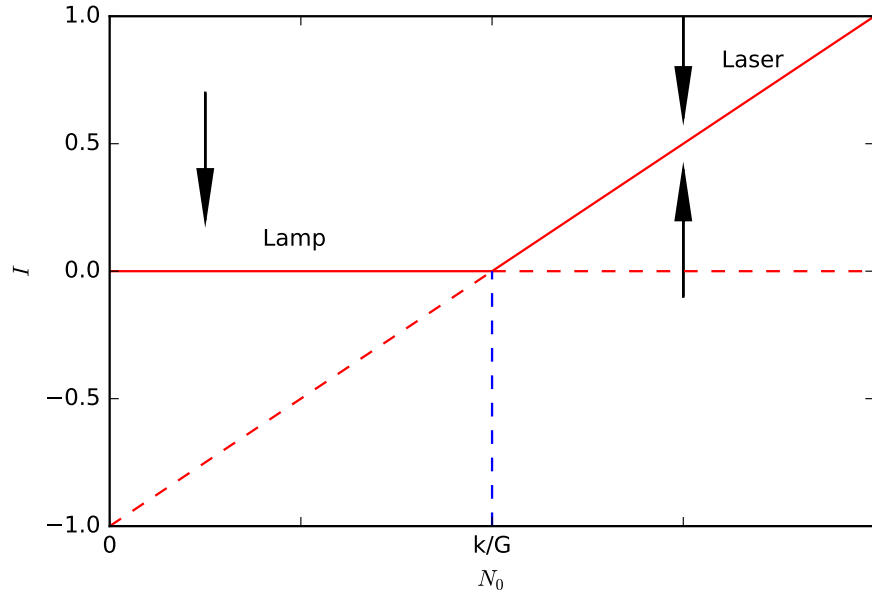


Figure 2.9: [84, p.55] For  $N_0 < \frac{k}{G}$ , the emitted photons behave like a lamp with a zero average intensity. At  $N_c$ , the stable fixed point becomes non-zero due to the transcritical bifurcation. The arrows indicate the flow of the system, which is 'attracted' towards stable points. When a qualitative change occurs due to a variation of the control parameter, a bifurcation is said to have occurred.

non-trivial fixed point is now positive and stable, while the zero fixed point is now unstable (previously stable). The conclusion drawn here should be that our phase portrait is parameter dependant, and that when certain parameters conditions are satisfied a transition between phase portrait scenarios occurs. A qualitative change in a dynamics of a phase portrait is called a *bifurcation* and occurs when a bifurcation parameter ( $N_0$  for the current model), passes through a critical point ( $N_0 = \frac{k}{G}$ ). In the case here, the bifurcation resulted in an exchange of stability when the fixed points collided.

The stability exchange is due to *Transcritical Bifurcation* as the control parameter  $N_0$  passes through a critical value:  $N_c = \frac{k}{G}$ . In Fig 2.8(b), the exchange of stability occurs when the unstable and stable fixed points collide at  $N_0 = N_c$ , to form a *half-stable* point, and then separate (with different stabilities) as  $N_0$  is changed further.

Fig. 2.9 depicts the stability and magnitude of fixed points of  $I$ .

The stable fixed point grows linearly with the population inversion and it should now be apparent that  $N_c$  is in fact the lasing threshold  $N_{Thr}$ . The transcritical bifurcation does not change the number of fixed points in a system (outside of the critical value of  $N_{Thr}$ ) but allows fixed points to collide and exchange sta-

bility. The stability of a fixed point can change at  $N_c$ . The normal form of the transcritical bifurcation is

$$\dot{x} = rx - x^2 \quad (2.108)$$

### 2.3.2 Pitchfork Bifurcation

#### 2.3.2.1 Supercritical

The next simple bifurcation arises from considering the magnitude of the  $E$  field. Using  $E = \sqrt{I}$  and Eqn (2.107):

$$\begin{aligned} E &= \sqrt{I} = I^{\frac{1}{2}} \\ \dot{E} &= \frac{1}{2}I^{-\frac{1}{2}}\dot{I} \\ \dot{E} &= \frac{1}{2I^{\frac{1}{2}}}\dot{I} \\ \dot{E} &= \frac{1}{2E}\dot{I} \\ &= \frac{1}{2}E\{(GN_0 - k) - aGE^2\} \end{aligned} \quad (2.109)$$

which is the *supercritical pitchfork bifurcation* and has the normal-form:

$$\dot{E} = E(r - E^2) \quad (2.110)$$

and  $r = \frac{GN_0 - k}{aG}$ . Fig 2.10 depicts the fixed points of  $\dot{E}$  as  $r$  is varied. For  $r \leq 0$  the system has only the (stable) fixed point at zero. This is consistent with the dynamics described in Sec: 2.3.1, namely that below  $N_c$  (and  $r \leq 0$ ) the laser acts as lamp with no organised stimulated emission of photons. Unlike the transcritical bifurcation, fixed points can be created (or annihilated). This is precisely what happens for the pitchfork bifurcation. When  $r > 0$ ,  $N_0 > \frac{k}{G}$  and the stable fixed point at zero breaks up to form an unstable fixed point at zero, and two stable fixed points that vary as  $E(N_0) = \pm\sqrt{\frac{GN_0 - k}{aG}}$

#### 2.3.2.2 Subcritical

In Sec. 2.3.2.2, the normal form of the supercritical pitchfork bifurcation has a negative cubic term. This acts as a restoring force that pulls  $E$  back towards 0. However if we change the sign of the cubic term in Eq. (2.110) we obtain the

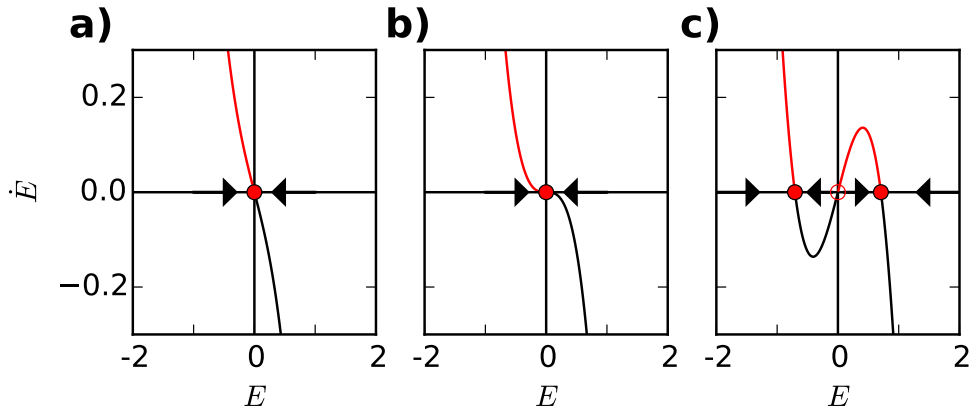


Figure 2.10: Phase portrait with fixed points (and their stability indicated using the standard notation) as the control parameter  $r$  is varied: a)  $r < 0$  b)  $r = 0$  and c)  $r > 0$  respectively.

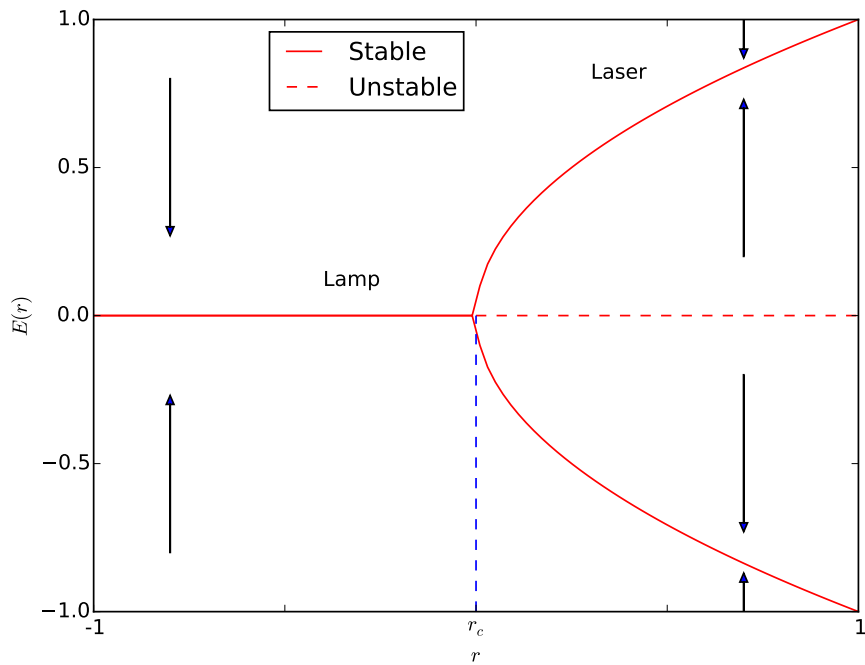


Figure 2.11: Bifurcation diagram for the pitchfork bifurcation. At  $r = r_c = 0$  (critical value of  $r$ , and is zero in the normalised form) a pitchfork bifurcation occurs and two stable non-zero fixed points occur. The previously stable fixed point at 0 is now unstable. The arrows indicate the flow of system and a qualitative change occurs at  $r_c$  indicating the bifurcation has occurred.

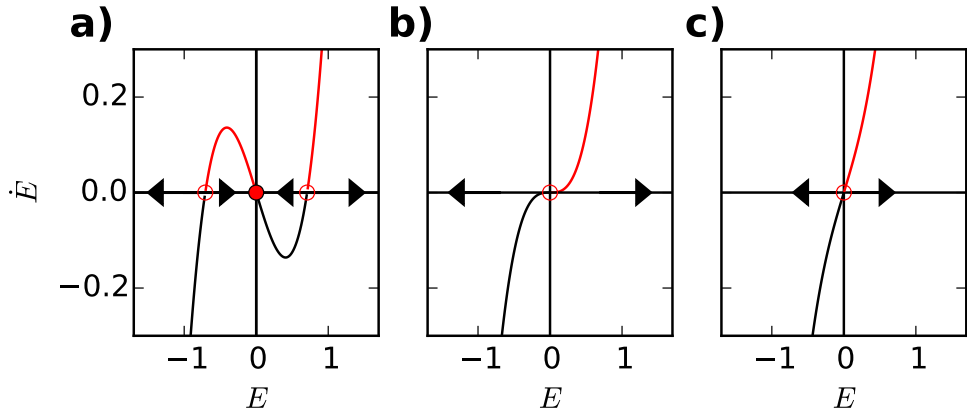


Figure 2.12: Phase portrait with fixed points (and their stability indicated using the standard notation) as the control parameter  $r$  is varied: a)  $r < 0$  b)  $r = 0$  and c)  $r > 0$  respectively.

*subcritical pitchfork bifurcation* which has the normal-form:

$$\dot{E} = E(r + E^2) \quad (2.111)$$

Examining phase portraits of Eq. (2.111) in Fig. 2.12 show that the stability of the fixed points have changed. As a result, changing the sign of the cubic term means the system has undergone a bifurcation as there is a qualitative change in the system's phase portraits.

The bifurcation scenarios discussed here, and many more, exist in the multi-mode laser device. More of these will appear in later chapters as experimental observations (such as a Hopf bifurcation and period doubling bifurcation). The undergraduate book by Strogatz[84] provides a full course on non-linear dynamics with examples in lasers, physics, biology and engineering.

## 2.4 Literature Review

The subject matter of this thesis is an extensive study into optically injected multi mode semiconductor lasers. This requires investigating the existing theoretical treatments of optically injected lasers and previous mapping techniques used to analyse experimental time-series. The existing literature in this field is quite extensive and therefore this section is merely a summary of existing work to place this thesis in the correct scope based upon the research goals undertaken. For this reason the literature will be divided into three sections: theoretical models, experimental mapping techniques and rogue wave dynamics. The first two subsections refer to the treatments undertaken (theoretically and experimentally) previously (with a brief summary/comparison of their suitability to this thesis) and the the third section refers to the works already done in the area of identifying and the studying optical rogue wave phenomena.

### 2.4.1 Theoretical Models

Many theoretical approaches have been taken in order to capture the intricate and complex behaviour of semiconductor laser. With each modelling decision, typically one aspect or characteristic of the underlying structure is chosen often at the expense of another. A careful balancing act of approximations and assumptions are made based on a desirable form of equations, simplification of parameters based on empirical experimental knowledge. For example, in White et al. [92], a Travelling Wave Model (TWM) approach is taken to a model an optically injected two-mode semiconductor laser and has shown good agreement with experiment. The model is presented in the form of a second order Partial Differential Equation (PDE) for the forward and backward fields. The model captures important dynamical properties including mode hopping and boundary conditions are used to select the contributing modes. The TWM are successfully applied in homogeneous and periodically modulated cavities. However TWM can be problematic in the case of more complicated devices with aperiodic reflective features in the cavity. In the case of the lasers utilised in this thesis, this approach therefore is not suitable as each slot would contribute a new source of reflection and the system of equations would then grow enormously. Additionally, travelling wave models are not easily amenable to the tools of non-linear dynamics such as bifurcation analysis and numerical continuation. Therefore, a spatially independent rate equation model subject to external optical injection is preferred.

When considering the existing contributions to optically injected semicon-

ductor lasers using rate-equation models, significant work has been done in both single-mode and two-mode lasers. Some of the early work is described here briefly. Moving beyond the model characteristics, Solari et al.[81] made leading efforts to develop the initial bifurcation diagrams of the optically injected laser. In Solari et al. [81] they utilise bifurcation theory to establish the existence of fixed points, periodic orbits and tori and confirm their results with computer simulations of the rate equation model. They introduce flow pattern diagrams which are parameter dependent and discuss the importance of the detuning between the cavity and atomic frequencies.

In Wieczorek et al. [93], the results go further and they describe the various regions bounded by bifurcation lines detected using nonlinear tools. These lines included Saddle-Node, Hopf, Period-Doubling, Saddle-Node of limit cycles and Torus bifurcations. Simulations were performed on a three dimensional rate-equation model subject to optical injection, for various linewidth enhancement factors ( $\alpha$ ) values. Their results culminated in the first global stability diagrams. Previous to this, only partial diagrams or small parameter region mappings were available. The persistence of the bifurcation lines under parameter changes demonstrates the robustness of bifurcation analysis. Their work was mostly involved with single mode optically injected lasers, but it is an aim of this thesis to extend this work to two-mode lasers.

Moving to two-mode rate-equation laser models, Kawaguchi et al. [40] employs a two-mode rate equation model without optical injection and focuses on the the existence (and stability) of a two-mode equilibrium region (often referred to as a two-colour point). It is shown that the stability of the two-colour point is dependent on the self and cross saturation terms, which are in turn affected by the separation of the two primary modes. For our model, the parameter of the self and cross saturation terms were chosen to yield a stable two-colour point with equal intensities in the free-running laser. Similar to our model, Kawaguchi also uses a single shared population inversion for the two Transverse Electric (TE) and Transverse Magnetic (TM) modes present. The modal competition is modelled in Kawaguchi et al. [40] by including the field intensities in the numerator of the non-linear gain. Both models agree in the first order of the nonlinearity parameter  $\epsilon$ . However, Kawaguchi does not include an optical injection term which is necessary for this this thesis.

In Simpson et al. [79] a DFB laser with optical injection is studied. While the free running laser is almost perfectly single mode, it is shown that through optical injection side modes (at a distance of the relaxation oscillation frequency)

side can have significant magnitudes. The effect can be modelled on the basis of a multi-mode rate equation model, where the additional mode is closely coupled with the primary mode. This is different to our model where the two primary lasing modes coexist in the free running case. Also the close coupling in Simpson et al. [79] does not allow for a straightforward expansion to lasers with a higher number of lasing modes. This renders this model unusable for our setup.

In an effort to describe the behaviour of an optically injected VCSEL Gatare et al. [30] utilises a model with two modes corresponding to  $x$  and  $y$  polarisations (of the fields) and two carrier variables. This yields a complex six dimensional model. They were successful in capturing many of the expected bifurcation scenarios that exist in the VCSEL system. Both modes are mutually coupled in both phase and amplitude. The structure of this model is similar to ours if the second carrier variable vanishes, however there is a direct dependence of the amplitude of each polarisation mode with each other. This explicit cross-dependence does not allow for an easy extension to a higher number of lasing modes.

Krstic et al. [46] investigates a multimode Fabry-Pérot (FP) laser with optical injection. In their setup optical injection occurs into the side mode and the form of their model is similar to ours with a low-dimensional rate equation model, albeit they have a linear gain dependence on the lasing photon density. Their comparison of results are quite promising as they demonstrate numerically and experimentally the presence of a bistability in laser devices. However, a larger comparison of theory and experiment is needed in the form of a full parameter sweep and dynamical feature mapping for our edge-emitting device.

Finally, in Ogita et al. [62] a similar approach was introduced for lasers with a large number of longitudinal modes. Their model is a low-dimensional ( $n + 1$  equations for  $n$  lasing modes) rate equation model with a unified population inversion and is explored specifically for a two-mode and twenty-one mode laser. The experimental and theoretical comparisons consider transient dynamics entirely and external optical injection is not utilised or modelled. The lack of optical injection places a limit on their model, however it has a similar form to our model (up to the missing optical injection). Furthermore, they do not generate stability maps of bifurcation analysis for either of the multi-mode laser configurations.

From analysis of the existing literature, the model presented in this thesis has been shown to be previously useful in both single-mode and multi-mode devices. However there are still contributions that can be made using this model, one such example is the extended stability and bifurcation mapping of two-mode optically injected lasers. While the literary review is not intended as a place to judge

relevant work on scale of best-to-worst, it does allow for brief overview of the existing research to adequately place this thesis in the scope of existing work and highlight the differences and most importantly the contributions to science.

### 2.4.2 Experimental Mapping Techniques

Given access to both a powerful theoretical model and a optically injected semiconductor device, experiment-theory comparisons are a natural development. For an optically injected laser there are two natural (and easy) parameters to vary:  $K$  and  $\Delta\omega$  (the injection strength and detuning from the free running laser respectively). In this thesis, a dynamical systems mapping technique was developed for two-mode optically injected lasers. This technique is introduced in a way which is scalable for lasers with a larger number of lasing modes. With this technique the complete two-mode equilibrium (locked injected mode and free-running uninjected mode) was mapped out for positive detuning. To the best of the author's knowledge this is the first experimental confirmation of this dynamical region. Previous work in this area were focused on single-mode lasers predominately, or their dynamical mapping techniques were not easily extendable to semiconductor lasers with a larger number of lasing modes. A selection of mapping techniques are discussed below. In Eriksson et al. [21, 20], a single-mode optically injected semiconductor laser (with multiple quantum wells) is studied in a master-slave approach. They discuss briefly the previous successes of using a master-slave configuration for optically injected lasers. This includes detecting many elements of nonlinear dynamical systems in physical systems, such as period doubling routes to chaos. For the optical injection they have chosen to vary the optical intensity and frequency separation from the free running state. In both papers they present experimental stability diagrams (for various laser current values in [20]) however it is always a laser operating in a single-mode regime. Additionally, there is no theoretical stability map generated for comparison.

Simpson et al. [79] and Wieczorek et al. [98] performed a complete theoretical and experimental analysis of the single-mode laser. In their work a low-dimensional rate equation model was used to model the expected laser behaviour and was overlaid across the experimental results. The experimental results here were in fact the first experimental stability diagrams (obtained from the optical spectra) and demonstrated strong agreement with the theory.

Ideally, for a multi-mode laser the mapping technique should be reasonably fast, automatic and scalable according to the number of modes lasing in a laser. Therefore we consider a few automatic mapping techniques in the literature. In

Toomey et al. [87] automated algorithms were produced to determine the various boundaries between dynamical regimes of optically injected VCSELs. However they do not expand on the details of their algorithms but describe the quantities used for dynamical classification such as peak-to-peak amplitudes and mean intensity. These quantities can be used for classifying lasers with a higher number of modes with algorithms.

In their later work, Toomey et al. [85] introduce a more complicated dynamical classification system using permutation-entropy for mapping a semiconductor laser subject with optical feedback. Their two-dimensional parameter maps are then presented in terms of injection current vs feedback (Acousto-optic modulator transmission). This presents a technique formed to characterise the unpredictability of the system (chaos) but possible not all other dynamical regimes of the system. For our system, we desire a complete dynamical regime identification for a multi-mode device. In an effort to form a completely automated correlation tool for an optically injected semiconductor laser, Toomey et al. [86] describe their automatic correlation algorithm which utilises time-series information in the two-dimensional  $K$ - $\Delta\omega$  plane. The optical injection occurs from a similar semiconductor laser in a master-slave setup. The entire setup, although described for a single-mode laser can be extended to multi-mode lasers, where a complete complex dynamical behaviour identifier can be formed using time-series information from all of the recorded modes. This is the motivation behind our experimental setup and mapping technique.

### 2.4.3 Optical Rogue Waves

With a long and exhaustive history of study, one could perhaps consider the single-mode optically injected laser as well understood; however, recently Bonatto et al. [8] and Zamora et al. [101] have identified rare, large amplitude excursions in (single-mode) semiconductor lasers which have yet to be satisfactorily explained. These phenomena have been labelled Rogue Waves (RW) and their name originally comes from the oceanographic problem of rare, random large amplitude events that 'appear and disappear randomly without a trace' [3]. In [8, 72] it has been shown that the large amplitude events are predicted by a rate equation model and also have been experimentally observed. In Chap. 4 it is shown that the rate equation model in [8, 72] is equivalent with the model used in this thesis under a re-scaling.

The relationships between noise and the mean-time between RW events has been discussed in [72] and it was established that noise can be used to either en-

hance or suppress the occurrence of RM events. Experimental time-series and bifurcation diagrams are generated for their optically injected VCSEL that demonstrate experimentally the existence of rare, large amplitude events. They generate Lyapunov exponents diagrams and overlay locations where RW events have been detected in simulated time-traces. Predominately the RW events occur in chaotic regimes. Given that RW events are expected to be random, an investigation into the randomness of the RW events is presented in this thesis and the mean-time between events could be explored as a function of  $K - \Delta\omega$ . This could yield a clearer understanding into what happens near or at the chaotic boundaries. Additionally, there are histogram plots presented that show a distinct gap in the amplitude spectrum of the local maxima of the fields. It is not clear if this is just a result of the length of the time-trace taken and may in-fact be filled if the time trace was run for longer (In [8] it is stated that they 'cannot exclude the existence of physical mechanisms that result in a nearly forbidden "gap"').

In Perrone et al. [72] and Ahuja et al. [2] the dependence on current modulation and phase modulation are explored and are shown to have a complex relationship with RW occurrence. In both of these papers, the role of direct current modulation and modulation phase are studied in an attempt to enhance or suppress RW events. A strong analytical approach is still needed to understand the origins of such events.

In Zamora et al. [101] it is demonstrated that RW events can be predicted several  $ns$  in advance. They also investigate the contribution of the fixed points (saddle and unstable foci) in the generation of RW events. It is noted that on the path to a RW event the system travels very close to the stable manifold of the saddle-focus. This merits further study and an analytical investigation is desirable to determine the causes and requirements of a RW event. In this thesis, surface plots are generated in an attempt to explain the origin and path of the RW event, these are referred to as the 'chimney' and 'spike' plots in Ch. 4. A path leading to the onset of a RW is discovered through the chimney and spike structures, but the mechanism that forces the laser onto this path is still not fully understood. Also the rarity and randomness are RW's are understandable given the narrow window for RW's close to the origin and the difficulties associated with staying close to the origin. An analytic solution for the path of the RW near the upper unstable focus is sought by revisiting the spike structure and it is shown that the RW diverges from that saddle-node trajectory. Based on the literature examined above, Ch. 4 contributes in furthering the knowledge of RW events through identifying a window through which a RW can be generated, but

the origins of the RW event remain elusive.

# **Chapter 3**

## **Dynamical classification of optically injected lasers**

### **Abstract**

We present a reliable and fast technique to experimentally categorise the dynamical state of optically injected two mode and single mode lasers. Based on the experimentally obtained time-traces locked, unlocked and chaotic states are distinguished for varying injection strength and detuning. For the two mode laser, the resulting experimental stability diagram provides a map of the various single mode and two mode regimes and the transitions between them. This stability diagram is in strong agreement with the theoretical predictions from low-dimensional dynamical models for two mode lasers. We also apply our method to the single mode laser and retain the close agreement between theory and experiment.

## 3.1 Motivation

In the previous chapter, devotion was given to motivating the rate equation model for the optically injected two mode laser. It has been previously shown that this model reveals a wealth of dynamical behaviour[67, 63]. As the ultimate ambition in developing a mathematical model is in the application, a comparison is sought with the experimentally observed behaviour of the optically injected laser.

In this chapter, the method and results of the experimental investigation into a two-mode and single-mode laser are presented. These particular devices, while unique in design, are excellent examples of typical optically injected semiconductor lasers.

In [61, 60] a Fabry-Perot inspired multi-mode semiconductor laser was developed to generate stable two-mode operation in a free-running semiconductor laser. This device was developed in conjunction with Eblana Photonics, and the separation between lasing modes was shown to be tunable over a large range of frequencies. Traditional methods of optically synthesising these frequency ranges involve mixing the outputs of two single mode semiconductor lasers [56]. While this is a simple and easily implemented approach, it presents unavoidable drawbacks. As the output of the source lasers are uncorrelated, a broadening of the frequency difference line-width occurs. Several techniques, including an optical phase locked loop feedback mechanism, can be employed to improve the line-width resolution. However this adds to the complexity of the experiment[83, 26].

Other methods of optically generating these wavelengths include external cavity lasers[70] and compound cavity designs[100, 43]. However, the devices studied here are prototypes which do not utilise external or compound cavities. The key aspect of these devices is a spatially varying refractive index profile, which is optimised according to the desired spectral output of the laser. The design of these lasers is not part of this thesis and therefore will not be included here. Moreover, the underlying mechanism of laser design is often of secondary importance compared to its operation and behaviour. Therefore, a simple method of device characterisation is sought based upon an intuitive control parameter variation. In the case of the optically injected laser, the natural control parameters are the  $\Delta\omega$  and  $K$  (the injection detuning and strength as defined in Chap. 2). As these parameters are varied, the dynamics of the injected laser will vary accordingly. It is expected, based on past experimental single-point measurements, and theoretical mapping, that different regions of dynamical behaviour are present in these devices. In mathematics, a bifurcation (Sec. 2.3) is used to denote a change in the phase portrait of a system when some condition has been met. This quantitative

change can be seen as the change in the number of fixed points in the system, or a change in the stability of a fixed point. Experimentally (and numerically) systems will only follow the stable solution. Therefore, our characterisation technique will rely on recording the system as it tends towards a stable solution, and the interpretation of changes in stability of the laser, as a function of  $K$  and  $\Delta\omega$ . The regions of different dynamics will then be identified according to a stability measurement performed over a 2-D parameter mapping of  $K$  and  $\Delta\omega$ .

## 3.2 Introduction

The experimental acquisition of a two-dimensional stability diagram therefore involves characterising the optical output of the laser for varying  $K$  and  $\Delta\omega$  [29, 79].

Here we demonstrate an experimental technique, which uses a fast (i.e. within  $10\mu s$ ) modulation of the injection strength  $K$  for fixed  $\Delta\omega$  and simultaneously record the time trace of the optical output. This allows for a characterisation of the dynamical state for varying injection strength with high accuracy. The procedure is then repeated for varying values of  $\Delta\omega$ . Therefore a complete sweep of the overall  $K$ - $\Delta\omega$  plane is completed.

The impact of this method is demonstrated for Two Mode and Single Mode lasers. The resulting experimental stability diagrams show parameter regions of different dynamical behaviour in excellent agreement with theoretical rate equation models [97, 65, 64].

The main results in this chapter were previously published in Optics Express[68]. This chapter is divided into the following sections:

Sections 3.3 to 3.4 explain the experimental technique, Section 3.5 and 3.6 describes the routines derived to characterise the dynamical behaviour of the laser, and to classify a state as on, off, locked, unlocked or some combination thereof. Section 3.6 then presents the complete experimental  $K$ - $\Delta\omega$  stability diagram and discusses the accuracy of the experimental results with their numerical counterparts. Finally, Sec. 3.10 includes some previously unpublished results on bi-stability measurements.

## 3.3 Outline of experiment

Fig. 3.1 depicts the setup for the experiment. The master laser (injecting laser), is a low line-width, wavelength tunable coherent light source that operates in the

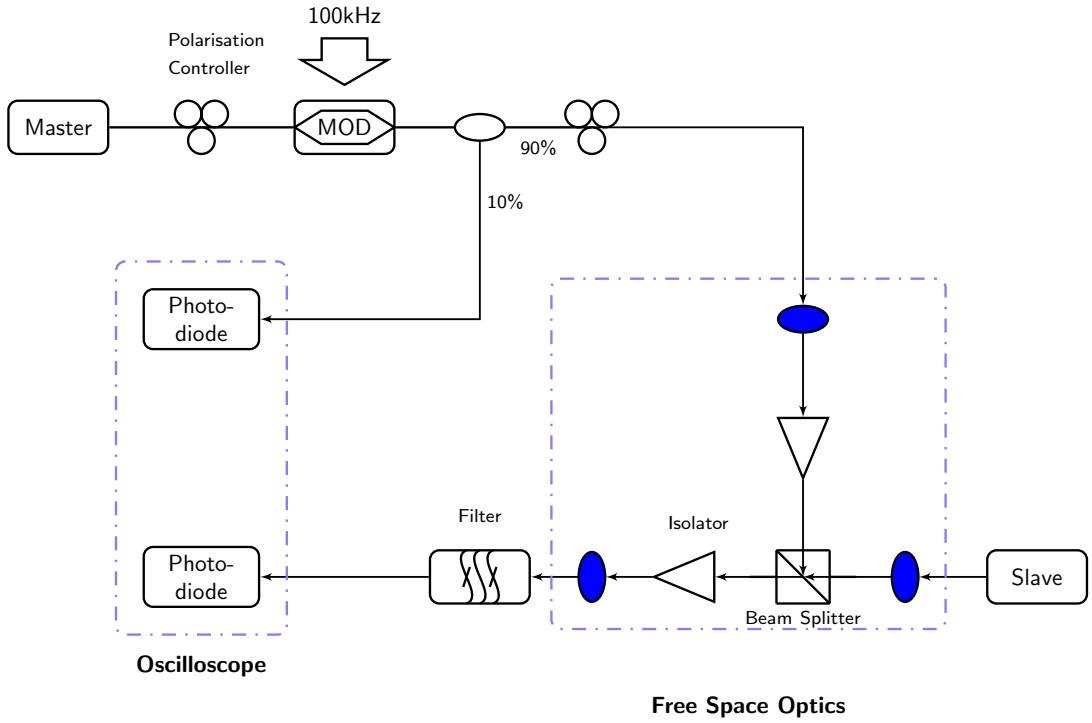


Figure 3.1: Diagram of Experiment:

1550 nm range, with a maximum power output of 4.2 PW and the slave-laser is a two-mode semiconductor laser[63, 59] (The method here is explained for the two-mode laser, but is easily adapted for the single-mode laser.).

The detuning of the master laser ( $\Delta\omega$ ) is increased incrementally with a step size of the order of 0.001nm and is controlled via a mechanical apparatus inside the master laser device. The modulation of  $K$  is performed via an electrical sinusoidal signal (100kHz) acting on a photo-crystal. Therefore, as  $K$  is a smoothly varying experimental parameter the decision was made to fix  $\Delta\omega$  while  $K$  is modulated. The polarisation controller was a Thor-Labs FPC030 device in which the optical fibre went through an azimuthal twisting to induce a polarisation change in the wave travelling along the optical fibre. The polarisation is adjusted in two places in the optical circuit: 1) Immediately before the injected light is coupled with a 100kHz sinusoidal wave generated by a photonic crystal, and 2) immediately before the injected light leaves the optical fibre (and immediately after passing through a 90: 10 beam splitter) and enters the free space section of the circuit.

The polarisation is adjusted in the first instance to ensure maximum coupling of the 100kHz signal with the injected light, and in the second instance to ensure that the modulated injected wave has maximum interaction with the slave laser

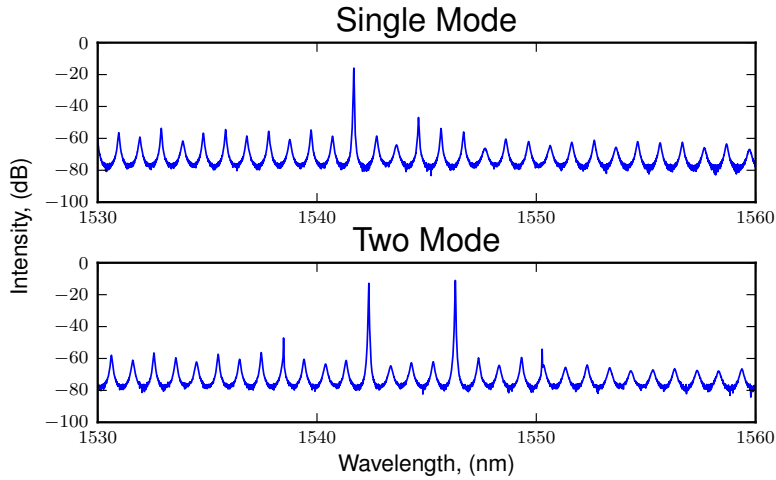


Figure 3.2: Optical Spectra of (a) Single-Mode and (b) Two-Mode laser

output in the free-space optics (this second adjustment also accounts for any change in polarisation due to a change in medium when going from glass to air).

The ideal polarisation is set by ensuring that an amplitude locking can be achieved with an optical injection at  $-8\text{GHz}$ . This detuning was chosen for several reasons: the majority of the dynamics that are of interest exists above  $-8\text{GHz}$ , and the limiting bandwidth of our photo-detector is  $8\text{GHz}$ . Once amplitude locking can be obtained at this point, locking can be attained at lower detunings where possible.

Once the polarisation is set, it remains constant for the entirety of the experiment (up to a significant change in laboratory conditions). The apparatus was isolated from air conditioning and secured on an anti-vibration table to ensure stable laboratory conditions.

10% of the modulated injected light is recorded directly via a photo-diode for reference. The remaining 90% of light is then injected into the optical output of the slave laser. The beam is divided by a standard 90: 10 beam-splitter.

The slave laser is temperature stabilised to within  $\pm 1\text{ mK}$  (using a Peltier cooler). The spectral output of the free-running (no injection) slave laser at a temperature of  $21.7^\circ$  and twice threshold is shown in Fig 3.2. The temperature dependence of the threshold current and the two-colour point are measured in the next section, as part of the pre-experiment setup measurements.

### 3.3.1 Measuring Threshold and Temperature Selection

The lasing threshold corresponds to the lowest current at which the output of the laser is dominated by stimulated emission (rather than spontaneous emission). This occurs above the transparency current which signifies the onset of a population inversion. The threshold current  $J_{Thr}$  (which is the experimental counterpart of the dimensionless inversion  $\Lambda_{Thr}$ ) is easily measured experimentally for a range of temperature values. The semiconductor laser is expected to operate in a room-temperature environment and will experience a temperature increase due to Joule heating from the electrical pumping. Therefore the standard operating temperature range should be of the order  $20 - 24^\circ C$ . The pump current  $J$  is slowly increased in  $mA$  until a considerable amplitude is achieved by one of the primary modes, as depicted in Fig. 3.2. The onset of lasing occurs when the threshold current,  $J_{Thr}$ , is passed. In terms of experimental quantities the normalised pump parameter from equation (2.103) is given by

$$P = \frac{J - J_{Thr}}{2J_{Thr}}. \quad (3.1)$$

For the two-mode laser, the pump current is increased until the second mode achieves an equal magnitude in the optical spectrum. In Fig. 3.2 (bottom panel), it is observed that both modes lase with an equal intensity of  $-20dB$  (log scale), and therefore we are satisfied that the intensities are equal. The value of pump current in this situation is the two-colour point ( $J_{2C}$ ).

The quantities  $J_{2C}$  and  $J_{Thr}$  are now explored as functions of temperature. Fig. 3.3 shows the data points recorded for the  $J_{Thr}$  in red, and  $J_{2C}$  in black. The temperature was increased in steps of  $0.5^\circ C$  and the system was allowed to relax before recording the new current values. A line of best fit is applied to both data points and depicts a strong linear relation between  $J_{2C}$ ,  $J_{Thr}$  and temperature. Using Eq. 2.103 the normalised pump parameter  $P$  can be calculated, and is depicted in Fig. 3.4.

A normalised  $P$  is desired, such that the laser operates at the two-colour point and is well above the threshold current,  $J_{Thr}$ . For convenience  $J_{2C}$  is set to be twice  $J_{Thr}$ . Using Eq. 2.103,  $P$  is therefore set to be 0.5. In Fig 3.4, the red dot indicates the interception of  $P = 0.5$  with the line of best fit. The red dashed line marks the corresponding temperature required which is shown to be  $21.75^\circ C$ .

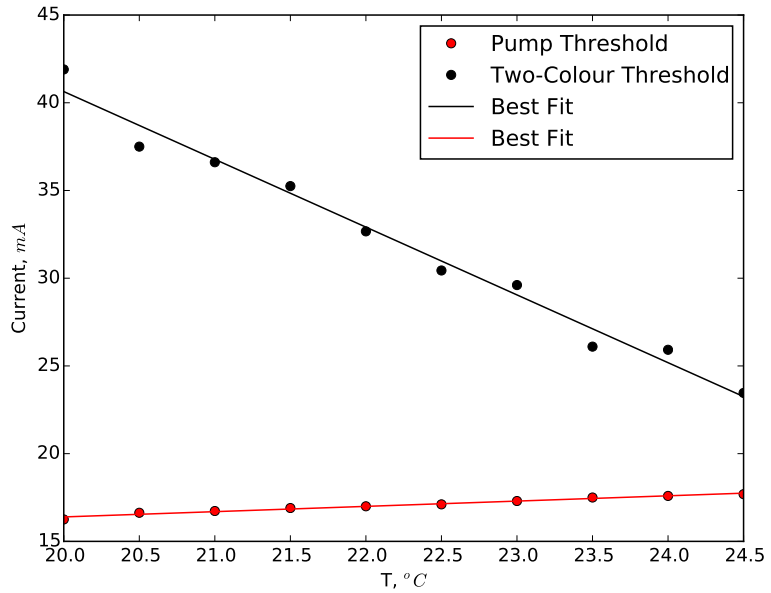


Figure 3.3: Threshold Current (Blue) and Two-Colour Point Current (Green) measured as the temperature is varied. The measurements were taken over the course of a day, providing the semiconductor laser ample time to stabilise after a temperature change.

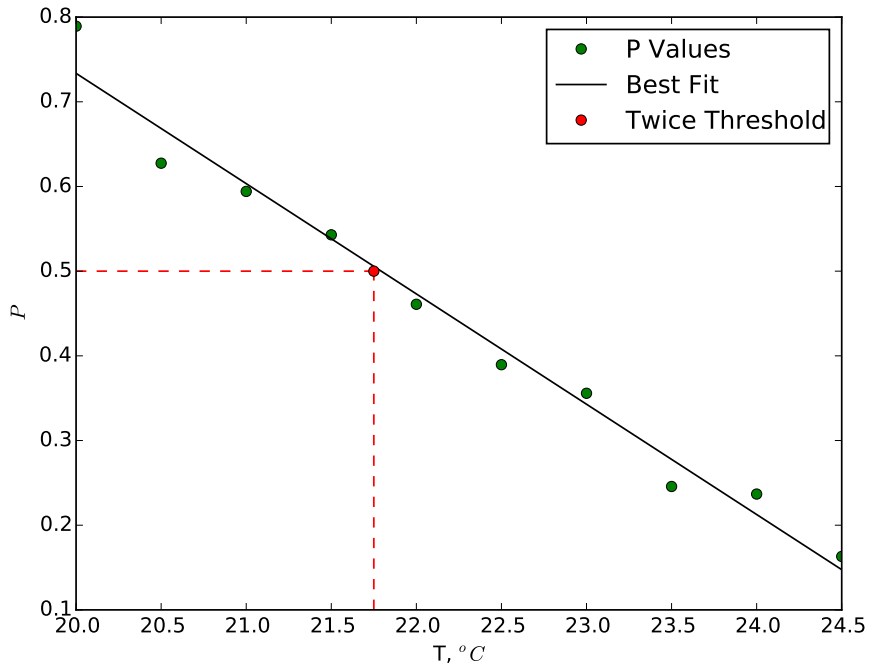


Figure 3.4: Plot of  $P$  versus temperature. The dashed line indicates how the temperature was selected to ensure a  $P$  value of 0.5.

### 3.3.2 Free Space Optics

During the set-up of the experiment, the optimal orientation of the free space optics is found by passing a reference beam through the plane of the slave/filter and connecting the beam received at the filter to the photo-detector.

The fine and coarse controls on the mounts are adjusted so that a maximum power of light is recorded on the photo-detector. Finally the reference beam is sent along the path of the injected light, which intersects the plane of the slave/filter at the beam splitter. Only the fine and coarse controls on the mount for the mount with the reference beam are adjusted (beam-splitter and master/slave are no longer adjusted) until a maximum light power is measured again on the photo-detector. The maximum power obtained was of the order of  $300\mu W$ (this is later seen to be sufficient to achieve locking). The fine-tune controls are not modified during the course of the experiment.

The optical output of the slave laser consisted of two primary modes (in the two-mode laser, only one lasing mode was present in the single-mode laser) and the output is filtered such that the data from one optical mode was recorded at a time.

### 3.3.3 Measuring Detuning

Having set up the experiment as described, a LabView program automates the data collection. The wavelength ranges were determined in advance of the experiment. To begin, a low strength optical injection is injected into the slave laser. This is used as a reference beam, as the low strength injection is detectable as a additional peak in the Fast Fourier Transform (FFT)[17] of the optical time-trace, but is sufficiently small that the underlying laser dynamics are not perturbed by the injection. The Table 3.1 below lists the detuning values.

Table 3.1: Table listing frequency detuning (GHz) and the corresponding wavelengths (nm) of the master laser.

Detuning List	
Freq (GHz)	Wavelength (nm)
-10	1546.542
-8	1546.524
-6	1546.516
-4	1546.497
-2	1546.479
0	1546.470
2	1546.464
4	1546.456
6	1546.448
8	1546.340
10	1546.382

### 3.4 Data Collection and Inspection

Beginning with an modulated optical injection at 1546.542nm, the optical output of the master laser ( $K$ ) is modulated with  $100\text{kHz}$ , and injected into the slave laser. The output of the slave laser is passed through a filter where only the injected mode is allowed through. The injected mode optical data is then recorded on an oscilloscope (via a photo-diode of  $8\text{GHz}$  bandwidth) with a time-step resolution of  $5 \times 10^{-11}\text{s}$ .

The wavelength is stepped through with a step size  $\delta\lambda$  of  $0.001\text{nm}$  and the optical output of the slave laser is recorded again. This process is repeated until the wavelength of the master laser reaches 1546.382nm.

The filter is then adjusted to allow only the uninjected mode of the slave laser through. Then the experiment is repeated, but this time the output from the uninjected mode of the slave laser is recorded.

Once all time-series recording has taken place, the optical output of the slave laser (with no filter) is then connected to a power-spectrum analyser to ensure mode locking is still attained at  $-8\text{GHz}$ . This check is also performed before adjusting the filter.

Having collected the data for the  $K-\Delta\omega$  parameter space, we now proceed to identify the dynamical features of the time traces. In Fig.3.5(a) the recorded  $K^2$  (10% of injection via 90: 10 beam-splitter) is shown above the time-trace recorded at  $+2.7\text{GHz}$  detuning. Depicted here are almost three full periods of  $K$  and a correlation between the injected  $K^2$  and  $|E|^2$  (Fig.3.5(c)) is clearly evident. Some broadening of the sinusoidal wave of  $K^2$  is also evident at the minima and maxima

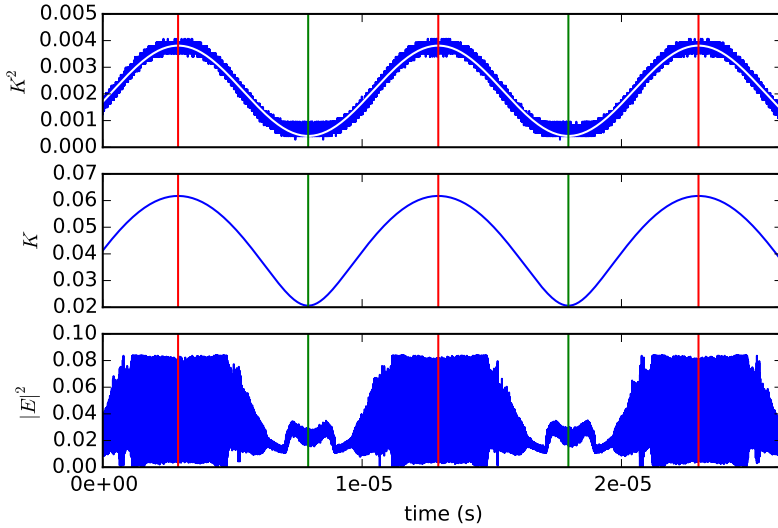


Figure 3.5: **a)** Recorded  $K^2$  (injection strength) with fitted sine curve (white). **b)** Fitted  $K$ . **c)** Sample time-trace at +2.7GHz detuning. The red and green vertical lines indicate the locations of the local maxima and minima of  $K$  respectively.

of  $K^2$ . This is due to setting the amplitude of the sine wave, which is biased at zero. The max/min of the sine wave are hitting the limits of the modulator. Setting the modulator any higher would result in 'inverted' sine waves at the max/min and any lower would lessen the  $K^2$  range explored. This broadening of the injected signal adds partially to an error in fitting a sine function to  $K^2$  and it will be shown soon that this is a very small error.

Having automatically found the turning points in  $K$ , the time-traces split up according to upward and downward sweeps in  $K$ . Fig 3.6 demonstrates the splitting of the time-traces.

In Fig. 3.6(a) and (d) the plateaus at the upper and lower limits of  $K^2$  are clearly evident. Later the plots will be cut to exclude the plateau regions as a constant  $K^2$  will add no new information.

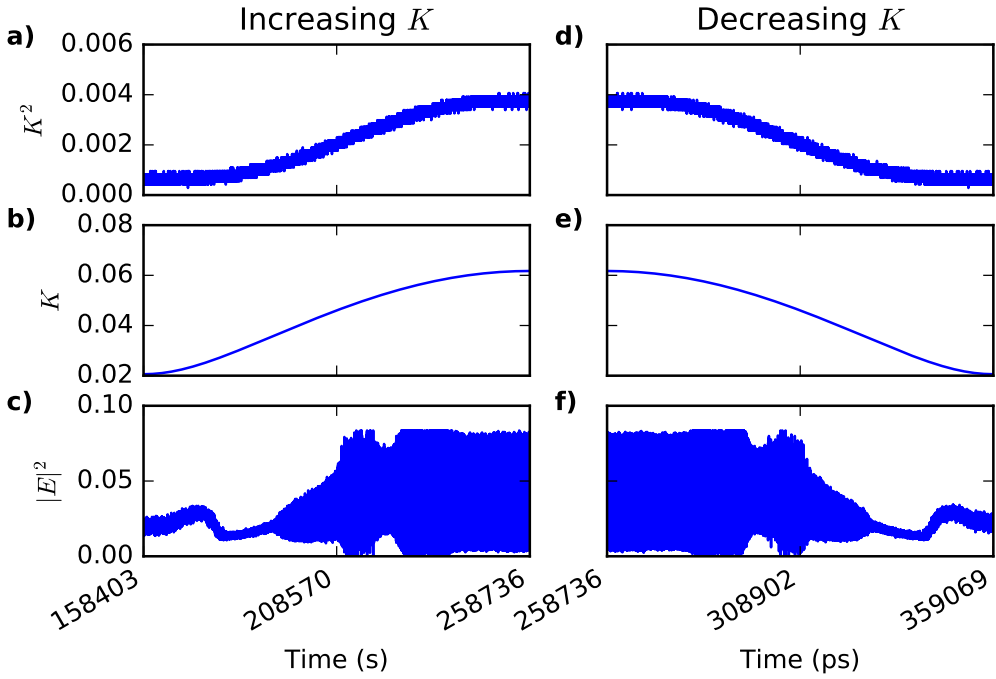


Figure 3.6: **a) - c):** Experimentally recorded  $K^2$ , fitted  $K$  and experimentally recorded  $|E|^2$  for the first upward sweep in  $K^2$ . **d) - f):** Experimentally recorded  $K^2$ , fitted  $K$  and experimentally recorded  $|E|^2$  for the first downward sweep in  $K^2$ .

### 3.4.1 Mean and Standard Deviation Thresholds

From here onwards, optical time-trace will be plotted against  $K$  instead of time, as  $K$  is varied in time and  $E$  changes correspondingly. To begin the dynamical regime identification, the various dynamical properties at each  $K - \Delta\omega$  point need to be identified. The mean and standard deviation of the optical intensities are arguably the most easily obtained quantities, therefore we determine them for the full  $K - \Delta\omega$  plane. The time-trace was split into segments of 500 points ( $2nns$ ) and over this interval  $K$  was assumed to be approximately constant.

This is shown in the top row plots of Fig. 3.7. The top left panel shows that the injected mode is lasing (red) for large regions of the parameter regime, and non-lasing for a blue region between 0 and 6 GHz detuning at low  $K$  values and a second blue region below -5 GHz.

By comparing with the top right hand panel of Fig. 3.7, we observe that the uninjected mode and injected mode appear to have some conservation of total intensity. It can be seen that outside of the TME state, only one of the modes is lasing with a large mean at a time. For example, it is shown that when the uninjected mode is at its lowest intensity (off) the injected mode is at a maximum

value. Conversely, when the uninjected mode has a large average intensity, the injected mode is low (but never off). There also exist regions where both modes lase with intermediate mean values. This alludes to a conservation of total optical output.

In addition we also observe regions where both modes have intermediate intensities (yellow, green and light blue regions), in these regions the sum of the intensities should be approximately equal to the maximum attained when either mode has a low mean intensity. From the plot of the standard deviation of the uninjected mode shown in the bottom right panel of Fig. 3.7 it is evident that the dynamics of the uninjected mode is not constant in these regions of intermediate intensities suggesting complex dynamical Two Mode behaviour. The standard deviation of the injected mode shown in the bottom left hand panel is also large for large  $K$  values, where the uninjected mode is off. In this region we expect complex single mode dynamics. The precise value of the standard deviation will depend on the bandwidth of the oscilloscope, but is not critical for the classification of the dynamical states. We therefore observe that already the average intensities and standard deviations of both modes reveal nontrivial dynamical features which depend on injection strength and detuning.

In Fig 3.7, it is evident that a distinction can be made between  $K - \Delta\omega$  points where the injected and uninjected modes have large or small means and standard deviations. It is generally assumed that the injected mode is always lasing, precisely because it is undergoing continuous injection, but nothing is known about the state of the uninjected mode. Therefore, it would be useful to define a threshold value for the mean and standard deviation of the uninjected mode to quantify if a point in  $K - \Delta\omega$  has single or two-mode dynamics, and also if the injected mode is in a locked or unlocked state.

In Fig. 3.8(a), several time-traces over various detunings are plotted. The threshold value of the mean is set to 0.0048. Fig. 3.8(b) depicts the standard-deviation for the same time-traces with a threshold of 0.0001.

In Fig. 3.9 the thresholds depicted in Fig. 3.8 are applied to the whole  $K - \Delta\omega$  plane and the main structures of the laser dynamics are outlined.

Apart from the intensity average and the standard deviation, another easily accessible quantity is the number of separated peaks in the power spectra of the mode intensities. The power spectra for a number of time traces are shown in the bottom row of Fig. 3.12. At low  $K$  (left hand panel at  $K = 0.027$ ) we see that the laser is unlocked, and the only (relatively weak) peak in the power spectrum is due to the beating between injected light and the free running laser. We use an

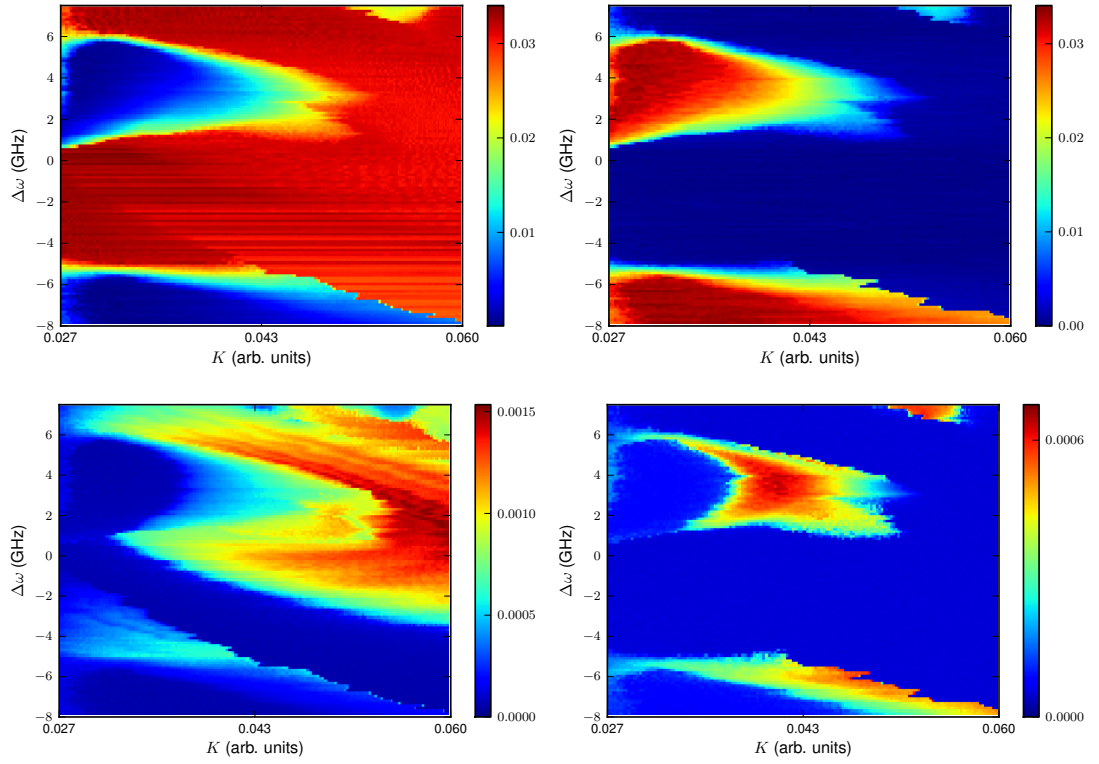


Figure 3.7: Experimentally measured average (top row) and standard deviation (bottom row) of injected (left column) and uninjected (right column) modes in the  $K$ - $\Delta\omega$  plane.

intensity threshold as shown in Fig. 3.12 to distinguish strong peaks from possible noise. The threshold value for counting the peaks was chosen to be significantly higher than the unavoidable noise background and significantly lower than the maximum oscillation amplitude. The chosen threshold value corresponds to 2% of the maximum peak. Therefore transitions from sub-harmonic peaks are captured even if they are considerably weaker than the fundamental peak.

In order to determine the number of frequencies present in the time-trace segment, a Discrete Fourier Transform is performed on the time-trace segment. In Fourier Theory, the transform assumes an infinitely repeating signal, however in the experimentally observed time-trace the injection strength  $K$  is varied in time. Consequently the signal is non-stationary and the discontinuity at the ends of the time-trace contribute non-existent frequencies and noise to the FFT. To overcome this well-known and anticipated problem a smoothing can be applied to the time-trace segment which lessens the discontinuity at the edges of the time-trace segments. The smoothing function applied in this work is the Hamming

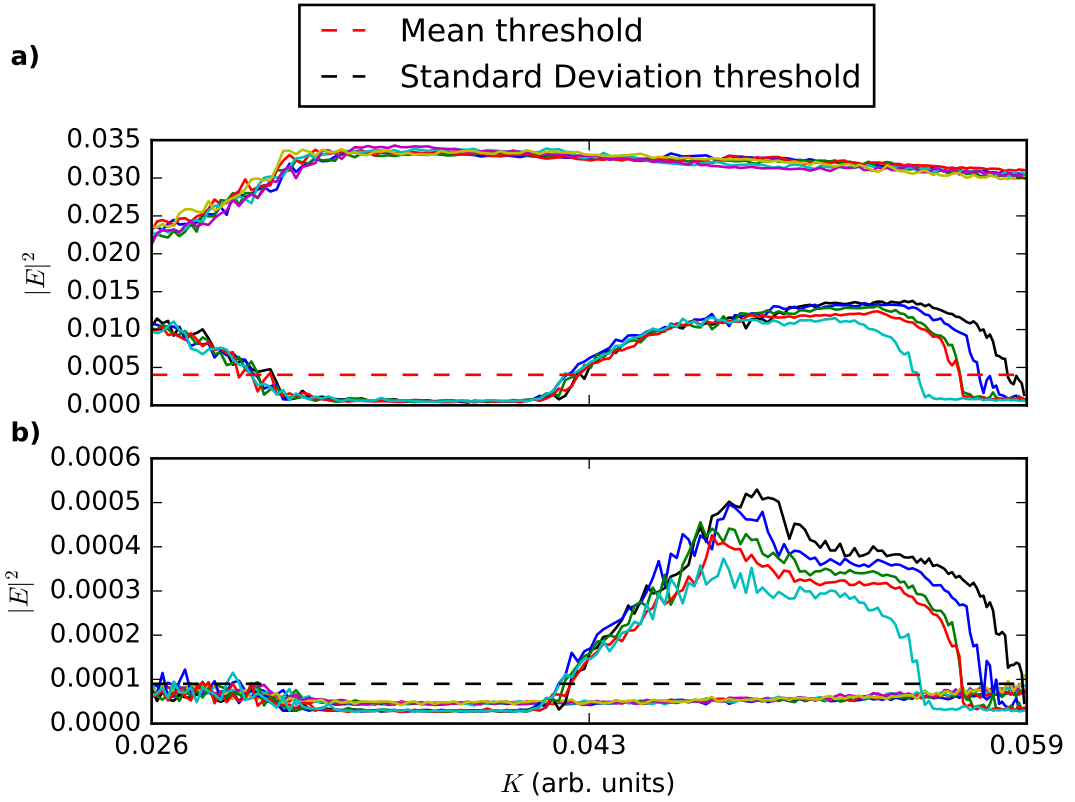


Figure 3.8: **a)** Mean threshold for uninjected mode and **b)** Standard deviation threshold for Injected mode. Time trace from several different  $\Delta\omega$  are plotted as a single threshold is used for the full two-dimensional plane.

Window[7, 5], which is defined as:

$$w(n) = 0.54 - 0.46\cos\left(\frac{2\pi n}{M-1}\right) \quad 0 \leq n \leq M-1. \quad (3.2)$$

where  $M$  is the number of points in a time-trace segment. The Hamming Window is multiplied by the time trace before an FFT is performed. The coefficients chosen decrease the discontinuity between the ends of the time-trace chunk as the FFT requires a periodic function and the discontinuity would appear as noise in the frequency domain.

Fig. 3.10 depicts the Hamming Window and its Fourier Transform. It should be noted that the coefficients dictate the side-lobe compression. These coefficients [35] were chosen such that the maximum size of the side lobe is one-fifth the size lobe of the Hanning Window [19, p.142].

For the time-trace segments, the time-traces were discretised into chunks of 25ns. This resulted in a truncated maximum FFT resolution signal of the order of  $(0.2)GHz$ . As the typical laser dynamics occur on the  $GHz$  scale, no dynamical

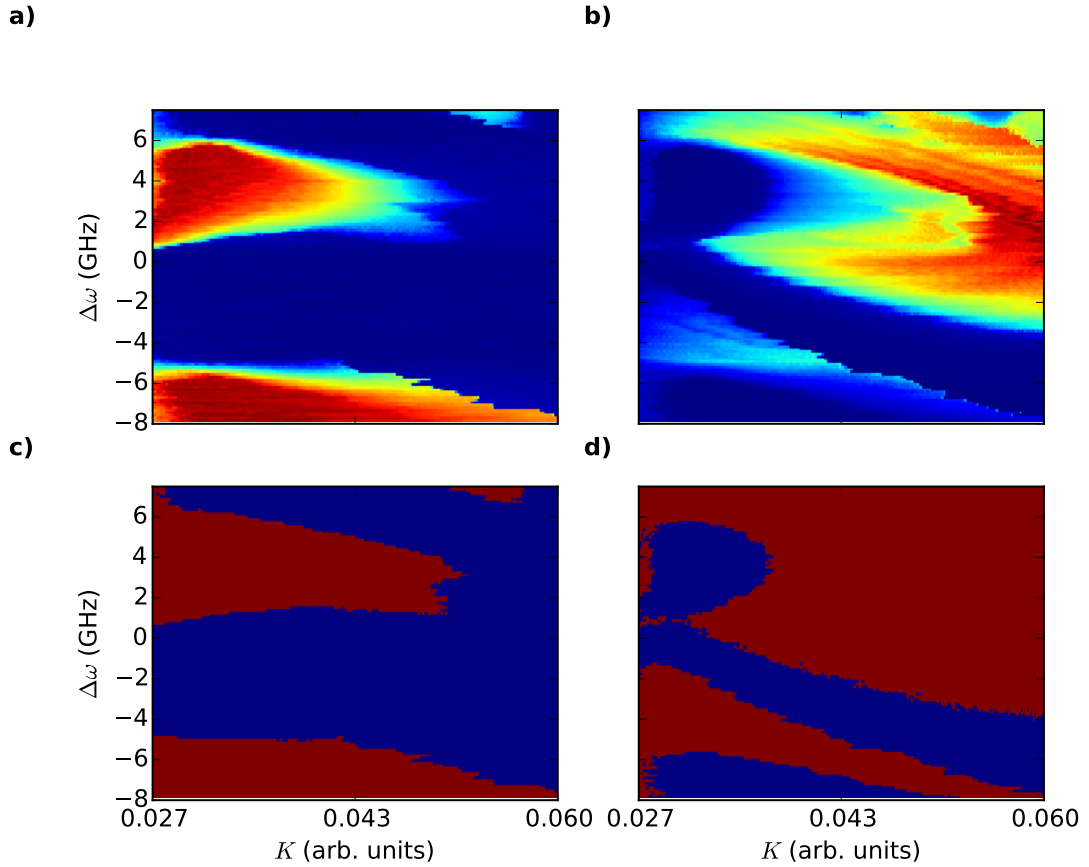


Figure 3.9: (a) Mean of Uninjected Mode and (b) Standard deviation of Injected Mode. (c) Mean threshold and (d) standard deviation threshold as depicted in Fig. 3.8.

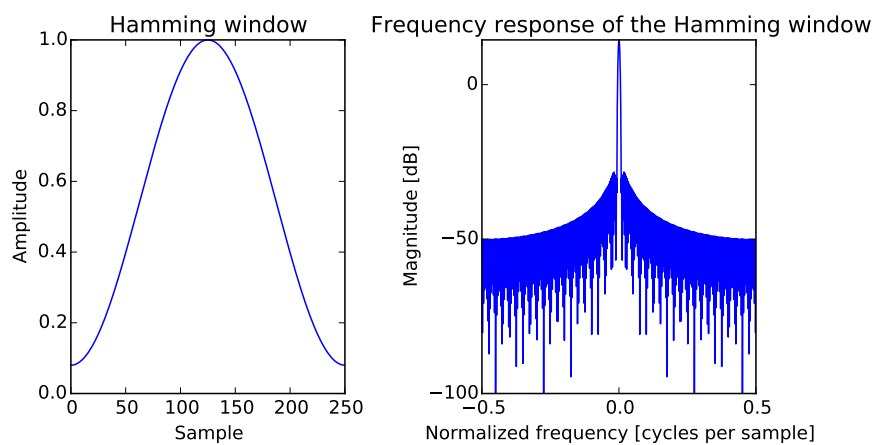


Figure 3.10: a) Hamming Window. b) FFT of Hamming Window.

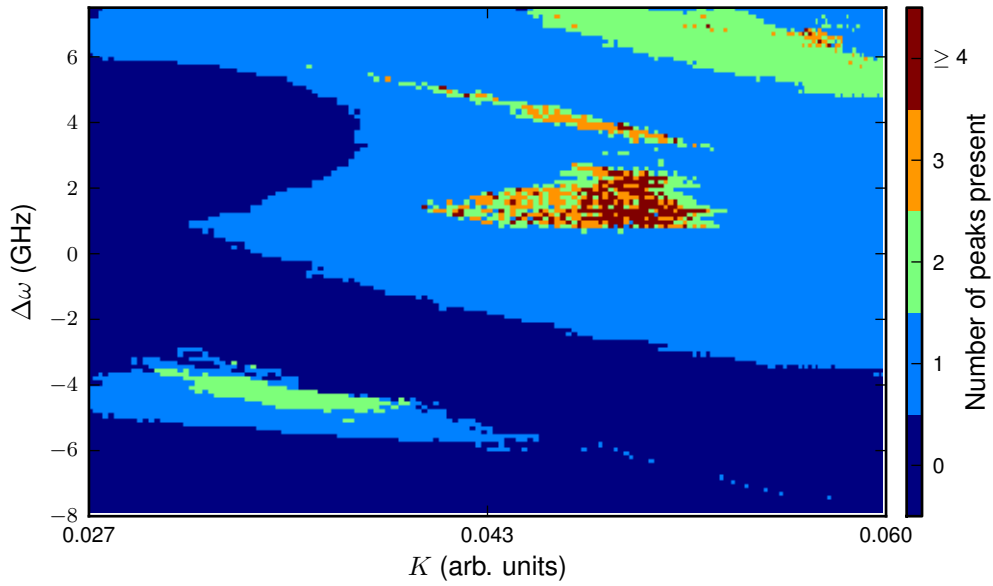


Figure 3.11: Number of peaks present in the FFT of the experimentally obtained time traces as a function of  $K$  and  $\Delta\omega$

phenomena are omitted due to the chunk size selected.

An overview of the number of peaks in the power spectrum of the injected mode at every point is shown in Fig. 3.11. Here the dark blue regions have no peaks above the FFT intensity threshold. Most of these regions correspond to states where the injected mode is locked, except for states with large standard deviations. All other colours correspond to unlocked behaviour. However, only considering the number of peaks present, does not always allow us to distinguish between Single Mode and Two Mode dynamics. For example, the dark blue region around  $(0.027, +4)$  is a locked state, where the uninjected mode is on (Two Mode locked state), while in the band shaped dark blue region around  $(0.043, -2)$  the uninjected mode is off (Single Mode locked state). In order to distinguish between Two Mode and Single Mode dynamics and to identify other dynamical features, we will now introduce a method, which combines the information from Fig. 3.7 and Fig. 3.11.

Having described all of the analytical tools utilised in the analysis, Fig 3.12 is introduced as an example of their combined information. Using the detuning at  $+2.7\text{GHz}$  most of the systems' dynamics can be seen in a single time-trace. At  $K = 0.028$  the injected mode locks and no peak is present in the lower spectrum. At higher  $K = 0.04$  the laser shows undamped relaxation oscillations with a single peak appearing at  $5.9\text{ GHz}$ . For even higher  $K = 0.047$  (right most panel), a number of peaks appear in the power spectrum due to the complex dynamics

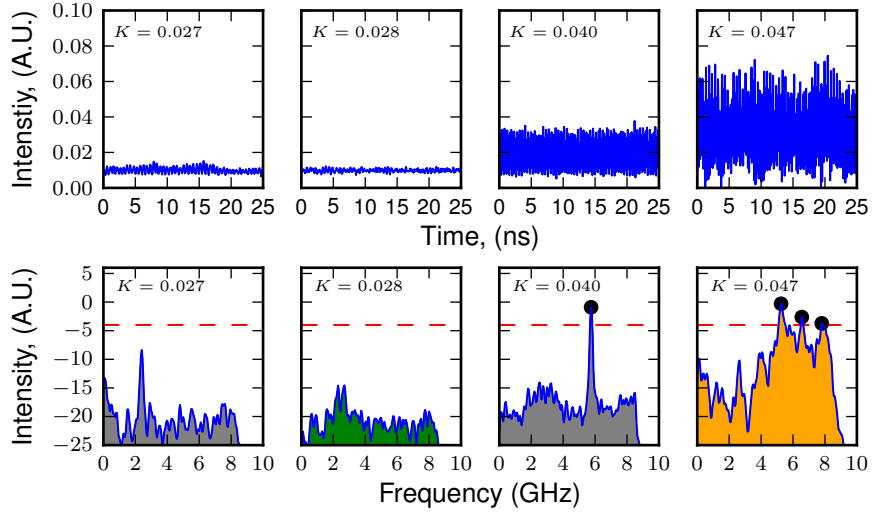


Figure 3.12: Top row: Sample time traces for various values of  $K$  at  $\Delta\omega = +2.7$  GHz. Bottom Row: FFT of time traces in Top Row, with detected peaks indicated by full circles. Colour fill represent the identified state as explained in the main text. The red dashed line indicates the intensity threshold used for peak detection. FFTs are shown on a log scale.

Table 3.2: State colour definitions, based on if the Mean (Mn) or Standard Deviation (SD) is Large (L) or Small (S) and the number of peaks detected in the injected mode.

State	Injected Mode			Uninjected Mode		Colour
	Mn	SD	Peaks	Mn	SD	
TM Locked	L	S	0	L	NA	Light Green
SM Locked	L	S	0	S	NA	Dark Green
TM Unlocked	L	L	$\leq 1$	L	NA	Light Grey
SM Unlocked	L	L	$\leq 1$	S	NA	Dark Grey
TM Complex	L	L	$\geq 2$	L	NA	Light Orange/Red
SM Complex	L	S	$\geq 2$	S	NA	Dark Orange/Red

present in the time trace. In the bottom row of Fig. 3.12 the FFT of each time-trace chunk is colour filled. The colours grey, green and orange are used to indicate unlocked, locked and complex dynamics respectively. In the next section this colour pattern scheme will be applied to a full time-trace, and then to the entire  $K - \Delta\omega$  plane and a shading will be introduced to distinguish two-mode and single-mode dynamics.

For completeness, Table. 3.2 contains the colours used for each type of state identified.

### 3.5 State Identification

First we demonstrate our method for determining the dynamical states of the laser for the case of  $\Delta\omega = +2.7\text{GHz}$ . In the middle and lower panel of Fig. 3.13 the time traces of the injected and uninjected modes are shown during one upward sweep of  $K$  and the top panel shows a power spectrum density plot. For low  $K = 0.027$  we observe a low intensity peak in the FFT, which is below our cut-off point for peak intensity. However, the standard deviation of the injected mode is non-zero as indicated by a non-zero standard deviation at  $K = 0.027$ . For this Two Mode unlocked state we adopt a light-grey colour as shown in the background of FFTs in Fig. 3.12 and the middle and lower panels of Fig. 3.13. For  $K$  between 0.028 and 0.036 the standard deviation in the injected mode decreases, but both modes remain on. This is a Two Mode locked state which we indicate with a light green colour. Then for  $K > 0.036$  the state unlocks and the relaxation oscillation frequency appears in the power spectrum. This unlocked state is again indicated by a light grey colour. For higher  $K$  values between 0.046 and 0.049 additional peaks are picked up in the power spectrum, and we denote them with orange and red colours. At  $K = 0.047$ , both modes are on with a significant standard deviation and there are three peaks in the power spectrum (see the lower right hand panel in Fig. 3.12). We identify this as a Two Mode chaotic state, and denote this point by a light orange colour. In the following, points with more than one peak in the power spectrum are coloured from yellow to red, for small and large standard deviation, respectively. This yields a useful indicator of chaotic behaviour. At even higher  $K > 0.05$  the uninjected mode vanishes and we enter a regime of Single Mode dynamics, which is indicated by a dark shading.

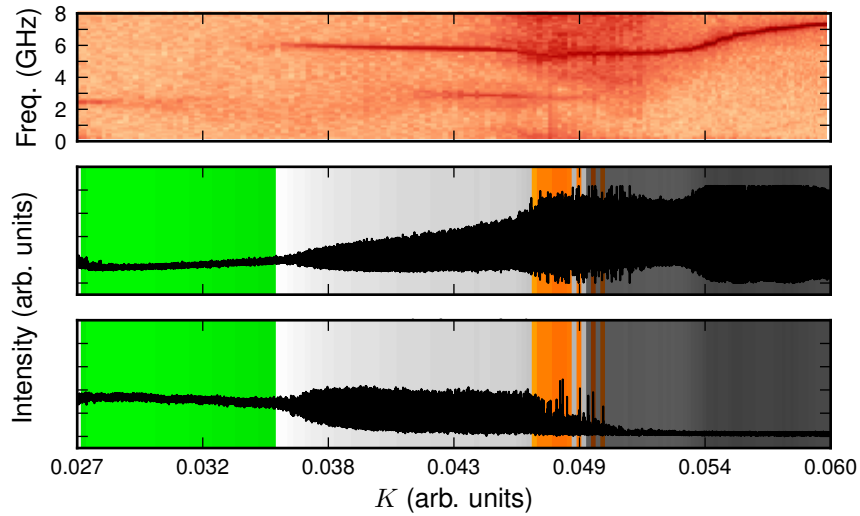


Figure 3.13: Experimentally recorded dynamics at fixed detuning  $\Delta\omega = +2.7$  GHz and varying  $K$ . Top panel: Power spectrum of injected mode. Middle panel: Time trace for injected mode. Bottom panel: Time trace of uninjected mode. The coloured backgrounds in the middle and bottom panels represent the identified state.

## 3.6 Experimental Stability Diagram

Applying the technique demonstrated in Fig. 3.13 for all  $\Delta\omega$  allows us to build a  $K$ - $\Delta\omega$  stability diagram which identifies the dynamical state of the two colour laser at given parameter values. The result is presented in the top left panel of Fig. 3.14. We observe two regions of Two Mode locked states (light green), one at positive detuning ( $\Delta\omega$  between 0 and 6 GHz) and one at negative detuning ( $\Delta\omega < -6$  GHz). This latter region of Two Mode locked states was partly identified previously in [65]. Both Two Mode locked states are bounded by regions of Two Mode dynamical states (light grey). The top Two Mode dynamical region shows a distinctive triangular shape. Two bubbles of Two Mode complex behaviour (light orange/ light red) extend at two of the sides of this triangle. At larger  $K$  values the dynamics becomes single mode (dark shading), including a prominent bubble of complex behaviour (dark orange and red) at the centre of the stability diagram. In the top right corner a further bubble of complex Single Mode dynamics (dark red) exists. We observe a large dark green band of Single Mode locked states below 1 GHz and a large dark grey region of single mode unlocked states and there is a further region of Single Mode complex dynamics around  $\Delta\omega = -4$  GHz below the band of Single Mode locked states.

After generating the experimental stability diagram for a Two Mode laser at  $P = 0.5$ , our aim is now to put this result in a broader context, firstly by compar-

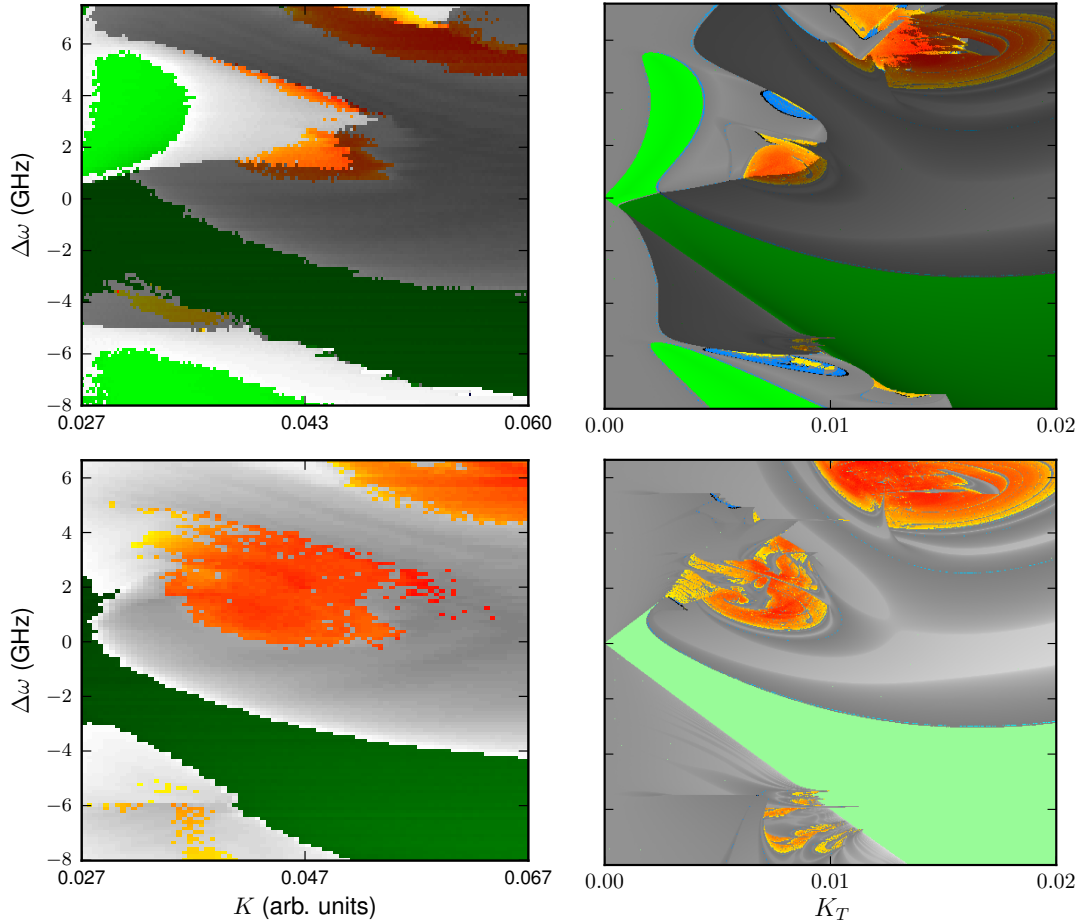


Figure 3.14: Left panels: experimental stability diagrams for the Two Mode laser at  $P=0.5$  (upper) and the Single Mode laser at  $P=0.5$  (lower). Right panels: corresponding theoretical stability diagrams based on numerical time-traces and Lyapunov exponents. Light (dark) colours indicate Two Mode (Single Mode) dynamics. Stable Fixed point (FP) states are green, stable limit cycles (LC) are grey, stable tori (TR) are blue and chaotic (CH) states are yellow and red.

ing with a theoretical model and secondly by comparing different experimental configurations. For the theoretical comparison we explore the use of Lyapunov Exponents in Sec 3.7.

### 3.7 Lyapunov Exponents

The following dimensionless model for Two Mode lasers is used to model the amplitude of the uninjected mode  $|E_1|$ , the complex slowly varying field for the

injected mode  $E_2$  and the population inversion  $n$  [65]:

$$|\dot{E}_1| = \frac{1}{2}(g_1(2n+1) - 1)|E_1| \quad (3.3)$$

$$\dot{E}_2 = \left[ \frac{1}{2}(1+i\alpha)(g_2(2n+1) - 1) - i\Delta\omega \right] E_2 + K_T \quad (3.4)$$

$$T\dot{n} = P - n - (1+2n)(g_1|E_1|^2 + g_2|E_2|^2) \quad (3.5)$$

where the nonlinear modal gain is  $g_{1/2} = \left[ 1 + \epsilon \left( |E_{1/2}|^2 + \beta |E_{2/1}|^2 \right) \right]^{-1}$ . The parameters for the numerical simulations are  $\alpha = 2.6$ ,  $P = 0.5$ ,  $T = 800$ ,  $\beta = 2/3$ , and  $\epsilon = 0.01$ . This model is also identical to the system of ODE's motivated in Sec. 2.2.3. The experimental parameters have been established by previous work in the Tyndall National Institute [65, 64]. The bifurcation parameters are the injection strength  $K_T$  and the frequency detuning  $\Delta\omega$ . As previously mentioned, the parameter  $K_T$  in (3.4) and the experimental injection strength of the master laser  $K$  cannot be quantitatively compared, because the experimental coupling efficiency is not known. Integrating this model numerically and calculating the Lyapunov exponents (LEs) [99] allows us to distinguish between fixed points (all LEs less than zero), limit cycles (one LE equals zero), tori (two LEs equal to zero) and chaotic states (one or more LE positive).

Fig. 3.15 contains a graphical representation of the concept of a Lyapunov calculation. The point  $d_0$  is the unperturbed state that is integrated forward in time to  $d_0(t)$ . In the model employed here, there are three dimensions in which the point  $d_0$  can be perturbed. This perturbation in three-dimensions forms the sphere in Fig. 3.15 centred at  $d_0$ . This sphere is then evolved forward in time to a more complex ellipse-like structure. The rates of compressing/stretching of the radii correspond to the Lyapunov exponents at that point. Mathematically, they are defined as:

$$\lambda = \text{Limit}_{t \rightarrow \infty} \frac{1}{t} \ln \frac{|\delta d_0(t)|}{|\delta d_0|} \quad (3.6)$$

where  $t$  is the time integrated forward, and  $\delta$  represents the change in  $d_0$  and  $d_0(t)$  due to a perturbation.

The theoretical stability diagram is shown in the upper right panel of Fig. 3.14. We find that this diagram mirrors astonishingly well the overall shape and location of both regions of Two Mode locked states (light green) identified in the experimental diagram shown in the top left panel of Fig. 3.14. In addition, the band of Single Mode locked states (dark green) agrees with the theoretically ob-

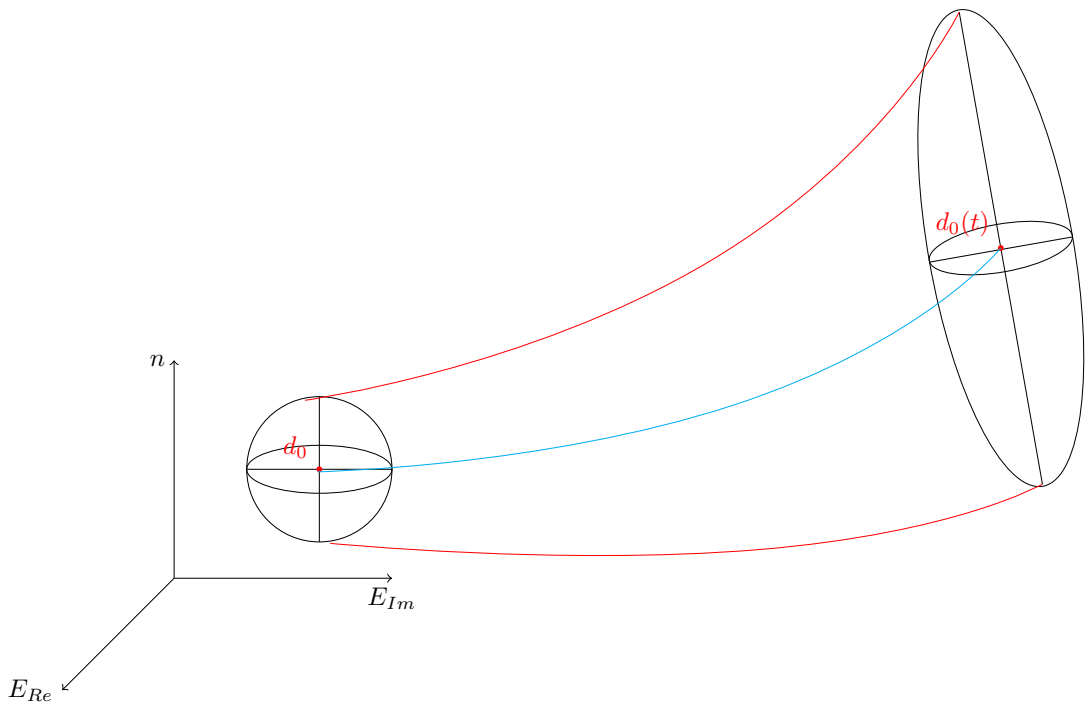


Figure 3.15: Lyapunov Exponent diagram: An initial point  $d_0$  is integrated forward to  $d_0(t)$ . The initial point is perturbed by a small influence and ends up on black sphere. The sphere is integrated forward in time and maps onto the ellipse. The rates of stretching/compressing of the radii of the sphere/ellipse are the Lyapunov Exponents of the  $E_{Re}, E_{Im}$  and  $n$  dimensions respectively. If any of the Lyapunov Exponents are positive, the system is said to be chaotic as two trajectories, initially close, will diverge in finite time.

tained Single Mode fixed points at negative detuning. The top row of Fig. 3.14 also shows that the regions of Two Mode (light grey) and Single Mode (dark grey) dynamics in the left upper panel are consistent with the stable limit cycles found theoretically in the upper right panel. The remaining dynamics in the theoretical model are the tori and chaotic states, which are identified with a blue and yellow/red colouration, respectively. Experimentally we did not attempt to distinguish between tori and chaotic behaviour, however, the complex dynamical regions in the upper left panel of Fig. 3.14 correspond strongly with the collective tori and chaotic regions in the central lower panel of Fig. 3.14. Unavoidably, we experimentally slightly overestimate the band of Single Mode locked states at low  $K$ . This is explained by the experimental difficulty of distinguishing between Single Mode locked and Single Mode unlocked states. This issue does not arise for Two Mode states, as our state identification routine can use the behaviour of the uninjected mode as a reference point.

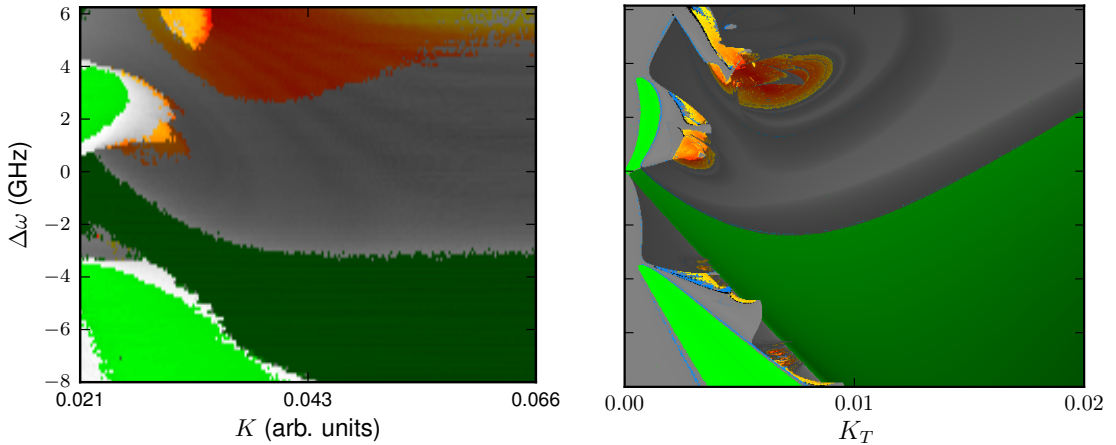


Figure 3.16: Left panel: Experimental stability diagram for the Two Mode laser at  $P = 0.2$ . Lower panel: Theoretical stability diagram for the Two Mode laser at  $P = 0.2$ . Locked, unlocked and complex dynamical states are identified using the same colour scheme as the Two Mode and Single Mode  $P = 0.5$  configurations.

### 3.8 Single Mode Stability Analysis

Having established qualitative agreement for the Two Mode laser at  $P = 0.5$ , we now examine the Single Mode laser at  $P = 0.5$  shown in the lower left and right hand columns of Fig. 3.14. By its nature, there are no Two Mode states present in the Single Mode laser and we now distinguish between locked (green), unlocked (grey) and complex (red/yellow) states. In the experimental stability diagram we observe a band of locked states and two prominent bubbles of complex dynamics. These features are in agreement with the corresponding theoretical stability diagram in the lower right panel. Again a slight overestimation of the band of locked states occurs at low  $K$ . One of the more striking results of the Two Mode/Single Mode laser comparison is the persistence of states identified as Single Mode states in the Two Mode laser, that remain Single Mode states in the Single Mode device. For example, all states in the Single Mode band of locked states in the Two Mode laser are still locked states in the Single Mode laser. However, states which are Two Mode in the Two Mode laser in general change their character in the Single Mode laser, for example a region of Two Mode unlocked states near the centre of the top central panel becomes part of the complex bubble in the top left panel. This behaviour is reproduced theoretically in the lower right panel, and is due to the presence of the invariant manifold  $|E_1| = 0$  in the system of equations (3.3)-(3.5).

## 3.9 Lower $P$

The final configuration explored via our technique is the Two Mode laser at a lower pump parameter  $P = 0.2$ . The respective experimental and theoretical stability diagrams are shown in the left and right hand panels of Fig. 3.16. Experimentally, we observe that all dynamical regions identified for  $P = 0.5$  are still present at  $P = 0.2$ , however, the boundaries shrink to smaller  $K$  and  $\Delta\omega$  values. For example, the upper bound of the Two Mode locked state at positive detuning has decreased from 6 GHz to 4 GHz. In addition the distance between the Two Mode and Single Mode locked states at negative detuning becomes smaller and almost closes at  $\Delta\omega \approx -6$  GHz. These experimental trends are in striking agreement with the theoretical results shown in the lower right panel of Fig. 3.14, where the same dramatic shrinking of the domain boundaries to smaller values of  $K_T$  and  $\Delta\omega$  is observed.

## 3.10 Optical Bi-stability

The results thus far have been utilised in characterising an optically injected laser, however uses of optically injected lasers have not yet been fully explored. In today's technology-centred world, all optical signal processing is a strong competitor to meet the bandwidth demands in telecommunication. Novel approaches are sought to implement many electrical circuit elements optically such as switching[52], logic gates[73] and RAM[23] (random access memory). It has already been shown[49, 41] that a master-slave configuration, similar to the one utilised here, can achieve optical bi-stability.

Having thoroughly developed a characterisation method for dynamical state identification in an optically injected laser, the next logical step is utilise the information available to demonstrate the automatic detection of an optical bi-stability in an optically injected laser. As  $K$  is varied sinusoidally, the laser will visit all  $K - \Delta\omega$  combinations as  $K$  both increases and decreases. Therefore, a bi-stability in the mean of the injected mode should be observed in comparing Figs. 3.6(a)-(c) with the previously unused down sweeps (downsweep of  $K$ ) time-traces from Figs. 3.6(d)-(f).

Previously, the estimate of the turning points of  $K$  in Fig. 3.6 were sufficient for dynamical region mapping. However, a different type of accuracy is required for the detection of an optical bi-stability.

Therefore an investigation into the accuracy of the fit is now required as we now compare the upward and downward sweeps of  $K$ . This is shown in Fig 3.17.

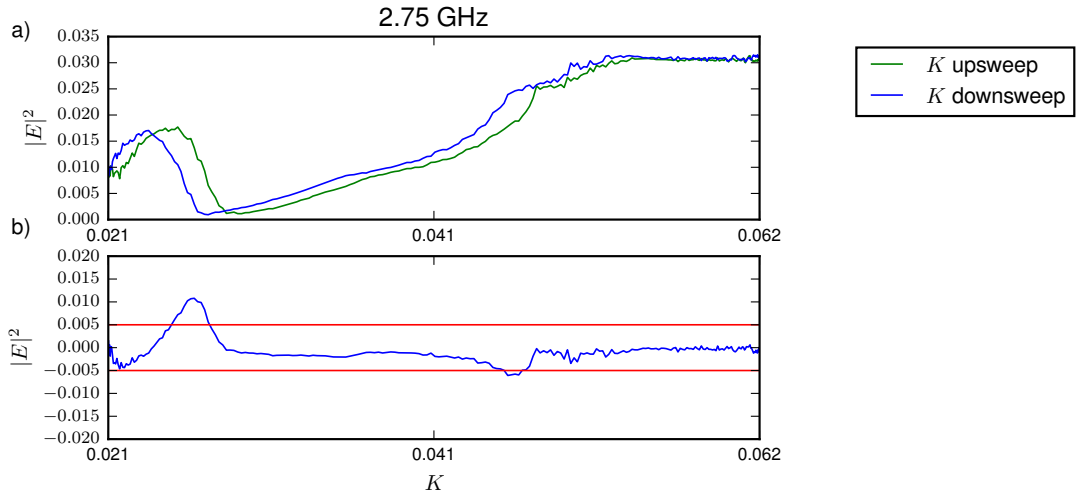


Figure 3.17: **a)**: Plot of the mean of  $|E|^2$  as  $K$  is increasing (blue) and decreasing (green).**b)**: Plot of the difference (subtracted) between the upward and downward means.

An explanation of the terminology used to describe the bi-stability detection is included here: All choices of bi-stability are made assuming that  $K$  begins at zero and increases first. Therefore, the green time-trace in Fig. 3.17 is the first half of the full  $K$  sweep and the blue is the second half (referred to as  $K$  upsweep and  $K$  downsweep respectively). Furthermore, the test for the existence of a bi-stability will the subtraction of the latter from the former. The instances where (if any) points on the downsweep of  $K$  the mean is larger, the bi-stability will be labelled “ $K$  switches down”, acknowledging that the mean is larger at this  $K - \Delta\omega$  point while  $K$  is decreasing. The reverse situation ( $K$  upsweep is larger) is referred to as “ $K$  switches up”.

Fig 3.17(a) shows that a misalignment exists with the estimation of the turning points of  $K$  in the previous section. The error in detecting the exact turning points of  $K$  is small, but important. The error is estimated to be approximately 2.4% over the full  $K$  period. For the automatic detection of optical bi-stability, the two time-trace segment must align and their differences must equal 0 in the absence of a bi-stability.

Fig 3.17(b) (that difference of two means plotted in (a) )demonstrates that a deviation from 0 is present despite no bi-stability exists. This is due to both time-traces tending to 0 near  $K = 0.027$  and due to the misalignment becoming significant near  $K = 0.05$ . The red horizontal lines indicate  $y$  thresholds of  $-0.01$  and  $0.01$  (a tolerable deviation from 0 for indicating bi-stability.)

To correct alignment issue, the trace for the downward sweep of  $|E|^2$  is shifted along  $K$  by 6 points (in the segmented view, a 2.4% error in the of the total

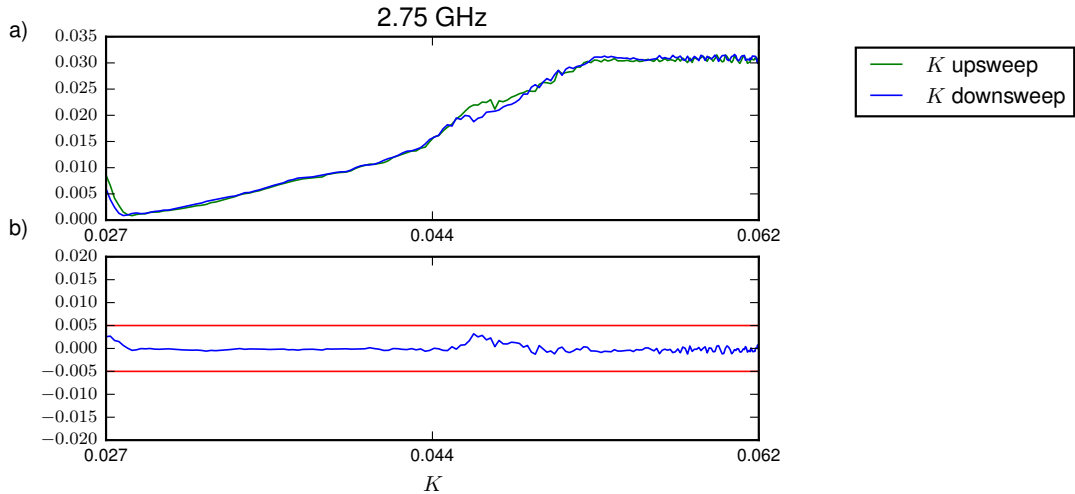


Figure 3.18: **a)** Corrected  $K$  fit for  $+2.75\text{GHz}$  detuning showing a much improved overlap.**b)** Plot of the difference (subtracted) between the upward and downward means showing no bi-stability at this  $\Delta\omega$ .

recorded  $K^2$ ). This shift size was selected as it was small ( 6 of 250 points) and is an acceptable error given only a minimal effort was made in locating the turning points of  $K$ . Once the shift was made, the mis-alignment near  $K = 0.05$  disappeared as the temporal profiles over lapped sufficiently.

Also the time-trace segments are truncated at  $K = 0.027$  and  $K = 0.060$  as  $K^2$  is non-varying beyond those limits. The results of this shift are seen in Fig 3.18 and Fig 3.19, where two different frequency detunings are selected to test if only correct bi-stabilities are detected. This method is now applied to full  $K$ - $\Delta\omega$  plane as shown in Fig. 3.20.

Fig 3.20 shows that when  $K$  is varying sinusoidally, the injected mode switches on from a previously off-state on the downward sweep of  $K$ . This is indicated as the large blue region in Fig 3.20. However, as this is a closed system under optical injection, the total power output of the laser must remain constant and a corresponding change must be seen elsewhere. Therefore, an analysis of the uninjected mode is required. Fig 3.21 combines the results of a bi-stability examination of the injected and uninjected modes as  $K$  is varied sinusoidally. The left column of Fig 3.21 have already been discussed, however when presented here, the bi-stability is easily confirmed visually in the injected mode. Now in the right-hand column, the results of the uninjected mode are presented in an identical fashion, but the results display the opposite transition has occurred. The results show that when  $K$  switches down (from a higher  $K$ ), the uninjected mode goes from an on state to an off state. In the grid view, it is easy to see that the bi-stability

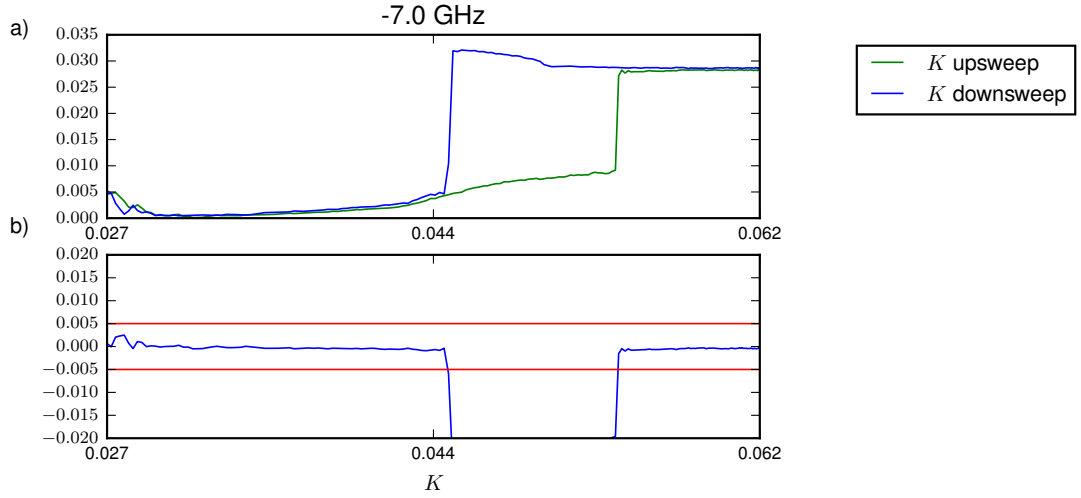


Figure 3.19: **a)** Corrected  $K$  fit for  $-7\text{GHz}$  detuning showing a much improved overlap.**b)** Shows a correctly identified bi-stability using the difference of the corrected means.

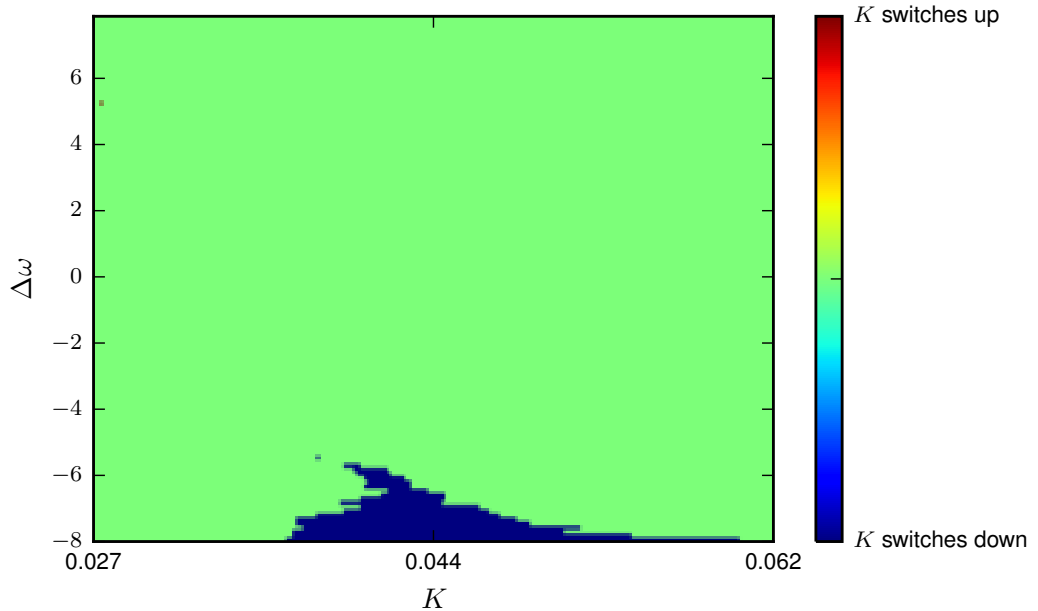


Figure 3.20: A large bi-stability region is detected for negative detuning. This bistability occurs in the injected mode.

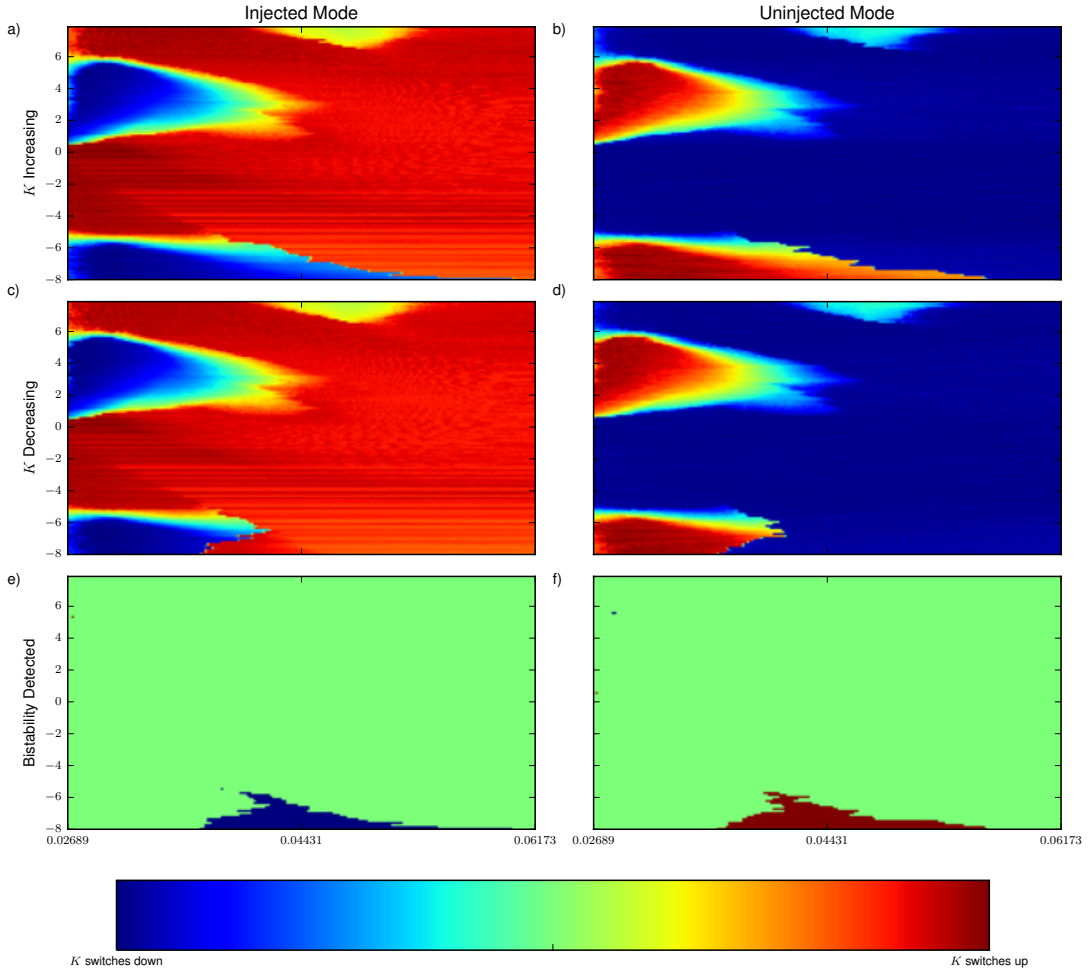


Figure 3.21: Combination of results of the bi-stability analysis for both the injected (left column) and uninjected mode (right column), as  $K$  is swept upwards (top row) and downwards (middle row). The bi-stabilities detected are shown in the bottom row.

area in both modes is identical in shape, size and location. This means that this bi-stability is a region where two modes can be configured to be in either an off or on state by means of optical injection manipulation and therefore this device can be used to provide an optical memory element. This particular bi-stability region has been detected before [36] but using the experimental method outlined in this thesis, the full bi-stability region has been traced out with little effort.

The final step is to confirm bi-stability numerically. This is shown in Fig 3.22. This figure contains the numerical integration of Eqns 2.98 - 2.100 with the addition of a small noise term. The small noise is added to ensure that the bi-stability occurs correctly and the system does not stay trapped on the single mode manifold (see App. A.1 for a demonstration that without noise the uninjected mode can remain in an unstable off state).

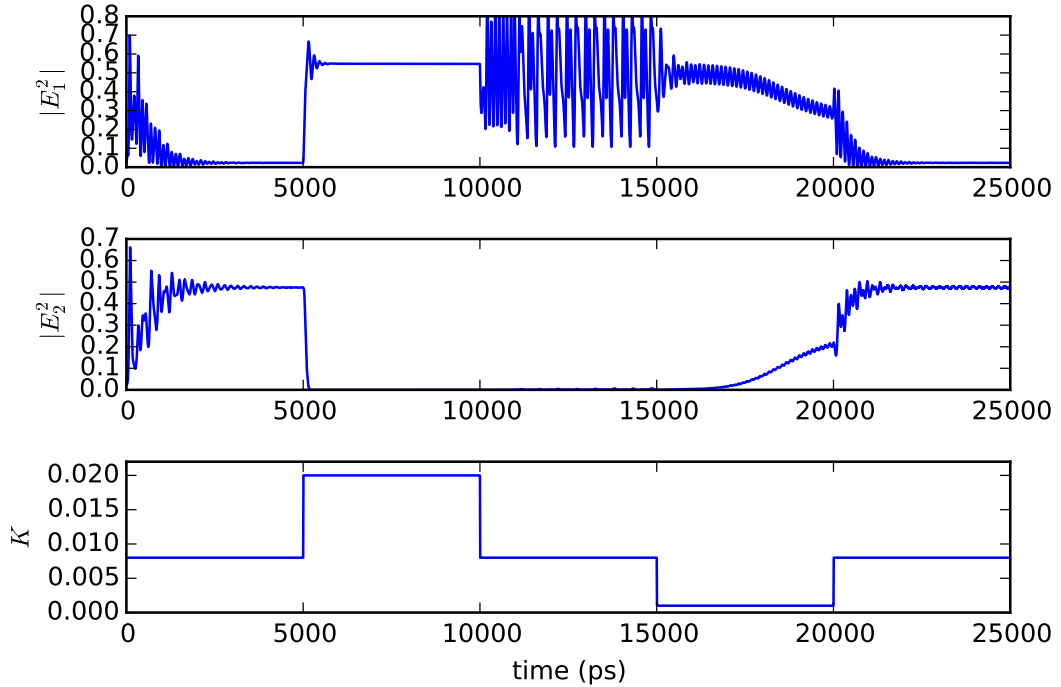


Figure 3.22: Numerical simulation of Bi-stability

### 3.11 Conclusion

In conclusion we have experimentally obtained a two-dimensional stability diagram of an optically injected Two Mode laser for varying injection strengths and detunings. Our method is based on a fast modulation of the injection strength and an analysis of the resulting time traces of the individual modes. The experimental stability diagram agrees quite well with the theoretical model, and thereby confirms the existence, shape and location of many dynamical phenomena. Locked and unlocked states, and complex behaviour have been clearly identified.

The agreement between theory and experiment is mirrored in our results for the Single Mode laser. This validates our technique as device independent and opens new opportunities for other optically injected dynamical systems. Furthermore, this agreement is continued as  $P$  is varied, demonstrating that the dynamical regions are robust areas of dynamics.

In addition to the previously published results, the method has been extended to bi-stability detection and automatically detected the previously known bi-stability region, confirming its novelty and impact. This addition means that a complete dynamical classification routine now exists and can characterise the dynamics of an optically injected laser entirely after simple yet fruitful experiment.

# Chapter 4

## Origins of abnormally large 'Rogue Waves' in optically injected lasers.

### 4.1 Background

With the previous thorough studies of single-mode, optically injected lasers, one could easily conclude that the single mode laser is well understood, with few surprises remaining. However, recently [8, 101] rare, large amplitude excursions have been discovered in semiconductor lasers which have yet to be satisfactorily explained. In [8, 72] it has been shown that the large amplitude events are predicted by the rate equation model and also have been experimentally observed. This confirms their existence as a feature of semiconductor device and not an anomalous aberration from faulty lasers or numerical precision errors.

The title of 'Rogue Wave' (abbreviated from here on-wards as RW) originated initially from the oceanographic problem of rare, large amplitude waves that "appear from nowhere and disappear without a trace" [3] and is currently a popular topic in the study of dynamical phenomena [74]. Additionally, rogue waves have also been identified in capillary waves [78], super-fluid helium [27], atmosphere [28] or microwaves [37]. Their existence in multiple disciplines only further fuels their interest. The semi-conductor laser is an excellent research tool to investigate these phenomena as it is already known to provide an accessible window into a dynamical system. In Sec 4.2 I will compare the previously used model for rogue wave study with the singe mode model outlined in Eqns. (2.101, 2.102).

## 4.2 Model Comparison

Optically injected semi-conductor lasers have been of considerable interest since their invention, as they allow the investigation of complex non-linear dynamical problems in a controllable system isolated from vibration and thermal variation and noise [8]. However, the rate-equation models previously used in [8] (Eqns. (4.1, 4.2)) to numerically reproduce the rare, random, large excursions are derived to model an optically injected laser subject to noise (characterised by the noise strength  $\sqrt{D}$ ) as-well as being presented in a dissimilar form to Eqns. (2.101, 2.102). The first task is to-rewrite Eqns. (4.1, 4.2) and compare them to Eqns. (2.101, 2.102). Following this model comparison, a thorough comparison of previous work into Optical RW events can be made.

$$\frac{d}{dt}E = \kappa(1+i\alpha)(N-1)E + i\Delta\omega E + \sqrt{P_{Inj}} + \sqrt{D}\xi(t) \quad (4.1)$$

$$\frac{d}{dt}N = \gamma_n(\mu - N - N|E|^2) \quad (4.2)$$

Where  $E, N, \alpha, \Delta\omega$  and  $t$  take the same meanings as previously used up to constant proportionality factors which are derived in the next section.  $\sqrt{P_{Inj}}$  is the strength of the injected light.  $\kappa, \gamma_n$  and  $\mu$  are the field decay rate, carrier decay rate and the injection current respectively.  $\xi$  is a complex Gaussian white noise function.

### 4.2.1 Dimensionless model

Using (4.1) and (4.2), let us first re-scale  $N$  using  $\hat{N} = \frac{N-1}{2}$  which gives

$$\frac{d}{dt}E = 2\kappa(1+i\alpha)\hat{N}E + i\Delta\omega E + \sqrt{P_{Inj}} + \sqrt{D}\xi(t) \quad (4.3)$$

$$2\gamma_n^{-1}\frac{d}{dt}\hat{N} = \mu - 1 - 2\hat{N} - (2\hat{N} + 1)|E|^2 \quad (4.4)$$

and both sides are divided by  $\gamma_n$ . Next a re-scaling of  $t$  is introduced as  $\hat{t} = 2\kappa t$  for the dimensionless time. Note that

$$\langle \xi(t)\xi(t') \rangle = \delta(t-t') \quad (4.5)$$

$$\langle \hat{\xi}(\hat{t})\hat{\xi}(\hat{t}') \rangle = \delta(\hat{t}-\hat{t}') \quad (4.6)$$

$$\int_{t_1}^{t_2} \delta(t-t')dt = 1 = 2\kappa \int_{\hat{t}_1}^{\hat{t}_2} \delta(\hat{t}-\hat{t}')d\hat{t} \quad (4.7)$$

Therefore

$$\hat{\xi}(\hat{t}) = \frac{1}{\sqrt{2\kappa}}\xi(t) \quad (4.8)$$

This results in

$$\frac{d}{dt}\hat{E} = (1 + i\alpha)\hat{N}\hat{E} + \frac{1}{2\kappa}\left[i\Delta\omega E + \sqrt{P_{Inj}} + \sqrt{2\kappa D}\hat{\xi}(\hat{t})\right] \quad (4.9)$$

$$2\gamma_n^{-1}2\kappa\frac{d}{dt}\hat{N} = \mu - 1 - 2\hat{N} - (2\hat{N} + 1)|E|^2 \quad (4.10)$$

Furthermore define  $\hat{E} = \frac{E}{\sqrt{2}}$ ,  $\Delta\hat{\omega} = -\frac{\Delta\omega}{2\kappa}$  (Note that the sign of  $\Delta\hat{\omega}$  changes) and  $\hat{D} = \frac{D}{4\kappa}$  to yield

$$\frac{d}{dt}\hat{E} = (1 + i\alpha)\hat{N}\hat{E} - i\Delta\hat{\omega}\hat{E} + \frac{1}{2\kappa\sqrt{2}}\sqrt{P_{Inj}} + \sqrt{\hat{D}}\hat{\xi}(\hat{t}) \quad (4.11)$$

$$\gamma_n^{-1}2\kappa\frac{d}{dt}\hat{N} = \frac{\mu - 1}{2} - \hat{N} - (2\hat{N} + 1)|\hat{E}|^2 \quad (4.12)$$

Finally introduce  $\frac{1}{2\kappa\sqrt{2}}\sqrt{P_{Inj}} = K = 0.00913$ ,  $\frac{\mu - 1}{2} = P$ ,  $\gamma_n^{-1}2\kappa = T = 600$ . The “ $\hat{}$ ” notation is dropped for simplicity and the system reduces to:

$$\frac{d}{dt}E = (1 + i\alpha)NE - i\Delta\omega E + K + \sqrt{D}\xi(t) \quad (4.13)$$

$$T\frac{d}{dt}N = P - N - (2N + 1)|E|^2 \quad (4.14)$$

which is the simplified single mode model in the case of linear gain ( $\epsilon = 0$ ) and the absence of noise ( $D = 0$ ). Having successfully re-normalised Eqns. (4.1, 4.2) into (2.101, 2.102), it has been verified that all dynamical structures measured in [8] are contained in the model derived in this thesis, and by extension, exist in the semiconductor lasers studied in this thesis.

Having compared the two rate equation models and confirmed their similarity it is now necessary to investigate time-series for the presence of RW events. This search will be conducted in the next section and all numerical simulations were begun with the same arbitrary point in the  $E - N$  field, namely:

$$E_{re} = E_{im} = 0.1 \quad (4.15)$$

$$N = -0.0001 \quad (4.16)$$

Using the relations derived above, the parameter values from [8] are translated

as:

$$\begin{aligned}
 P &= 0.472 \\
 \alpha &= 3.0 \\
 \Delta\omega &= -0.005769 \\
 K &= 0.00913 \\
 T &= 600
 \end{aligned} \tag{4.17}$$

These constants will be used for time-series plots unless otherwise stated.

These parameter values were chosen to fall into the centre of an RW region identified in [8]. An investigation into RW events at this  $P$  value is therefore of high interest as a considerable amount of work in this thesis has utilised  $P = 0.5$ .

Without knowing the precise underlying causes of an optical rogue wave phenomenon, a precise definition is difficult. However, rogue waves are often characterised as rare, random events that are abnormally large. The threshold for being considered large is often chosen from one of the following definitions: 1) "the ratio between the height of the wave and the average wave height among one-third of the highest waves in a time series" [42] and 2) "any wave whose height is higher than the mean surface value plus  $8\sigma$  is considered a rogue wave" [42] ( $\sigma$  is the standard deviation). For the purpose of this study, I will employ the latter definition for a rogue wave amplitude. In the next section I begin an analysis of time-traces that produce rogue-waves (RW's) to understand the responsible mechanism and compare the amplitude and distribution of the RW events to gauge the appropriateness of the name.

### 4.2.2 Bifurcation Diagram

One of the first important numerical calculations that can be performed is that of a bifurcation diagram. A one-dimensional bifurcation diagram will quickly and easily identify the dynamics of the region. Analytical one-dimensional bifurcation diagrams were discussed in Sec. 2.3.

Fig 4.1 contains the one-dimensional bifurcation diagram in  $P$ . The y-axis contains the local maxima of the  $|E|^2$  found after integrating beyond the transient. The red-vertical line indicates the  $P$  value chosen for this chapter as defined in Eq. 4.17. For the parameter set chosen, the point of interest lies in the middle of a chaotic region, which agrees with the Lyapunov Exponent calculations performed

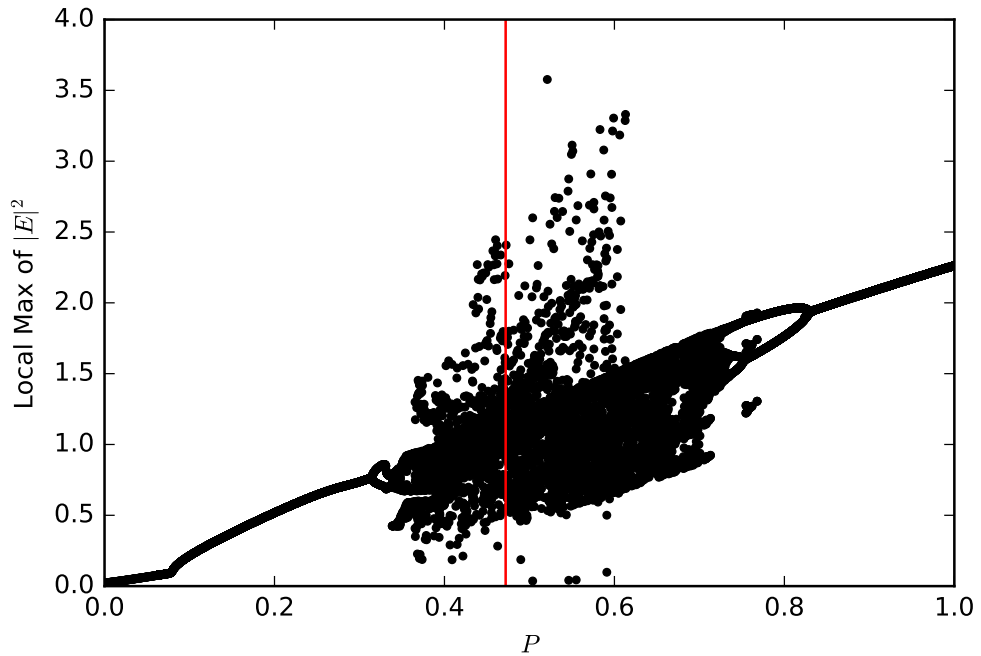


Figure 4.1: One-dimensional bifurcation diagram. The sweep is performed for varied  $P$ . The vertical red line indicates the  $P$  used for this investigation. Plotted along the y-axis are the local maxima found at a particular  $P$ .

for this region [8].

### 4.3 Time-Trace Analysis

The definition of an RW employed here is:

$$RW_{Limit} = |\bar{E}|^2 + 8 \sigma = 3.2 \quad (4.18)$$

where the first and second terms are the mean and standard deviation of  $|E|^2$  respectively. The value of 3.2 was determined from integrating the system for over a thousand nanoseconds.

Fig. 4.2 depicts a histogram plot of  $|E|^2$  integrated for 1000s of ns. The histogram shows a positively-skewed distribution centred near 1.0. The positive skew of the distribution is consistent with results presented for the original model (Eq.( 4.1)) [8], demonstrating that the expected behaviour has survived the transformation. The red dashed line indicates the RW threshold as calculated using Eq 4.18, which is found to be 3.2. Only after integrating for sufficiently long time, is a RW event located. This is indicated as the single measurement plotted to the right of the dashed red line. This confirms the existence of RW events numerically in our system. Furthermore, there is a distinct break in the continuum of  $|E|^2$ : from 2.7 to 3.2 the system does not visit any points before the RW event is detected. A similar plot was obtained experimentally in Fig. 2 of [8], where a distinct break in the continuum was also observed. However, more than one RW event was observed. This gap has not been established theoretically either in [8] (theoretical simulations suggests it fills) or this thesis (only one RW event was recorded). It is possible that a sufficiently long time-trace would cause this gap to fill, however RW events are still not completely understood and a break in continuum could be a distinct characteristic of RW events. More context is required and therefore the time-trace should also be investigated.

Fig 4.3 depicts the last 3300ns before the first RW event. The RW event and threshold are both indicated on the plot.

Starting with the parameters outlined previously, over 35000ns were iterated through ( $10^9$  steps) before the first RW event was discovered. After first detecting a RW location, the integration was restarted 3300ns before the event for plotting convenience. Starting (or continuing) integration from an arbitrary point along a time-series requires high numerical precision.

The C-Code in Sec B.1.1 are the routines derived to integrate the system. They are included for completeness and also as additional considerations were needed during their development that were not necessary in previous integration routines.

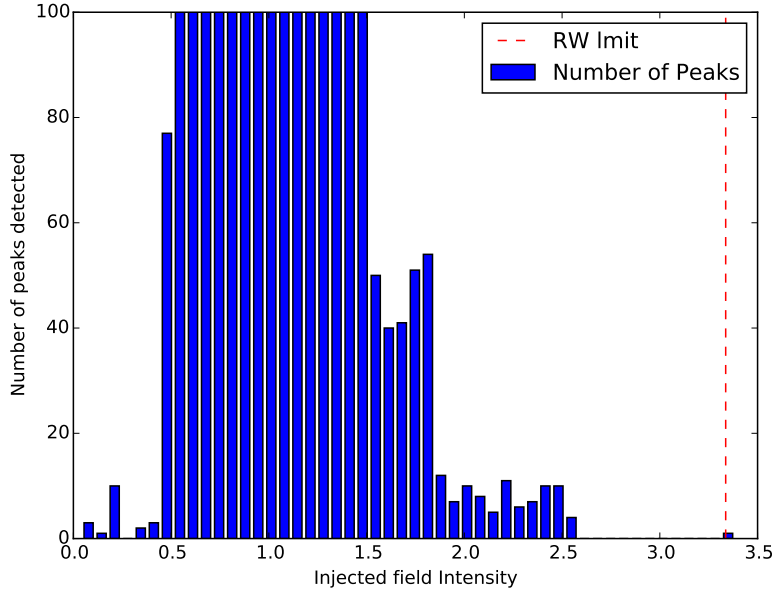


Figure 4.2: Histogram of  $|E|^2$  time-trace. The RW limit (dashed red line) was calculated using Eq. 4.18

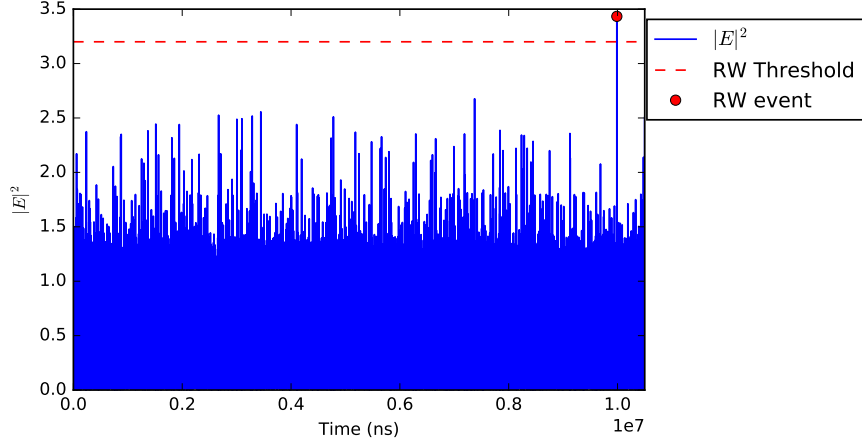


Figure 4.3: Time-trace segment of  $|E|^2$  (Blue) with an optical rogue-wave event in (Red dot). The red dashed line indicates the RW-Limit.

Careful inspection of Fig 4.3 shows that both before and after the RW event, no unusual  $E^2$  height is attained. Combining this with the continuum gap as noted in Fig 4.2, this could be considered the origins of quotes such as "appear from nowhere and disappear without a trace"[3], as no evidence to suggest that a RW event is about to occur or has just occurred.

As RWs appear to be rare random events, it was extremely useful to develop an integrator that could successfully be started at any point along a time-trace and produce the same numerical results without numerical noise or truncation errors

forcing the time-traces to deviate. However, the RW events are often located near chaotic[8] regions, and sensitivity to initial conditions must be considered. In order to arbitrarily integrate from any point in Fig. 4.3, numerical noise due to storing and passing an initial  $E - N$  state must be eliminated. To do so requires 17 decimal places [38] of precision. Secondly, a chaotic system will want to visit all points in the systems attractor without displaying periodic behaviour.

Ordinarily, it could be taken for granted that the size of the attractor is sufficiently larger than the number of points visited by integration, however with the current time-step (0.01 dimensionless time)  $10^9$  unique points were already used to find only the first RW event. Many more RW events will be needed to uncover their origins. Aside from estimating the size of the attractor that can be visited numerically before either a) the system begins to repeat itself or b) the system begins to settle on to a steady-state system with fewer (or no) RW events, the distribution of RW events can be investigated as a function of noise. If the addition of small noise effects does not affect the distribution of RW events, it can be assumed that the (finite-numerical) attractor has not yet been filled. If it appears that in the absence of noise RW events become rarer (or stop appearing altogether) it can be understood that the system has settled down onto a steady-state system. It is also likely that some-other unanticipated scenario can happen, however the important aspect of this approach is to ensure that the system remains in a chaotic state while being evolved numerically. To begin, the RW distribution is investigated without noise.

## 4.4 Rogue Wave Mean-Time

Fig. 4.4 depicts the location in time of 200 different RW events. The time in  $ns$  required for the laser to physically experience this number of RW events is  $2.2 \times 10^6 ns$ , or  $2.2ms$ .

Visually, the RW events appear to have a random maximum value. There is some clustering and spacing of RW points which would suggest the the RW events are also randomly distributed. To determine if the RW event are randomly distributed, the time-between consecutive RW events must be measured and a histogram should be made of the distribution. If the mean-time between rogue waves is well approximated by an exponential fit, then it can be understood that the mean-time is a randomly varying quantity. This is the expected result, as it has been shown in existing literature (experimentally and numerically) that RW events are randomly distributed in time [101].

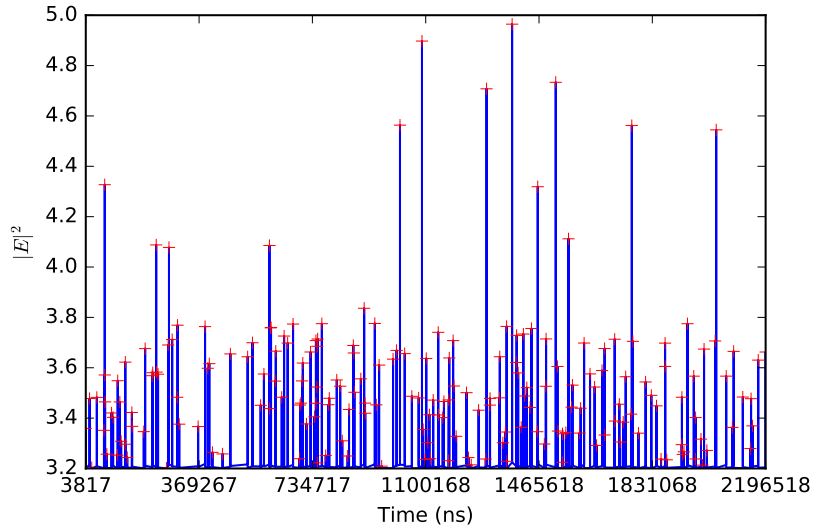


Figure 4.4: Time-trace plot indicating the detection of RW events. 200 separate RW events were detected after integrating the system for  $2.2 \times 10^6$  ns ( $\approx 1.3 \times 10^{10}$  steps with a time-step of 0.1).

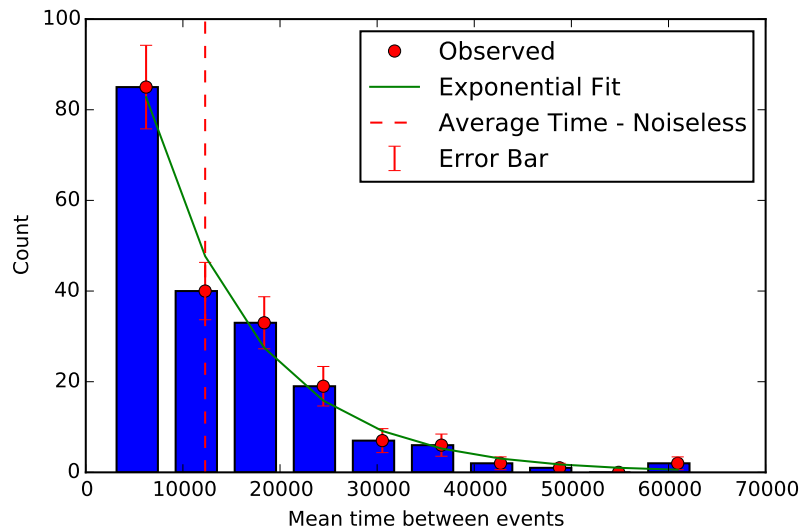


Figure 4.5: Histogram of time-between RW events. Blue bars are the binned observations. The green line is the least-squares fit of the Exponential Distribution. An error of the square-root of the numerical observation is assumed to be sufficient. The vertical red dashed line indicates the average time between observed events.

Fig 4.5 shows that that Exponential Distribution fits the observed data quite well, but not perfectly. The red dashed line indicates the average time between RW events. This is determined as  $\frac{\text{Timetaken}}{\text{numberofRWevents}} = \frac{2143593.259\text{ns}}{200} = 10881.2\text{ns}$ . This line intersects the second bin of observations, therefore it can be estimated that over 100 of the 200 RW events occur within  $12000\text{ns}$  of the previous RW event, and 130 of the events occur within  $15000\text{ns}$  of the previous event.

The fact that the time taken to observe the first RW point was  $35000\text{ns}$  means that the first RW mean-time is an outlier of this distribution but over 65% of the mean-times are below the average mean-time of  $11000\text{ns}$ . The initial point taken just happened to be sufficiently far away from the the RW events, but still lies within two standard deviations of the distribution.

The exponential-fit function used is defined as:

$$y(x) = ae^{-cx} \quad (4.19)$$

The fitting parameters  $a, c$  were determined to be 84 and 0.501 respectively. Here 0.501 (decay constant) corresponds to the inverse of the mean-time and is normalised to the bin size. Therefore, the centre of the second bin ( $\frac{1}{0.5} \approx 2$ ),  $12000\text{ns}$  should correspond to the mean time. This is of the same order as the mean time calculated from the total time taken to find 200 RW events. The close agreement of the exponential fit to the numerical data suggest that the RW events are indeed random, as the exponential function describes the mean-time between stochastic (random) events. Including this result, with the RW anomaly size analysis in Fig. 4.2, allows one to conclude that these events meet the criteria for RW events. That is, the RW events are rare, random and abnormally large optical phenomena. Therefore the remaining task is to attempt to determine the cause of the RW events.

In [101], a similar study was performed (with and without additive noise) with the same conclusion regarding a random time-distribution (see Fig. 2 of [101]). Another contribution from [101] is the observation that RW events could be predicted up to  $1.5\text{ns}$  before an RW occurs. This is an important first for optical RW events, however a complete explanation is still lacking. Therefore in the next section, I consider the similarity between RW events.

## 4.5 Rogue Wave Comparison

In Fig. 4.6 the time-series evolution of 4 RW events are examined. These are the first 4 RW events indicated in Fig. 4.4 and the common x-axis denotes time

4. ORIGINS OF ABNORMALLY LARGE  
'ROGUE WAVES' IN OPTICALLY  
INJECTED LASERS.

4.5 Rogue Wave Comparison

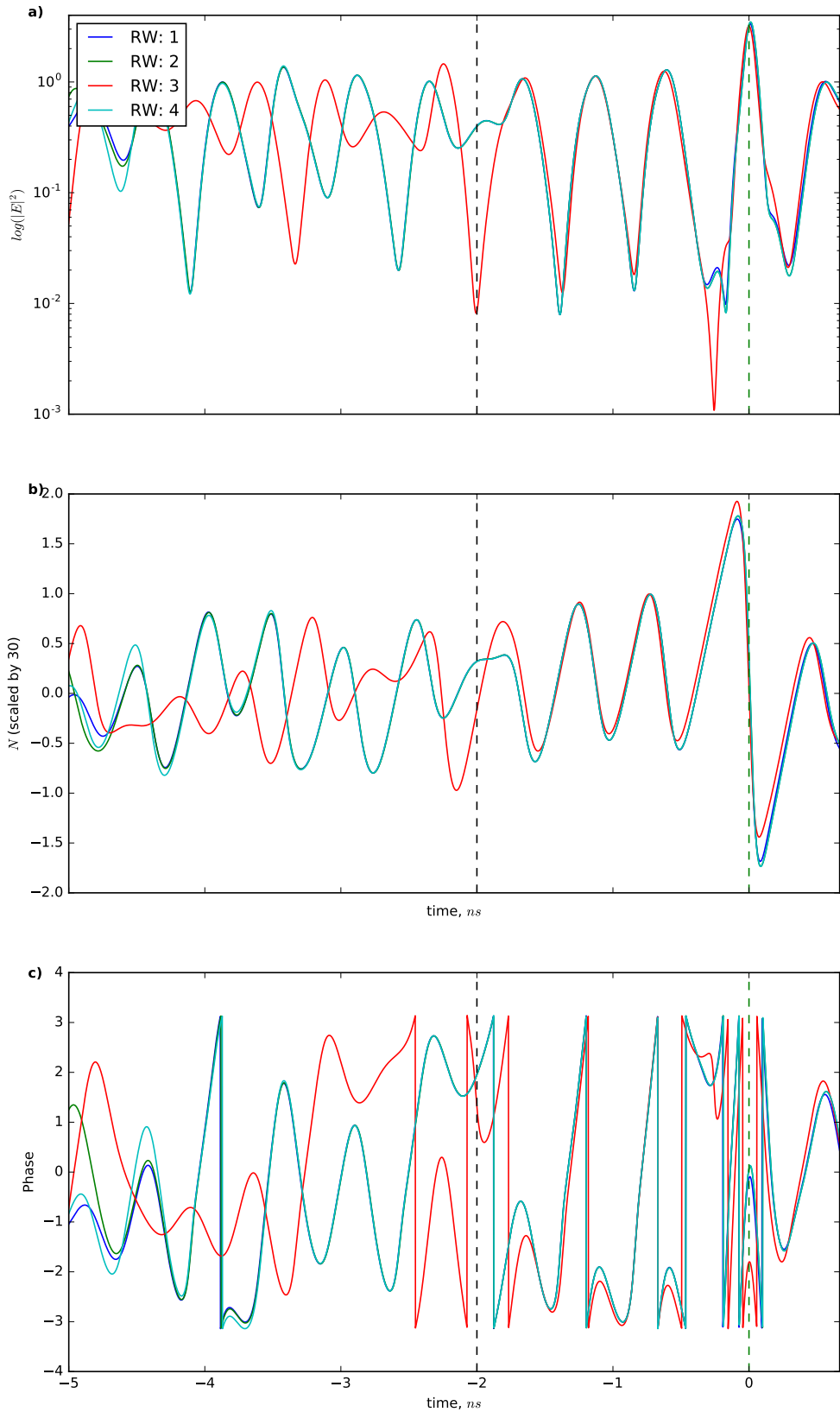


Figure 4.6: Time series of 4 RW events are plotted, aligned at the RW event. Plot of: **a)**  $|E|^2$  in a log scale. **b)**  $N$  (scaled  $\times 30$  to make features clearer). **c)** Phase of  $|E|$ . A black dashed line at  $2\text{ns}$  before the RW event and a dashed green line is used to indicate the time of the RW events.

( $ns$ ) before the RW event. The black dashed line at  $2ns$  before the RW event is intended to mark the beginning of time-region of interest.

The green dashed line at  $0ns$  denotes the RW event. Fig. 4.6(a) depicts the evolution of  $|E|^2$  on a log-scale, for each of the 4 sample RW events. Therefore, any such differences should be considered very small. In this plot, after the black dashed line, the values of  $|E|^2$  are almost indistinguishable (apart from a small deviation in RW:3, this is explained by a phase variation in  $\mathbf{c}$ )) until the RW event. A similar picture is presented in Fig. 4.6(b) and Fig. 4.6(c), from  $-2ns$  to  $0ns$  before the RW event, the plotted  $N$  and the phase (respectively) for all 4 RW events are almost indistinguishable.

This agreement between RW events (up to  $2ns$  before an event) has been demonstrated previously in [101], and thus-far the RW events in this chapter have primarily served to confirm the existence of RW events in the optically injected lasers utilised in this thesis. However, Fig. 4.6 contributes additional insight in the the understanding of RW events that is not yet demonstrated in the literature. This new insight comes from the comparison of  $\log(|E|^2)$  with  $N$  (Fig. 4.6(a) and (b) respectively). From inspection, it is evident that before an RW event (where  $|E|^2$  obtains a maximum value)  $N$  first must grow abnormally large. In addition,  $N$  can only grow sufficiently large if  $|E|$  remains very small.

A close study of Fig. 4.6(b) reveals that the  $N$  before the RW event is permitted to grow unusually large ( $N$  of RW:3 grows slightly larger than the other traces). The corresponding point in the  $|E|^2$  fields shows that they are simultaneously small (RW:3 smallest of all). Finally, at the RW event in each time-trace ( $0ns$ ) the abnormally large  $N$  is depleted to allow  $|E|^2$  to grow to an unusually large height that is the RW event. Assembling these pieces of information, one can theorise that this path that is followed from  $-2ns$  leads to an unusually large  $N$ , which in turn allows the abnormally large optical event. Understanding the origins of the RW events has now been reduced to understanding two smaller problems. That is, an explanation is sought for:

1. the conditions that allow this path to the RW to exist
2. the conditions necessary that ensure the system ends up on this path.

This regular RW behaviour and predictability (up to  $2 ns$ ) is in stark contrast to behaviour of the time-traces further from the RW event, where the time-traces do not appear comparable to one another. If the  $|E|^2$ ,  $N$  and phase of the  $E$ - $N$  space are said to evolve in the same way, as depicted in Fig. 4.6, it could be suggested that the system ends up on a path at  $-2ns$  that will ultimately result

in a RW event. From Sec. 4.4, one could conclude that this path is rarely and randomly visited.

## 4.6 Chimney and Spike Structure

Item 1 requires consideration of the local-maxima of the time-traces presented in Fig. 4.6(a) and (b). Both the time-trace of  $E^2$  and  $N$  go through local maxima between  $-2ns$  and  $0ns$ . However, these local maxima are monotonically increasing before the RW event. Therefore, an inspection of the Eqns. (2.101, 2.102) is required. Writing:

$$|E|^2 = Im^2 + Re^2 \quad (4.20)$$

where  $Im$  and  $Re$  are the real and imaginary parts of our complex electric field, Eqns. (2.101, 2.102) can be re-written as:

$$\dot{Re} = N(Re - \alpha Im) + \Delta\omega Im + K \quad (4.21)$$

$$\dot{Im} = N(Im + \alpha Re) - \Delta\omega Re \quad (4.22)$$

$$\dot{N} = \frac{1}{T}(P - N - (2N + 1)[Im^2 + Re^2]) \quad (4.23)$$

When  $N$  is a local max,  $\dot{N} = 0$  and therefore:

$$\frac{1}{T}(P - N - (2N + 1)[Im^2 + Re^2]) = 0 \quad (4.24)$$

$$(P - N - (2N + 1)[Im^2 + Re^2]) = 0 \quad (4.25)$$

$$P - N = (2N + 1)[Im^2 + Re^2] \quad (4.26)$$

$$\frac{P - N}{(2N + 1)} = [Im^2 + Re^2] \quad (4.27)$$

$$[Im^2 + Re^2] = |E|^2 = \frac{P - N}{(2N + 1)} \quad (4.28)$$

$$r = \sqrt{|E|^2} = \sqrt{\frac{P - N}{(2N + 1)}} \quad (4.29)$$

where  $r$  is the radius of the  $|E|$  field in polar coordinates. The surface defined in Eq. 4.29 describes a chimney-like surface. This surface describes three separate areas of dynamics:

1. On the surface ( $r = \sqrt{\frac{P - N}{(2N + 1)}}$ ) of this chimney  $\dot{N} = 0$

2. Inside the chimney ( $r < \sqrt{\frac{P-N}{(2N+1)}}$ )  $\dot{N} > 0$  and
3. Outside the chimney ( $r > \sqrt{\frac{P-N}{(2N+1)}}$ )  $\dot{N} < 0$

Now, let us consider the local max of  $|E|$ .

$$r = \sqrt{|E|^2} \quad (4.30)$$

$$\dot{r} = \frac{1}{2}(Im^2 + Re^2)^{-\frac{1}{2}} 2(Im\dot{Im} + Re\dot{Re}) = 0 \quad (4.31)$$

$$(4.32)$$

At  $\dot{r} = 0$ , only the numerator needs to be zero:

$$(Im\dot{Im} + Re\dot{Re}) = 0 \quad (4.33)$$

$$\begin{aligned} Im(N(Im + \alpha Re) - \Delta\omega Re) + \\ Re(N(Re - \alpha Im) + \Delta\omega Im + K) = 0 \end{aligned} \quad (4.34)$$

$$\begin{aligned} N(Re^2 + Im^2 + \alpha(ImRe - ImRe)) + \\ KRe + \Delta\omega(ImRe - ImRe) = 0 \end{aligned} \quad (4.35)$$

$$N(Re^2 + Im^2) + KRe = 0 \quad (4.36)$$

and solving Eq. 4.36 for  $N$  yields:

$$N = -K \frac{Re}{Re^2 + Im^2} = 0 \quad (4.37)$$

$$= -\frac{K \cos(\theta)}{r} \quad (4.38)$$

with:

$$\cos(\theta) = \frac{Re}{\sqrt{Im^2 + Re^2}} \quad (4.39)$$

The surface generated by Eq 4.38 define two areas of different dynamics:

1. Above the surface: ( $N > -\frac{K \cos(\theta)}{r}$ )  $r$  is increasing
2. Beneath the surface: ( $N < -\frac{K \cos(\theta)}{r}$ )  $r$  is decreasing

Fig 4.7 contains the combined chimney-spike structure described by the equations derived in this section. The time-trace begins outside the chimney, above the spike in the left-middle ground (initially:  $\dot{r} > 0, \dot{N} < 0$ ). From the point, the time-series evolves towards the reader and down through the spike ( $\dot{r} < 0, \dot{N} < 0$ )

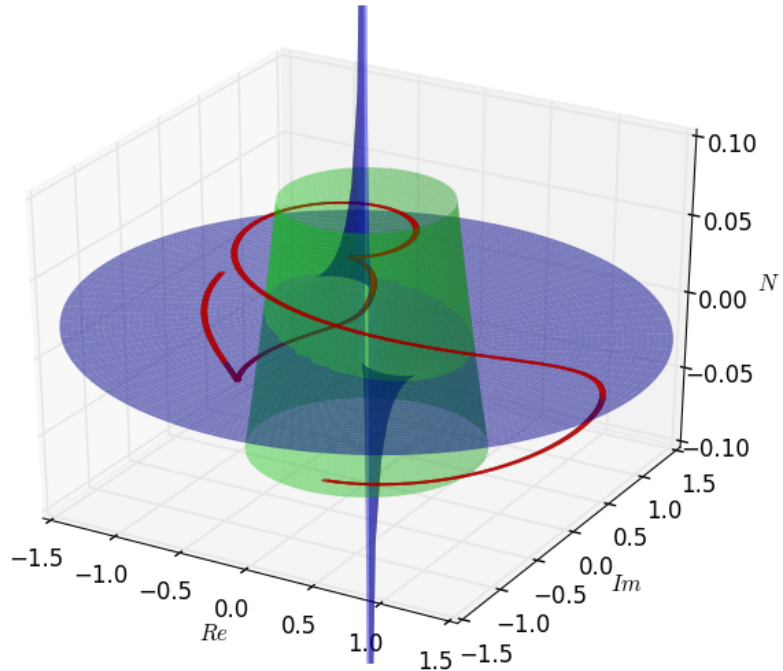


Figure 4.7: 3-D Chimney-Spike (green, blue respectively) structure with time-series ending with RW event (red).

and evolves towards the chimney. Inside the chimney ( $\dot{r} < 0, \dot{N} > 0$ ) the time-series begins to move upwards in  $N$  while shrinking in  $r$  until it crossed the spike surface again ( $\dot{r} > 0, \dot{N} > 0$ ). The time-series now evolves upwards and outwards until it crosses the chimney a second time ( $\dot{r} > 0, \dot{N} < 0$ ). The time-trace is evolved until it crosses the spike surface in the right-middle ground. From this figure, part of the RW behaviour is explained: the spike-surface contains a singularity at 0 and fits inside the chimney structure. Therefore, if a time-series was allowed to remain inside the spike ( $|E|^2$  small)  $N$  can be allowed to grow abnormally large. Once the time-series eventually crosses the spike, a larger than normal  $|E|^2$  will be observed. This coincides with the analysis of Fig. 4.6, and also with observations made in [101] regarding the trajectory of a RW events towards a saddle. In both examinations, the time-trace moves upwards while close to the axis until it approaches the unstable **foci** and is pushed outwards. In the chimney-spike structure, the time-series crosses the spike and  $|E|$  is now positive. This validation of the chimney-spike analysis motivates its continued use. A discussion on the importance of the saddle points of the systems will be included later with emphasis on their relation to the chimney-spike structure.

The width of the bottom of the spike is narrow, therefore the rarity of the RW events could be caused by the majority of time-traces crossing the spike-structure low down, where the time-trace then will evolve outwards towards the chimney structure sooner and the maximum  $N$  achieved will not be sufficient to create an RW event.

The next issue to resolve is the combination of conditions necessary to have a time-series evolve high enough in the spike-structure so the  $N$  can become sufficiently large. The next section considers a Poincaré Map approach in an attempt to find a path high into the spike structure.

## 4.7 Poincaré Map

In dynamical systems theory, a Poincaré Map is a mapping from a hyper-plane of the system to itself obtained by following the system evolution until the next intersection of the hyper-plane. In this section the Poincaré Map is generated by mapping points along the time-trace where the real and imaginary parts of  $E$  form a  $-45^\circ$  angle relative to each other. In Fig. 5 [101] a different Poincaré Map is chosen. In [101] the plane for the Poincaré Map is taken such that it contains the saddle point  $S1$  at  $N = 1.0036$ .

In the previous section, the mean time between RW events was estimated to be of the order of  $10000\text{ns}$ . Therefore, if an RW event is not found after  $11000\text{ns}$ , and a large number of intersection with the Poincaré map have occurred, it can be interpreted that the starting point is far from an RW event.  $11000\text{ns}$  is selected as a starting point for the integration limitation.

Fig. 4.8 contains the result of this approach. The coloured background represents the number of times the time-trace will pass through a phase of  $-45^\circ$  before an RW event is observed. The brown region corresponds to where four or more intersections were necessary before an RW event was found (many of these points did not find an RW point within the time-constraint, but many intersections with the map were found).

The red circles are the intersection of the time-trace with the map. The last four points of the time-trace were coloured white to identify the transition between regions more easily. Starting with the bottom left, the white point is intersection with the map four intersections before the RW event. From here, the transition from between regions towards the RW event is easily identified with the white points in the orange, green and light blue (three, two and one intersections before RW event.) The dark blue region corresponds to points that

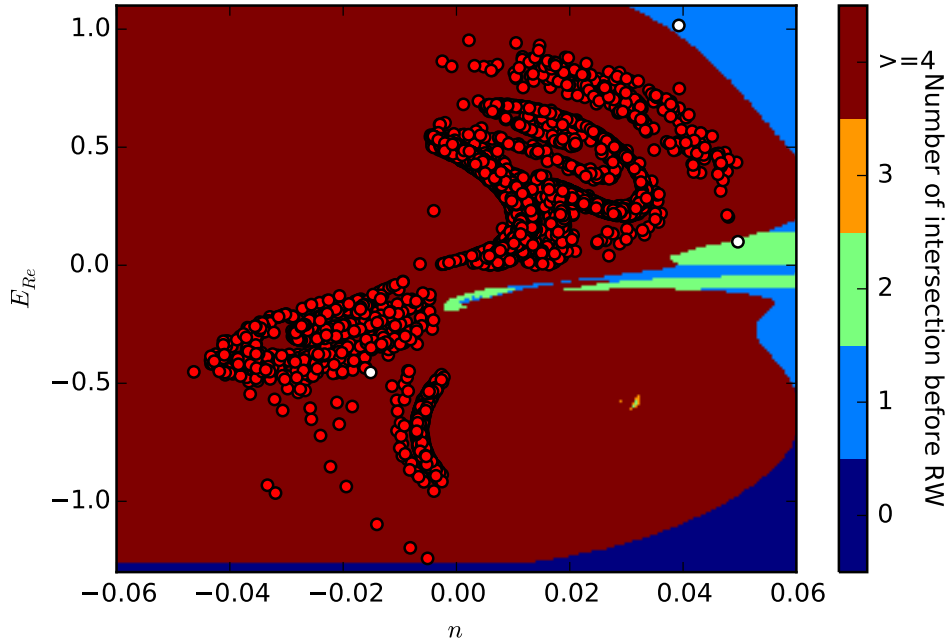


Figure 4.8: Poincaré Mapping of  $\theta = -\frac{\pi}{4}$ . The colour-bar indicates the number of times a point on the time-trace will have before an RW event. The circular points are the intersections of a sample time-trace with the map.

start at a phase of  $-45^\circ$ , but do not intersect again before the RW event. This is due to starting on a sufficiently large  $E$  inside the chimney structure, where  $N$  can still increase and  $|E|$  will be greater than the RW threshold before the next intersection with the hyper-plane.

The aim of this approach was to identify the beginning of a path where a typical time-trace can begin and be guaranteed to produce an RW event. However, the iterated regions do not appear to clustered (multiple green regions separated by other colours) and a very high raster is needed to form small regions. For example the orange cluster in the lower right was only visible after 500 points were calculated along  $Re$  and  $N$  for the background. Also in many regions, even at this raster, many points on the Poincaré section did not start sufficiently close to the time-trace to find an accurate count for the remaining number of sections. For example the white dot in the lower left will undergo three more intersections with the hyper-plane before an RW event, but the surrounding area is marked as red. This suggests that a very small orange region is located in this vicinity but is not visible at this resolution. Given that a very high resolution is already used in Fig. 4.8, a different choice of hyper-plane may yield a more fruitful Poincaré type map.

### 4.7.1 Maximum $N$ Poincaré Section

In Sec. 4.6 the chimney-spike structure was introduced to graphically illustrate regions of growth and decay in the governing rate-equations. The spike (resulting from a singularity at  $E = 0$ ) in Fig. 4.7 is shown to make the RW possible by allowing the  $N$  to grow abnormally large. The Poincaré Map in Sec. 4.7 was an attempt to find a path that would lead to an RW event by measuring the intersection of a time-trace with a phase of  $-\frac{\pi}{4}$ . This did not succeed entirely and now a new map is considered. In this section, the analysis of the chimney-spike structure is extended in that a chimney colouring is sought for two mappings:

1. Maximum  $N$  obtained from starting on the chimney
2. Number of intersections with the chimney before an RW event.

It is hoped that both these mappings will shed light on the a more general triggering mechanism for the RW event. Presently two trivial ways of triggering an RW event have been discovered:

1. Starting integration with  $E$  at an abnormally large value, in a region where  $|\dot{E}|$  and  $\dot{N} > 0$
2. Starting with a very small  $|E|$  inside the chimney with a trajectory that takes the time-series trace high into the spike-surface.

The latter is the more interesting situation, but the question remains how does the system end up onto such a trajectory. As the chimney-spike structure is the structure of interest, an analysis of the saddle points will be conducted to fulfil this aim. The saddle points are found where  $\dot{E} = 0$  and  $\dot{N} = 0$ . From Eqn. (2.101), setting  $\dot{E} = 0$  and solving for  $E$  yields:

$$E = \frac{-K}{N + i(\alpha N - \Delta\omega)} \quad (4.40)$$

Equating Eqn(4.29) with Eqn(4.40) and simplifying the polynomial equation in  $N$  is obtained for the saddle points.

$$\frac{P - N}{2N + 1} = \frac{K^2}{(N^2 + (\alpha N - \Delta\omega)^2)} \quad (4.41)$$

$$(P - N)(N^2 + (\alpha N - \Delta\omega)^2) = K^2(2N + 1) \quad (4.42)$$

$$\begin{aligned} P(N^2 + (\alpha N - \Delta\omega)^2) - N(N^2 + (\alpha N - \Delta\omega)^2) &= K^2(2N + 1) \\ PN^2 + P(\alpha^2 N^2 + \Delta\omega^2 - 2\alpha N \Delta\omega) - N^3 \\ -N(\alpha^2 N^2 + \Delta\omega^2 - 2\alpha N \Delta\omega) &= K^2(2N + 1) \\ N^3(1 + \alpha^2) + N^2(-P - \alpha^2 P - 2\alpha \Delta\omega) + \\ N(2\alpha \Delta\omega P + \Delta\omega^2 + 2K^2) + K^2 - P \Delta\omega^2 &= 0 \end{aligned} \quad (4.43)$$

Eqn. (4.43) implies that the saddle  $N$  co-ordinates of the saddle points can be estimated as  $n = P, n = -0.5$  and the roots of  $n^2 + (\alpha n - \Delta\omega)^2 = 0$ . The roots of Eqn. (4.43) can be solved numerically for exact results. Using the parameters defined in Sec. 4.5, the  $N$  co-ordinates of the saddle points are: 0.41792, -0.00584 and 0.00245. Note the leading  $N$  is very close to the  $P$  value used in this investigation. It is also the largest of the three  $N$  co-ordinates and may be related to the RW event.

Figs. 4.9 to 4.11 depicts the time-series evolution of a point starting near a saddle in reverse time. The red points are the saddles and the green points are the end of the time-series for reverse-time.

In [101], a combination of elements from Figs. 4.9 to 4.11 were presented with a sample RW event. It was demonstrated that the time-trace followed closely the one-dimensional sub-manifold before the onset of a RW event. Here the chimney-spike structure has been plotted over each saddle-point, and a trajectory towards each saddle point, to determine the effect (if any) of the saddle points on the RW events.

The C-code in App. B.1.1 includes a routine for solving stiff systems. This is necessary as the ODE that describes the model represents a dynamical system that can be numerically unstable, particularly if the system is modelled in reverse time with a large time-step. Several issues merit consideration when a dynamical system is integrated backwards, including that the stability of fixed points can change and that the equation can contain terms that may lead to rapid variation in a solution. Firstly, the change in stability means that a time-series can converge to a point or limit cycle that was previously not reachable. Secondly, if the time-step is not sufficiently small, the trajectories obtained may diverge from the correct evolution, particularly in a region where multiple trajectories, in forward time, with vastly different origins, would converge to a point. If too large a time-

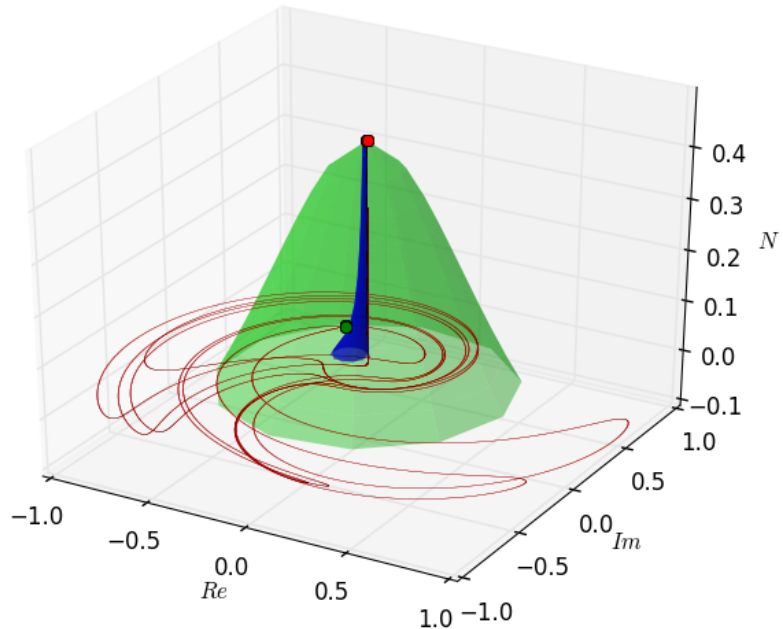


Figure 4.9: Saddle:  $n = 0.41792$ . The red trace beginning (in forward time) at the green point will eventually lead to the red point (saddle). The green structure is the chimney which is shown to close near  $n = P$ . The blue structure is the spike which is shown to become quite narrow near  $n = P$ .

step is taken, the time-series may end up following the wrong path numerically.

Fig 4.9 shows that the trajectory, in forward time would rise upwards in the chimney-spike structure as desired for an RW event. Therefore, an analysis of the dynamics involving this point are necessary. Fig. 4.10 and 4.11 suggest that the trajectories towards the other saddle points exist predominately in the  $Re - Im$  plane and may not contribute strongly to the RW events.

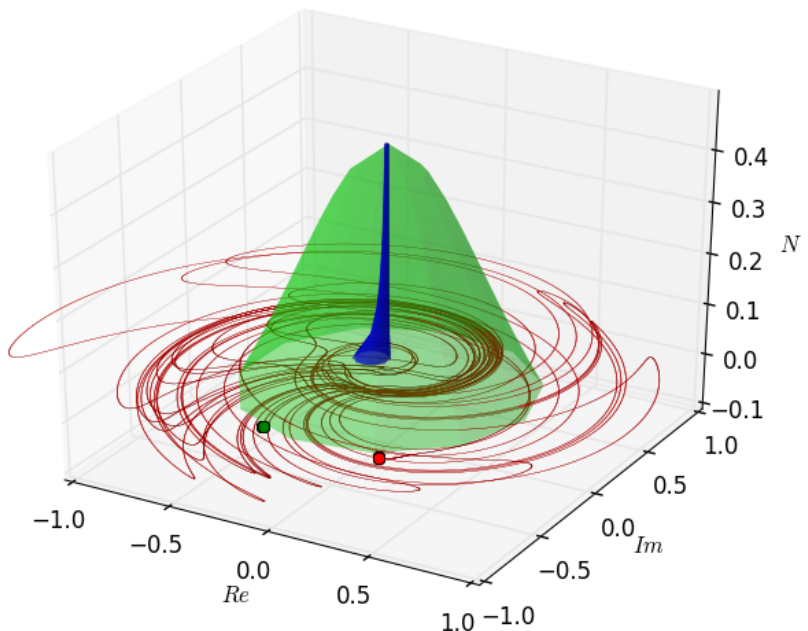


Figure 4.10: Saddle:  $n = -0.00584$ . The red trace beginning (in forward time) at the green point will eventually lead to the red point (saddle). The blue structure is the spike which is shown to become quite narrow near  $n = P$ .

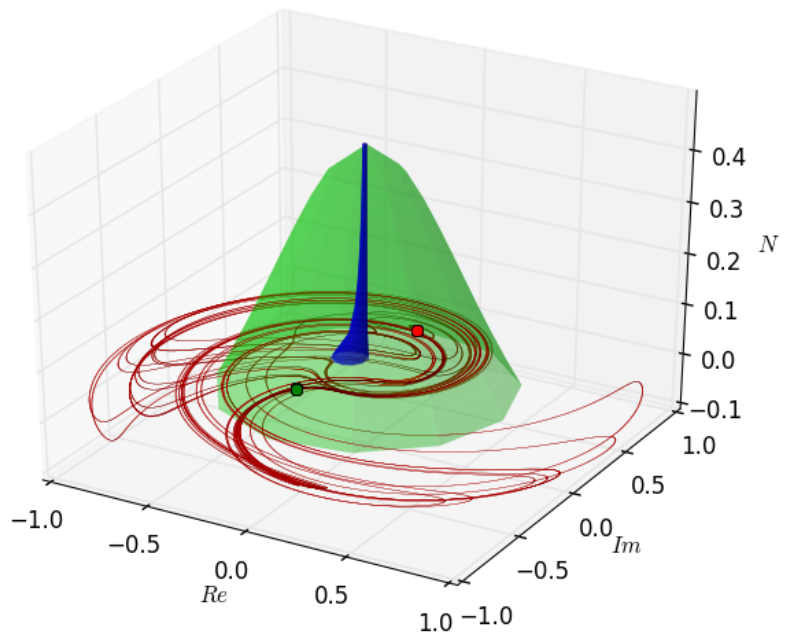


Figure 4.11: Saddle:  $n = 0.00245$ . The red trace beginning (in forward time) at the green point will eventually lead to the red point (saddle). The blue structure is the spike which is shown to become quite narrow near  $n = P$ .

## 4.8 Fast-Slow Dynamics

A close examination of Fig. 4.9 shows that the saddle node trajectory and sample RW trace both travel very close to the  $N$  axis with consistently small  $|E|$ . However, the saddle node trajectory is only known numerically and an analytical form for the evolution close to the  $N$  axis would be desirable. It has already been noted that in the spike-structure,  $N$  continues to vary while  $E$  is approximately constant. Following this observation, one can conclude that a slow manifold may exist nearby and separation of time-scales may be appropriate if the change in  $|E|$  is sufficiently small (negligible) compared to the evolution of  $N$ . This is in support of the dynamics witnessed in Fig. 4.6.

In Eq. 2.101- 2.102,  $T$  is the ratio of the two time-scales in the semiconductor laser: namely the ratio of the lifetime of the electron-hole pairs to that of the photons. To simplify the separation, a re-scaling of the system with  $T = 1/\tilde{\epsilon}$  and  $t \rightarrow \tilde{\epsilon}t$  (when  $T$  is large,  $\tilde{\epsilon}$  is small) Eq. 2.101- 2.102 reduces to:

$$\tilde{\epsilon} \frac{d}{dt} E = (1 + i\alpha) NE - i\Delta\omega E + K \quad (4.44)$$

$$\frac{d}{dt} N = P - N - (2N + 1)|E|^2 \quad (4.45)$$

and there are now two manifolds to consider, depending on the limit taken of  $\tilde{\epsilon}$ . Generally speaking, the separation of time-scales will work better with decreasing  $\tilde{\epsilon}$ .

### 4.8.1 Slow Manifold

In the limit of  $\tilde{\epsilon} \rightarrow 0$ , the LHS of Eq. (4.44) tends to zero and  $E$  becomes an additional parameter(constant) in Eq. (4.45)

$$0 = (1 + i\alpha) NE - i\Delta\omega E + K \quad (4.46)$$

This now places the evolution of the system onto the slow-manifold, where the  $E$  field is varying very slowly relative to the change in  $N$ . Note that Eq. 4.46 is again the  $\dot{E} = 0$  formula as derived in Eq. (4.40).

The solution for  $E$  becomes:

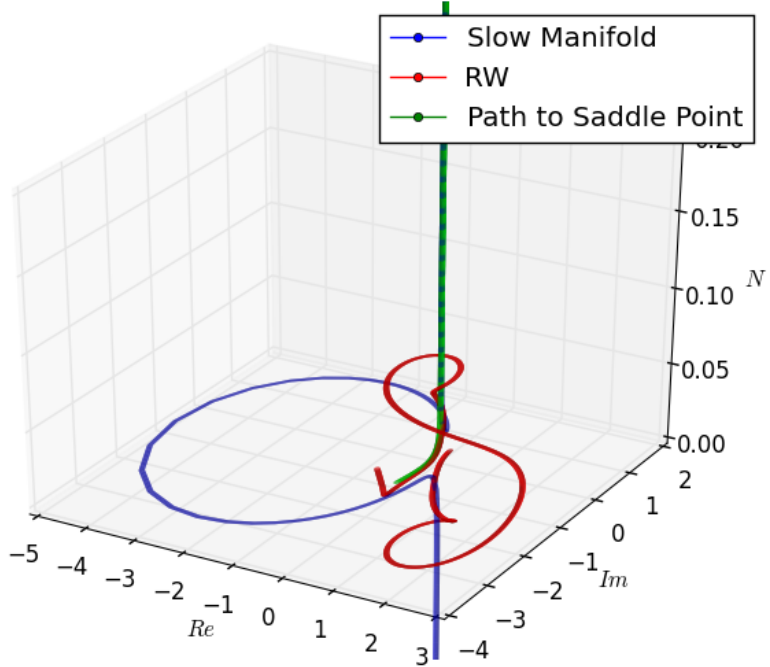


Figure 4.12: Combined figure of Slow Manifold (Blue), RW time-series and event (Red) and path to Saddle point (Green)

$$E = \frac{-K}{(1 + i\alpha)N - i\Delta\omega} \quad (4.47)$$

$$E = \frac{-K}{(1 + i\alpha)N - i\Delta\omega} \frac{N - i(\alpha N + \Delta\omega)}{N - i(\alpha N + \Delta\omega)} \quad (4.48)$$

$$E = -K \frac{N - i(\alpha N + \Delta\omega)}{N^2 + (\alpha N + \Delta\omega)^2} \quad (4.49)$$

This means that part of the slow manifold should be contained within evolution of the time-series towards the highest saddle points as the slow manifold forms part of the third-order polynomial that describes the location of the saddle points. From Fig. 4.9 it is clear that only this saddle point will draw the evolution of the time-series upwards into the spike-structure.

Fig 4.12 contains a combined figure of the slow-manifold, an RW event and the time-series that converges to the highest saddle point (similar to Fig. 3(c) of [101]). In the upper half of the plane, the slow-manifold and the path to the saddle converge as expected. In the lower half of the plane, the slow-manifold diverges from the saddle trajectory. The RW trace is seen to follow the slow

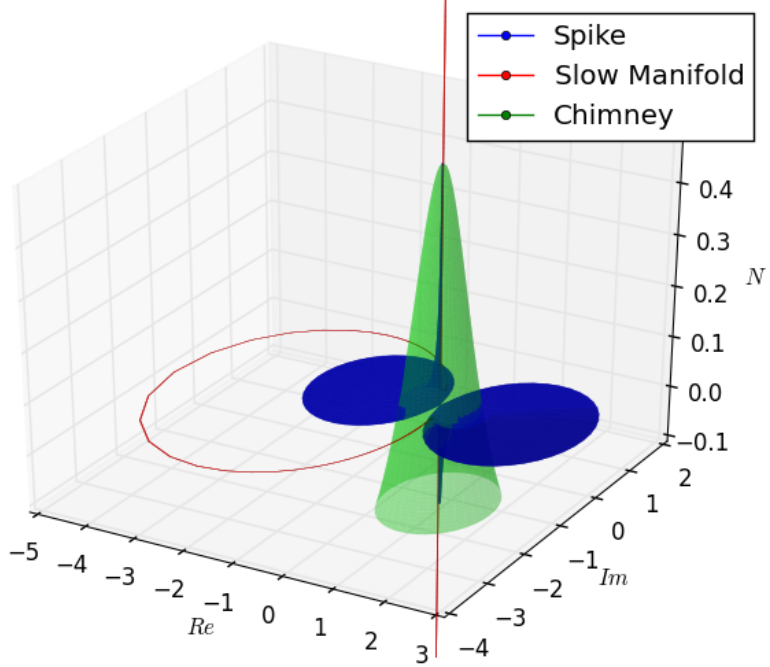


Figure 4.13: Figure containing segments of the Spike-structure, Chimney-structure and the Slow-Manifold.

manifold while in the lower-half of the plane but then diverges rapidly. Therefore, the slow manifold provides an analytical approximation of the trajectory to the saddle point close to the  $N$  axis. According to Eq (4.41), the separation between between the saddle trajectory and the slow manifold shrink as  $N \rightarrow P$  which agrees with the results presented.

Fig. 4.13 shows the slow-manifold with the spike-structure and chimney-structure. It's clear that the slow-manifold is not contained entirely within the chimney structure as the slow-manifold is a one-dimensional sub-manifold that exists on the two-dimensional spike-structure. An analysis of the stability of the slow-manifold is required.

By splitting up Eq. 4.49 into the real and imaginary parts the following equations are obtained:

$$\text{Re}(E) = -K \frac{N}{N^2 + (\alpha N + \Delta\omega)^2} \quad (4.50)$$

$$\text{Im}(E) = K \frac{(\alpha N + \Delta\omega)}{N^2 + (\alpha N + \Delta\omega)^2} \quad (4.51)$$

Also by substituting Eq. (4.47) into Eq. (4.45), the full slow-manifold equation is obtained, namely:

$$\frac{d}{d\tau}N = P - N - (2N + 1) \left| \frac{-K}{(1 + i\alpha)N - i\Delta\omega} \right|^2 \quad (4.52)$$

$$\frac{d}{d\tau}N = P - N - \frac{(2N + 1)K^2}{N^2 + (\alpha N + \Delta\omega)^2} \quad (4.53)$$

The roots of Eq. 4.53 would be another polynomial with non-trivial roots (trivial root near  $P$ ). Setting the LHS of Eq. 4.53 to zero and applying a simple re-organising reveals (into Eq. 4.54) that the stability of the slow-manifold is related to the chimney-structure.

$$\frac{P - N}{(2N + 1)} = \frac{K^2}{N^2 + (\alpha N + \Delta\omega)^2} \quad (4.54)$$

Where the LHS of Eq. 4.54 is  $|E|^2$  as derived in Eq. (4.29) to be the chimney-structure equation.

Fig. 4.14 depicts the sign and value of  $\dot{N}$  as  $N$  is varied. For small, positive  $N$  up to  $N = P$ , the slow-manifold is stable and will pull a nearby trajectory upwards. A nearby trajectory will continue upwards until it crosses the spike-structure. How close a trajectory is to the slow-manifold should therefore have a measure of influence over the maximum height obtained in  $N$ , and therefore the max  $|E|$  obtained. Therefore, an easy calculation would be to determine the maximum  $N$  obtained of trajectories beginning on the chimney structure close to intersection of the slow-manifold with the chimney.

In Fig. 4.15, the chimney-structure is plotted with colour scheme according to the future evolution of a trajectory beginning a point on the chimney surface. The upper half of the chimney is coloured blue, as  $\dot{r}$  is positive here and all trajectories move outward the chimney, and therefore are of little importance. The lower half of the chimney-structure (here:  $\dot{r} < 0$ ) is yellow/red according to the maximum  $N$  reached. A clipped/normalised colour scheme is applied to  $N$  values reached: The lowest 75% of the  $N$ 's are yellow, 75% – 100% are orange-red coloured. This highlights the region(s) where highest  $N$  values are achievable. The black line marks the trajectory to the saddle-point and crosses the chimney in a cluster of these red points.

The bands of red suggests the entry points on the chimney that allow large  $N$  exist in thinly spread rings. Following the red areas allow for large  $N$  to occur

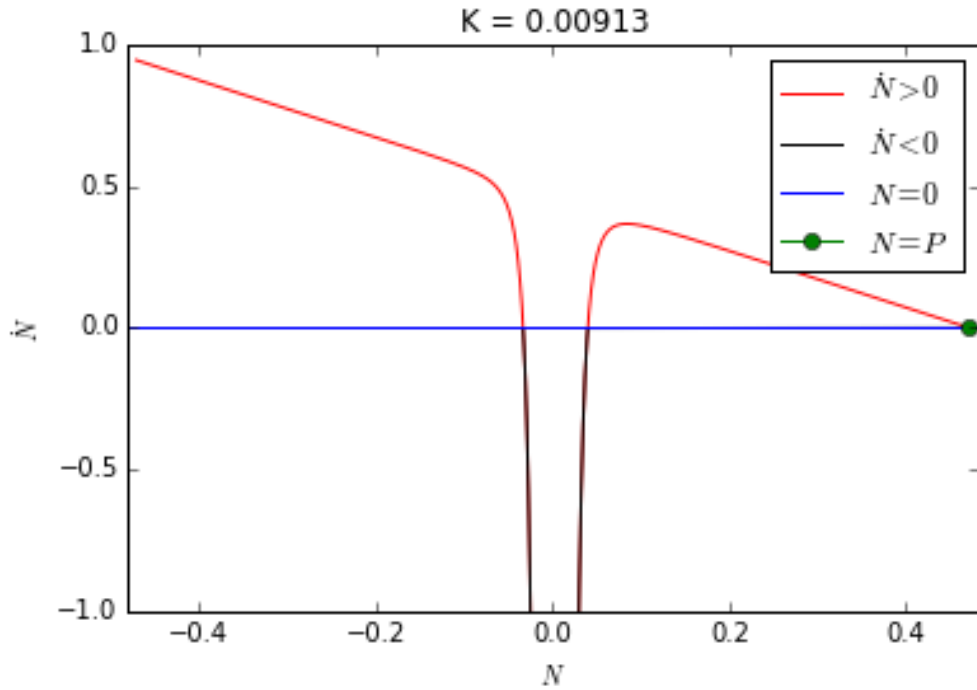


Figure 4.14: Plot of  $\dot{N}$  against  $N$ . The plot is coloured according to the sign of  $\dot{N}$ .

(and by extension, large  $|E|$ ). Following these points forward show that they do in-fact reach large  $|E|$ , but do not trigger the RW threshold (maximum  $|E|$  obtained is of the order  $\approx 3$ , but less then the RW limit of 3.2). This means that trajectory has to be very close to the saddle point trajectory, and that this trajectory is not attractive on the chimney surface. Therefore the key to the RW trajectory is intersecting the saddle point trajectory in a region where it is attractive.

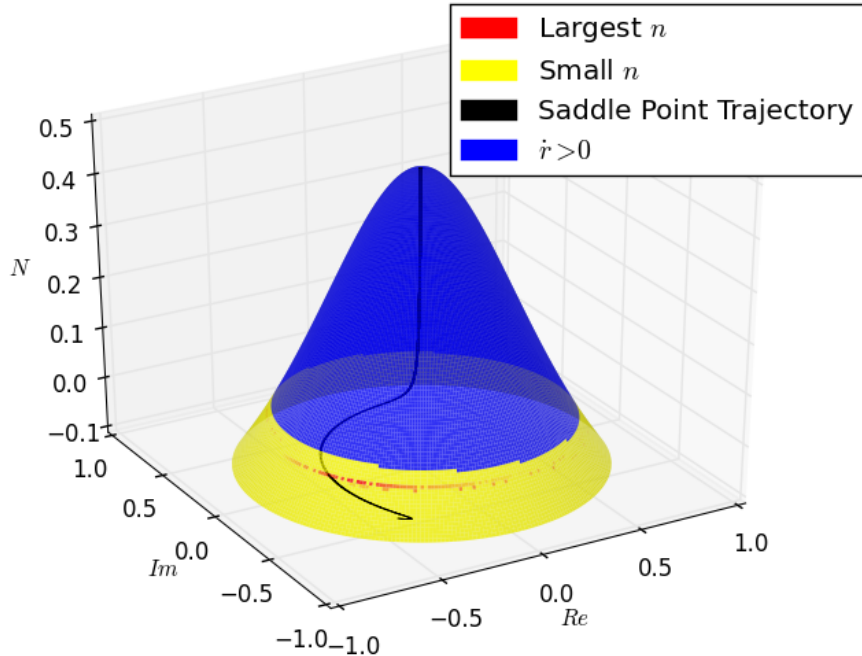


Figure 4.15: Chimney coloured according to height in  $N$  achieved. The highest 25% are shaded orange. The largest  $N$  is shaded red.

## 4.9 Rogue Wave Dynamics in Two-Mode Laser

To fully reconcile this chapter with the hypothesis of this thesis, the existence of RW and usefulness of the results uncovered here must be applied to two-mode lasers. Fig 4.1 depicted that the single-mode laser was in the middle of a chaotic region and therefore, the first step in moving towards a two-mode laser should therefore begin in a similar region if the results are to have any meaning. Two mode rate equation model (derived in Chap. 2 and utilised in Chap. 3) is now integrated for the same parameter space as for the single mode laser. The significant change in moving from the single mode to the two mode laser is the consideration of the non-linear gain, which involves changing of the parameter  $\epsilon$ .

### 4.9.1 $\epsilon = 0.01$

Fig. 4.16 shows that at the same parameter selection, the Two-mode laser is possibly also in a chaotic region. The red line indicates the current  $P$  value chosen. At this value, the two-mode laser appears to be in a region with a large number of local maxima. From numerical integration at this point, the RW

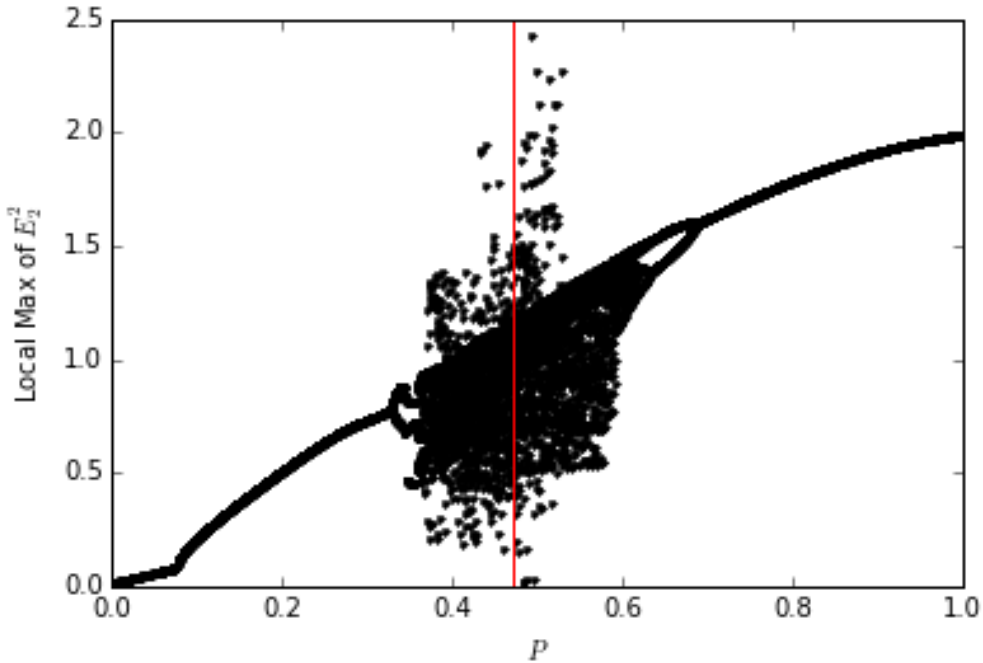


Figure 4.16: One-dimensional bifurcation2 diagram of  $E_2$  for the Two-Mode Laser. The sweep is performed over a varied  $P$ . The red vertical line indicates the chosen  $P$  for this investigation.

threshold for the two-mode laser is 2.99, which is less than for the single-mode laser.

Integration of the two-mode laser forward did not reveal an RW event larger than the threshold value calculated. The integration results are shown in Fig. 4.17. It now emerges that the Two-mode laser is operating in a two mode chaotic state.

To construct a similar chimney-spike structure for the two-mode laser would be beyond a trivial extent of the work presented here. For the two-mode laser, the number of variables ( $N$  and the real and imaginary parts of  $E_1$  and  $E_2$ ) increase to 5. Therefore, at best only sections of  $\dot{N}$  and  $\dot{E}$  surfaces could be plotted (holding some coordinates constant). However, an examination of the two-mode laser equations show an identical  $N$  dependence on the  $|E_1|^2$  and  $|E_2|^2$ . Also as two  $E$  fields are present, there are now possibly two spiking structures that could allow for the generation of RW events. This is left as future work. However, an investigation into the existence of paths to an RW event in a two-mode laser is not as trivial simply as adding a second mode.

Considering this, Fig. 4.17 clearly indicates that we are in a particular chaotic regime with maximum  $|E|^2$  of 1.5 compared to higher maximas on either side. In

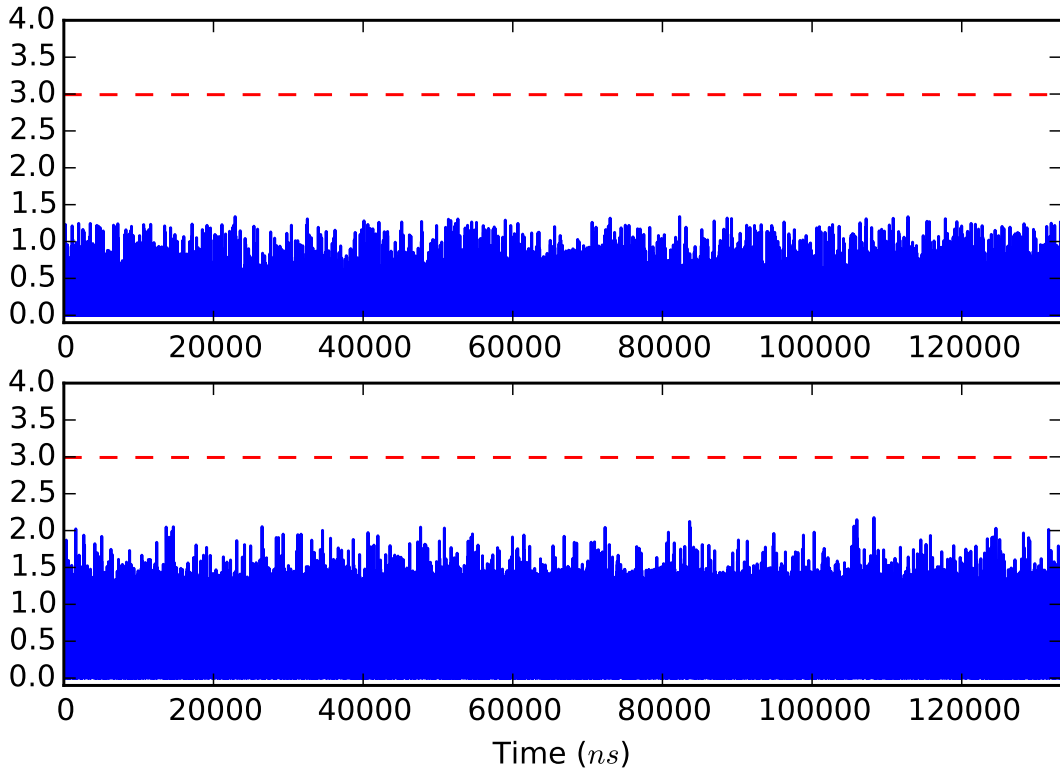


Figure 4.17: Integration of Two mode laser at for the same parameter space as the single mode laser. Top panel:  $|E_1|^2$  (uninjected mode). Bottom panel:  $|E_2|^2$  (injected mode)

order to produce an RW event in a two-mode laser an alternative  $P$  value may be required.

Finally, an investigation into the effect of noise is necessary to complete the work within the outlined scope.

## 4.10 Effect of Small Additive Noise on Rogue Wave Occurrence

The presence of noise in lasers is an unavoidable problem. Most external influences can be accounted for, or indeed removed through careful setup and isolation of the experiment. However, not all forms of noise can perfectly isolated and some sources of noise include spontaneous emission within the laser itself. Therefore a decision must be made when modelling the physical system if the remaining noise is significant and therefore must be included in the model, or that the effect of the noise is negligible and ignored in the model. Until now, the models in this thesis assumed noise was negligible and have been accurate in the most part, in their

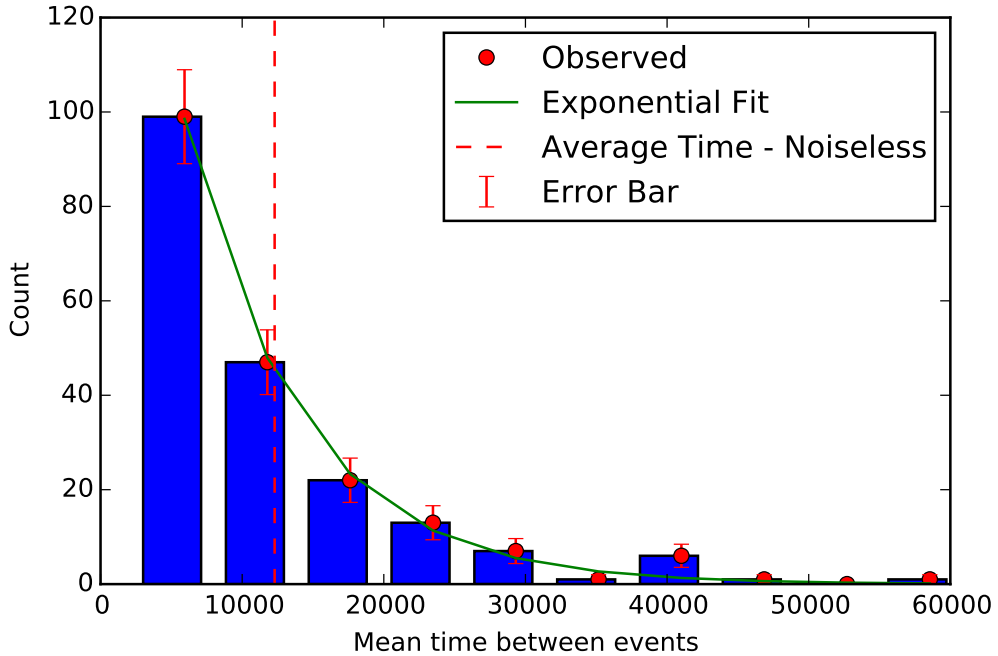


Figure 4.18: Poisson fit to mean-time between rogue waves. Small additive noise of the order of  $10^{-5}$  has been added to the  $Re$  at each integration step

predictions of the lasers' evolution. The literature on RW events have considered both noisy and noiseless systems. The current opinion [72] on the effect of noise on optical RW events is that noise can either enhance or suppress the occurrence of RW events via current modulation.

In this section, small additive noise is added to the RHS of Eq.( 2.101). In the absence of noise, integration was performed until 200 RW events were recorded. The number of steps required to find 200 RW events in a noiseless system was of the order of  $1.3 \times 10^{10}$ . With the addition of noise, integration was performed until either 200 RW events had occurred, or the number of steps taken had reached  $1.3 \times 10^{10}$ . From this an easy conclusion may be drawn on the effect of noise of RW occurrence, that is it can be found whether the presence of noise increases or decreases the mean-time between RW events.

To study the effect of noise, a range of amplitudes are added (to the real part of  $E$ ) of the order of  $10^{-3}$  or smaller in an attempt to measure any influence noise may have on the system.

Fig. 4.18 shows the Poisson fit to mean-time between RW events after the addition of small additive noise to  $E_{Real}$ . The Poisson agrees quite well with the numerical observations, the effect of the noise seems to have decreased the time between events. Previously, in Fig. 4.5, 130 of the 200 RW events had occurred

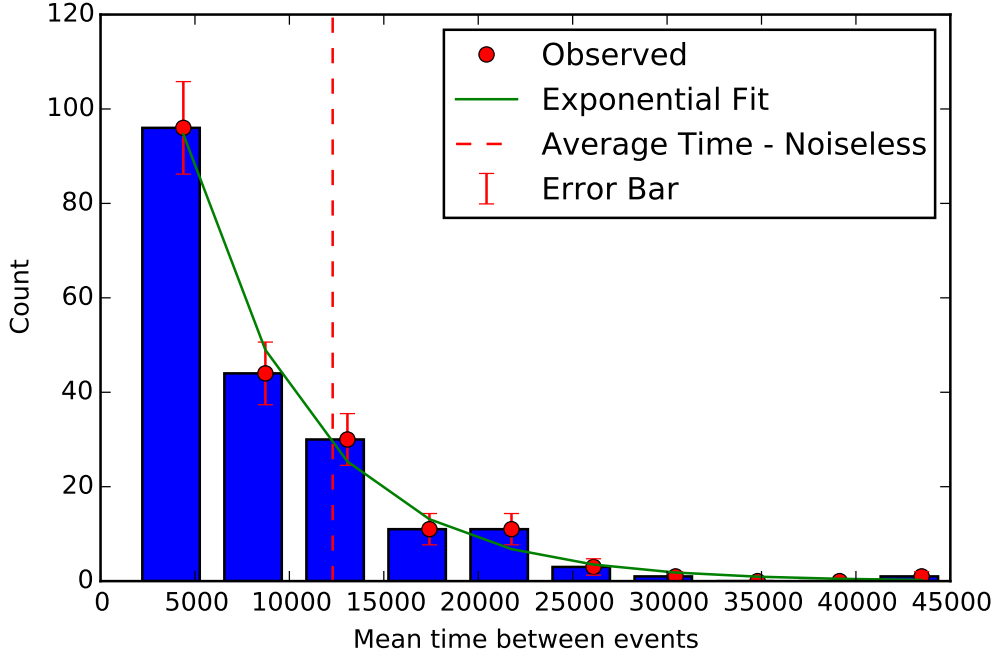


Figure 4.19: Poisson fit to mean-time between rogue waves. Small additive noise of the order of  $10^{-4}$  has been added to the  $E_{Real}$  at each integration step

within  $10000\text{ns}$  of the next event, where after the addition of noise that number is now 150.

Larger noise has been added in Figs. 4.19 and 4.20. The effect of the noise is consistent with results seen in Fig 4.18. As the noise is increased, the mean time between RW events decreases.

The results are discussed here and show that RW events are not only present in the absence of noise, but also in noisy systems (confirming previous reports). Additionally, (and previously not reported) Fig. 4.21 depicts graphically the change in RW mean-time as noise is increased. Although only four data points are used, a strong agreement is shown with the exponential decay function.

This is an important result as it would, theoretically, mean that RW events can occur in single-mode lasers with or without the presence of noise. Furthermore it demonstrates that RW events are more likely to occur in the presence of noise, and therefore may be occurring in already implemented devices. A similar result has been reported in [2], where the effect of current modulation affected the occurrence of RW events. The threshold for an RW event used was the same value that was used for all single mode calculations (3.2). However, given that the RW events occur more often with strong noise, a new threshold may need to be calculated as their increased presence will contribute to the mean of  $|E|$  and

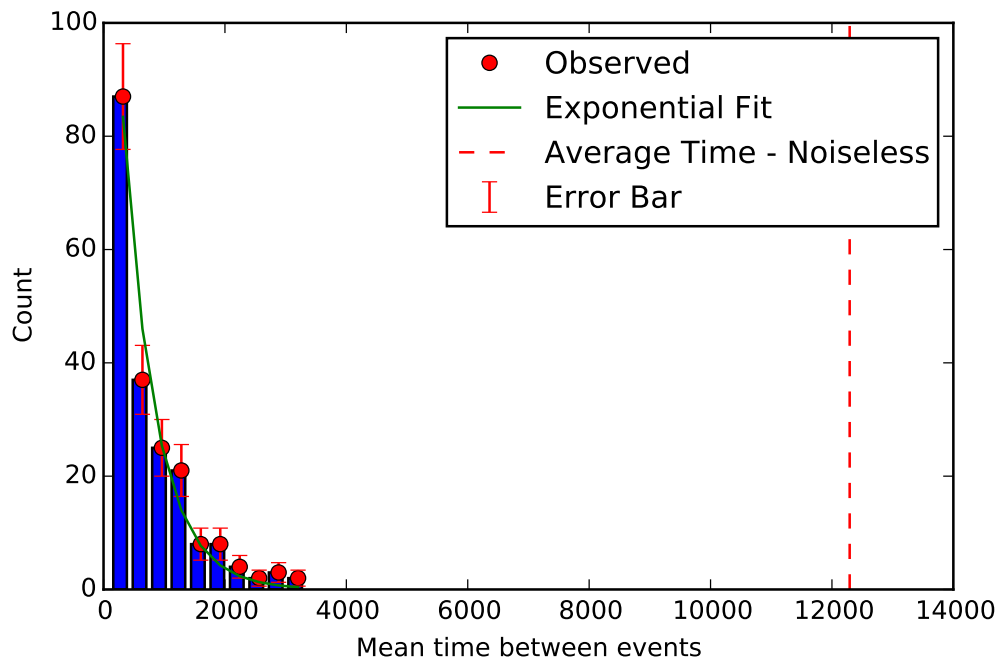


Figure 4.20: Poisson fit to mean-time between rogue waves. Small additive noise of the order of  $10^{-3}$  has been added to the  $E_{Real}$  at each integration step

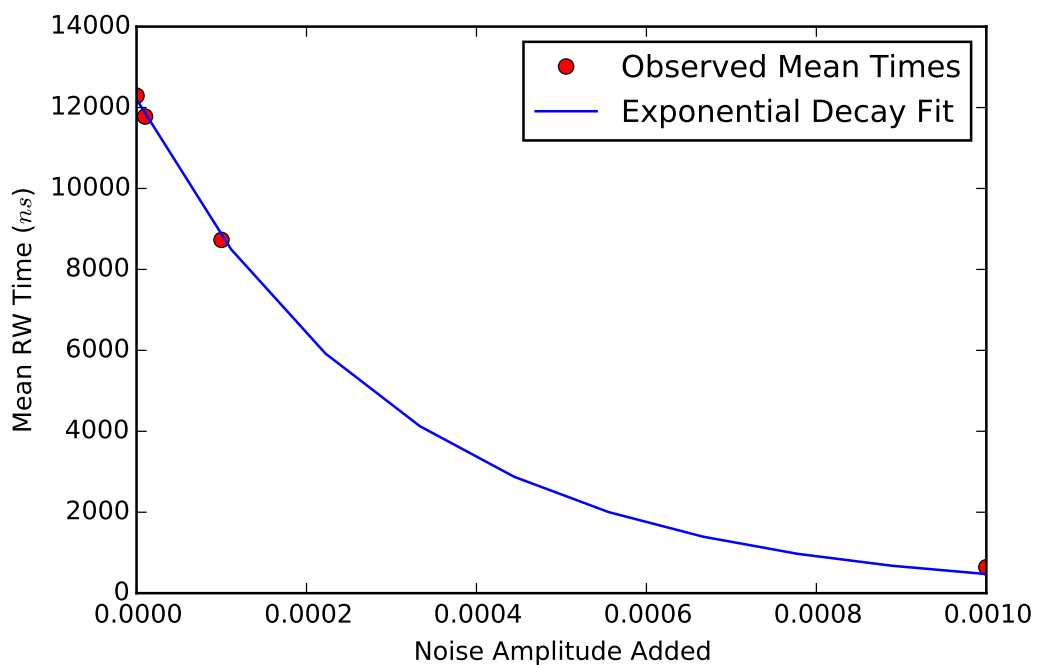


Figure 4.21: Mean-time between RW events versus noise

therefore to the threshold value as defined in Eq. (4.18).

## 4.11 Summary/Conclusion

The motivation for this work originally came from [8], where they claimed they had discovered an optical wave example of oceanography problem. As the semiconductor laser can be isolated from external noise reasonably well, exploring the origins of 'Rogue Wave' events could done without fear of experimental variation or contamination of results. This chapter has included several different approaches to understanding the RW events, including analysis of rates of change, a chimney-spike structure, Poincaré sections, Slow-manifold analysis, bifurcation diagrams and even numerical detection of an RW event in a two-mode laser.

The results from the above mentioned methodologies have confirmed several important properties of the events originally reported by [8, 72, 101]. That is, the rare, random and large amplitude nature of the optical events have been confirmed. The RW events have been shown to give less than  $2ns$  notice that (from a pure time-series approach) an RW event is about to occur. These results give merit to the title 'Rogue Wave'.

Additionally, several attempts at extending the knowledge surrounding RW events have been made in this chapter.

The chimney-spike structure, along with the saddle point perturbation have shown that singularity of the system allows a state where  $N$  grows abnormally large, which is a pivotal property of the system and without it the RW event would not be possible. The trajectories that are allowed to travel high enough in  $N$  for an RW event, all follow the trajectory towards the upper saddle, until they strike the spike-structure. However, uncovering how to get the system to follow the upper saddle point trajectory has not been fully uncovered and merits further investigation.

The existence of RW in two-mode lasers has not been fully explored but the results presented here show that the transition to a two mode RW is not trivial. Future work would entail parameter tuning (firstly in  $P$ ) to chaotic regions with larger visited  $|E|$  values. Other considerations for two-mode lasers would include the addition of noise as it has been repeatedly demonstrated that carefully chosen noise can enhance RW events in single-mode lasers.

While there may be RW events present in multi-mode devices, the single-mode lasers present the simplest device available to studying these phenomena. Future work for this area would involve further study of the saddle-point trajectory, up to where it becomes attractive or possibly intersects with the chaotic attractor which would explain the final piece of this puzzle.

# Chapter 5

## Conclusion

In this thesis we investigated the dynamical behaviour of single and two-mode lasers using optical injection. The main results of this work are the published results on the two-mode stability diagram - which is a first in several ways. Firstly, previous stability diagrams were generated for only single-mode lasers, and secondly, several areas of two-mode dynamics including two-mode locked, unlocked, and chaos were identified (as well as the single mode counter-parts) were captured in a single two-parameter mapping. In addition the transitions between two-mode and single-mode dynamics were also captured in a single unified view.

The detection of the two-mode equilibrium state (as positive detuning) is the first experimental verification of that region (to the best of the author's knowledge). Extraordinarily strong agreement is seen between the theoretical Lyapunov Exponents generated (from a simple, low-dimensional, rate-equation model) with the dynamical system mapping of the two-mode laser. The strength of this technique comes from the elegant experimental design where all of the optical data is captured for both lasing modes with a high sampling rate. The optical injection is controlled via a master laser and undergoes sinusoidal amplitude modulation and a portion of the modulated injected signal is directly recorded. Therefore we can quickly (less than 15min) sweep through a large frequency detuning where the main limitation to our results are the limitations of the apparatus used (such as the bandwidth of the photo-detector, time-resolution of the electrical spectrum analyser etc). From this data, simple yet crucial information of the state of the laser (two-mode/single-mode operation etc) can be extracted using easily accessible and well-understood quantities. From here, the mean, standard-deviation and FFT Spectra are used to generate a colour mapping for the different dynamical states present. The strength of this work is in the combination of theory and experiment and this unique perspective and understanding allowed for the results

to take form.

The technological impact of this dynamical mapping technique is far reaching. As well as being able to extend this technique to lasers with a higher number of lasing modes, it can also be used to characterise the dynamics of other types of optically injected lasers. Additionally this technique could be used to identify the location of desirable dynamics, or the transition between different desirable dynamics, such as all optical switching. It can also be used to characterise the complex dynamics from non-trivial devices such as Photonic Integrated Circuits(PIC), where output is desired behaviour requires extensive engineering.

As yet unpublished results from this thesis include the new insight into the origins of the RW phenomena. The introduction of the 'chimney-spike' structure allows for a greater understanding into this complex problem, highlighting a window through which a time-series can be guaranteed to generate a RW event, if the window is closely struck. Also additional time-series analysis and careful manifold analysis, while unsuccessful in explaining the true origin, highlight the contribution (if any) of the saddle points. Through this exploration, the importance of the singularity at the origin is highlighted. The singularity produces the 'spike' structure through which the abnormally large excursions are possible. Each of these new techniques came as a result of a thorough comparison and recreation of existing results in the area of optical RW. This includes a translation of the rate-equation model in [8] to the model used in this thesis. This was also in itself an important result as, although trivial it proved that we could expect to see RW events in our single-mode lasers which were previously thought to be well understood.

## 5.1 Future Work

Unavoidably in every thesis, the time comes when a line must be drawn between contributions that are to be included in the narrative and work that is left for future exploration. In this section I will list briefly some of the possible future applications and extensions to this thesis.

In the case of the dynamical system mappings, an obvious extension is to modify the colour mapping technique to include tori dynamics. This was left out (and marked as complex dynamics) due to the difficulty with automatically and robustly identifying secondary peaks that were located at precisely half the original frequency. This of course can be done by hand, but one of the goals is a fully automatic dynamical mapping process. Other extensions include the

improving the signal to noise ratio at very low  $K$ . This would allow for mapping the system stability for lower injection and experimental verification of the two-mode equilibrium region closing would be desirable as it is predicted numerically. In particular would allow comparison to [25] where they also detect observe experimentally the two-mode equilibrium regions.

In the case of the RW investigation, the true origins of these phenomena remain not completely understood. A complete mathematical statement describing the minimal requirements to create a RW event is desired. Presently the optically injected mode is the simplest known device (to the best of the author's knowledge) that displays the RW phenomena. Therefore presently the minimum known requirement is a three-dimensional autonomous system (chaos is required) with a singularity at the origin (this enables the 'spike' structure). Future work also should in could determining the presence of RW events in two-mode lasers as they are the next simplest device that meets the known requirements.

# **Appendices**

# **Appendix A**

## **Dynamical Classification of Optically Injected Lasers**

### **A.1 Additional Plots:Bi-stability Analysis**

Fig A.1 contains the numerical integration for Eq 2.98-2.100 without an additional random noise term. The system is initially in a state where both modes are non-zero, then a bi-stability is generated and the system moves to the single mode manifold but fails to switch back. The addition of the noise term in Fig 3.22 suggests that the single mode manifold is unstable at this region and requires a small perturbation (example: random spontaneous emission) to move the system away from the single mode manifold.

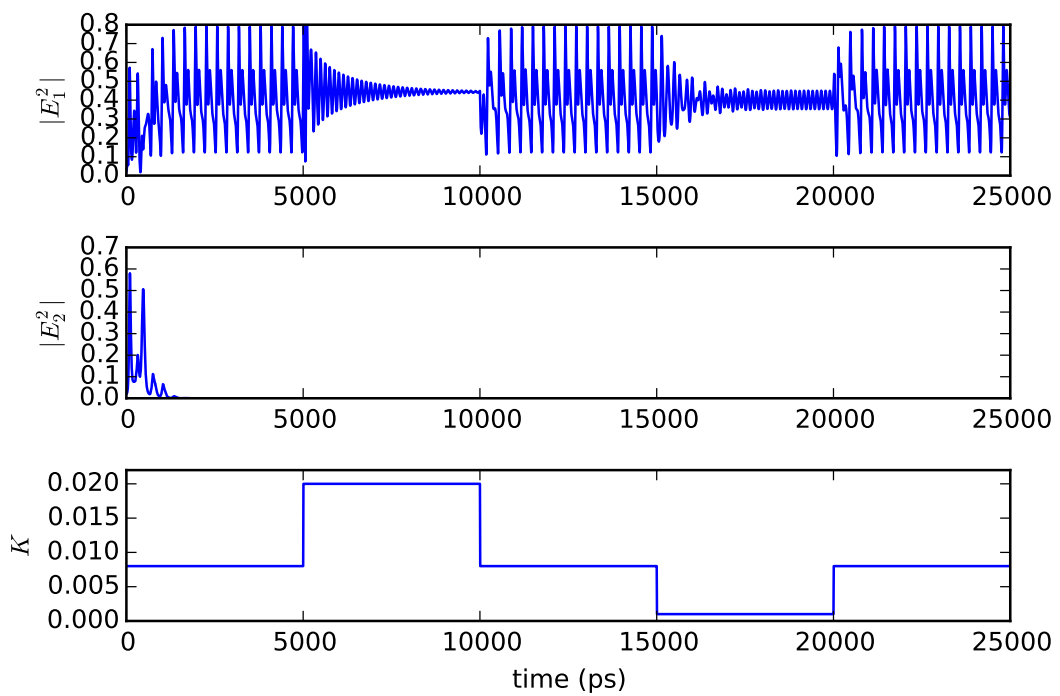


Figure A.1: No random noise for integration. Note that at 15000 ps the uninjected mode does not become non-zero.

# Appendix B

## Rogue Wave Analysis

### B.1 Source Code

#### B.1.1 RW Integrator.

```
#include <stdio.h>
#include <gsl/gsl_errno.h>
#include <gsl/gsl_matrix.h>
#include <gsl/gsl_odeiv2.h>
#include <math.h>

#define NDIM 3

typedef struct {
    double dt;
    double Tinv;
    double alpha;
    double P;
    double K;
    double Delta;
} param_type;

param_type param_default() {
    param_type p= {
        .dt = 0.01,
        .Tinv = 1/600.0,
        .alpha = 3.0,
        .P = 0.472,
```

```

        .K = 0.00913,
        .Delta = -0.005769,
    };
    return p;
}

int func (double t, const double y[], double f[], void *
params)
{
    param_type* p = (param_type *) params;

    double re=y[0], im=y[1], n=y[2];
    double tot = re*re + im*im;

    f[0]= n * (re - p->alpha * im) + p->Delta * im + p->K;
    f[1]= n * (im + p->alpha * re) - p->Delta * re;
    f[2]= p->Tinv * (p->P - n - ( (2. * n) + 1.) * tot);

    return GSL_SUCCESS;
}

double Esq(const double y[])
{
    return y[0]*y[0] + y[1]*y[1];
}

int jac (double t, const double y[], double *dfdy,double
dfdt[], void *params)
{
    param_type* p = (param_type *) params;

    double tot1 = Esq(y);

    double re = y[0];
    double im = y[1];
    double n = y[2];

    /* Jacobian matrix -> dfdy */

```

```

*(dfdy + 0 *NDIM+ 0) = n;
*(dfdy + 0 *NDIM+ 1) = -n*(p->alpha) + p->Delta;
*(dfdy + 0 *NDIM+ 2) = -(re - im*p->alpha);

*(dfdy + 1 *NDIM+ 0) = n*p->alpha - p->Delta;
*(dfdy + 1 *NDIM+ 1) = n;
*(dfdy + 1 *NDIM+ 2) = im + re*p->alpha;

*(dfdy + 2 *NDIM+ 0) = p->Tinv*(0+0-(2*n+1)*(2*re));
*(dfdy + 2 *NDIM+ 1) = p->Tinv*(0+0-(2*n+1)*(2*im));
*(dfdy + 2 *NDIM+ 2) = p->Tinv*(0-1-((2*1) + 0)*tot1);

/* df/dt */
dfdt[0] = 0.0;
dfdt[1] = 0.0;
dfdt[2] = 0.0;

return GSL_SUCCESS;
}

void jacobian_of_laser(double const y[], double DF[NDIM][
    NDIM], param_type p){
double dfdt[NDIM];
double dfdy[NDIM*NDIM];

jac (0.0, y, dfdy, dfdt , (void *) &p);

for (int k =0; k<NDIM; k++) {
    for (int l =0; l<NDIM; l++) {
        DF[k][l] = dfdy[k*NDIM +l];
    }
}

long long find_fdot(double y[], double dxdt_out[], double
rw_th, long long Nt, param_type p) {

    const gsl_odeiv2_step_type * T = gsl_odeiv2_step_rkf45;
    gsl_odeiv2_step * s = gsl_odeiv2_step_alloc (T, NDIM);
}
}

```

```

gsl_odeiv2_system sys = {func, jac, NDIM, (void *) &p};

//Save deriv calcs from previous iter to try and save
//run time...
double dxdt_in[NDIM];

double y_err[NDIM];

long long i;

//Initialise system for current params.....
GSL_ODEIV_FN_EVAL(&sys, 0.0, y, dxdt_in);

for (i =0; (!rw_th || Esq(y) < rw_th) && (!Nt || i< Nt)
; i++) {
    double t = i * p.dt;
    int status = gsl_odeiv2_step_apply (s, t, p.dt, y,
        y_err, dxdt_in, dxdt_out, &sys);

    if (status != GSL_SUCCESS) {
        printf ("error, return value=%d\n", status);
        break;
    }
}
gsl_odeiv2_step_free (s);

//return final estimate of dxdt_out
/* return dxdt_out; */
return i;
}

long long find_rw_chimney(double y[], double rw_th, long
    long Nt, param_type p, int *go_in_chimney, int *
    go_out_chimney, const gsl_odeiv2_step_type *gstype){
    gsl_odeiv2_step * s = gsl_odeiv2_step_alloc (gstype,
        NDIM);
    gsl_odeiv2_system sys = {func, NULL, NDIM, (void *) &p};
}

```

```

//Save deriv calcs from previous iter to try and save run
//time...
double dxdt_in[NDIM], dxdt_out[NDIM];

double y_err[NDIM];

long long i;

*go_in_chimney = 0;
*go_out_chimney = 0;

//Initialise system for current params.....
GSL_ODEIV_FN_EVAL(&sys, 0.0, y, dxdt_in);
int ndot_is_positive = (dxdt_in[NDIM-1] > 0);
//printf("ndot_is_positive %d\n", ndot_is_positive );

for (i =0; (!rw_th || Esq(y) < rw_th) && (!Nt || i< Nt) ;
     i++) {
    double t = i * p.dt;
    int status = gsl_odeiv2_step_apply (s, t, p.dt, y,
                                       y_err, dxdt_in, dxdt_out, &sys);
    if (ndot_is_positive && (dxdt_out[NDIM-1] < 0) ) {
        (*go_out_chimney)++;
        ndot_is_positive = 0;
    } else if (!ndot_is_positive && (dxdt_out[NDIM-1] > 0)
               ) {
        (*go_in_chimney)++;
        ndot_is_positive = 1;
    }
    if (status != GSL_SUCCESS) {
        printf ("error, return value=%d\n", status);
        break;
    }
    for (int j = 0; j<NDIM; j++) {
        dxdt_in[j] = dxdt_out[j];
    }
}
gsl_odeiv2_step_free (s);
return i;
}

```

```

long long find_rw(double y[], double rw_th, long long Nt,
param_type p) {
    int go_in_chimney = 0, go_out_chimney=0;
    return find_rw_chimney(y, rw_th, Nt, p, &
        go_in_chimney, &go_out_chimney,
        gsl_odeiv2_step_rkf45);
}

long long stiff_solver(double y[], long long Nt, param_type
p) {
/* gsl_odeiv2_step * s = gsl_odeiv2_step_alloc (gstype,
   NDIM); */
double epsabs = 1.0e-6;
double epsrel = 0.0;
gsl_odeiv2_system sys = {func, jac, NDIM, (void *) &p};
gsl_odeiv2_driver * d = gsl_odeiv2_driver_alloc_y_new (&
    sys, gsl_odeiv2_step_rk4imp, p.dt, epsabs, epsrel);

double t=0.0;
double t_end = Nt*p.dt;

int status = gsl_odeiv2_driver_apply (d, &t, t_end, y);

if (status != GSL_SUCCESS) {
    printf ("error, return value=%d\n", status);
}

//printf ("####E %.5e %.5e %.5e\n", t, y[0], y[1]);

gsl_odeiv2_driver_free (d);
return 0;
}

int main (int argc, char** argv)
{
    double y[] = { 0.1, 0.1, -0.0001 };
    double y1 []= { 0.1, 0.1, -0.0001 };
}

```

```

param_type p = param_default();
p.dt = -0.1;

printf("yold\n");

printf("%25.17e %25.17e %25.17e\n", y[0], y[1], y[2]);
for(int i=0; i<10; i++){
    find_rw(y1, 0.0, 1, p);
    printf("%s", "yold");
    printf("%25.17e %25.17e %25.17e\n", y1[0], y1
        [1], y1[2]);
}

for(int i=0; i<10; i++){
    stiff_solver(y, 1, p);
    printf("%s", "ynew");
    printf("%25.17e %25.17e %25.17e\n", y[0], y
        [1], y[2]);
}

//Test Jacobian
/* double DF[NDIM][NDIM]; */
/* jacobian_of_laser(y,DF,p); */
/* printf("Jacobian\n"); */
/* for(int i=0;i<NDIM;i++){ */
/*     for(int j=0;j<NDIM;j++){ */
/*         printf("%lf \n",DF[i][j]); */
/*     } */
/* } */

/* printf("Jac\n"); */
/* double dfdy[NDIM*NDIM]; */
/* double dfdt[NDIM]; */
/* jac(0.0,y,dfdy,dfdt,(void *) &p); */

/* for(int it=0; it<NDIM*NDIM; it++){ */
/*     printf("jac: %f\n", dfdy[it]); */
/* } */

```

```

    exit(0);
}

```

## B.2 Python Code

### B.2.1 do\_process\_data.py

```

import pandas as pd
import matplotlib.pyplot as plt
import numpy as np
import sys
import os
import time
import matplotlib as mpl

#####
# Globals
gamma0 = 9.8e11
GHz = 2.0*np.pi*1.0e9/gamma0
ns = 1.0/(gamma0/1.0e9)

fig_ext = '.png'
dir1 = './data/'
#####

#####
# Colour plot
cmap = plt.cm.jet
cmaplist = [cmap(i) for i in range(cmap.N)]

# force the first color entry to be grey
cmaplist[0] = (.5,.5,.5,1.0)
cmap = cmap.from_list('Custom cmap', cmaplist, cmap.N)

# define the bins and normalize
bounds = np.linspace(-1,5,7)
norm = mpl.colors.BoundaryNorm(bounds, cmap.N)
#####

#####

```

```

#Functions

def make_hist(data,b_num=50):
    hist, bins = np.histogram(data, b_num)
    width = 0.7 * (bins[1] - bins[0])
    center = (bins[:-1] + bins[1:]) / 2
    return hist, bins, width,center

def examine_data(data_temp,b_num):
    #This considers only local max/min and the histograms
    #looks more like the experiment
    d1 = data_temp[data_temp.index[1:-1]][(data_temp[
        data_temp.index[1:-1]] > data_temp[data_temp.index
        [-2]]) * (data_temp[data_temp.index[1:-1]] >
        data_temp[data_temp.index[2:]])]

    #Make histogram
    hist,bins, width,center = make_hist(d1)

    # Define the limit for Rogue Waves
    limit = d1.mean() + 8.0*d1.std()

    return d1,hist,bins,width,center,limit

def make_and_save_plot(file_name1,cols,b_num=50,iflog=False):
    num_cols = len(cols)

    # Read data from file
    dataset = pd.read_csv(file_name1,delimiter=r"\s+")

    #Create image plot
    im1 = plt.figure()
    im1.subplots_adjust(wspace=0.27, hspace=0.27, left=0.12,
                        right=0.9, top=0.9, bottom=0.1)

    for (j,col1) in zip(range(1,len(cols)+1),cols):

```

```

#Get column data
data_temp = dataset[col1]

#get histogram data and RW limit
d1,hist,bins,width,center,limit = examine_data(
    data_temp,b_num)

a1 = im1.add_subplot(2,num_cols,num_cols+j)
b1 = im1.add_subplot(2,num_cols,j)

a1.locator_params(nbins=5)
b1.locator_params(nbins=5)

#Make quick plot of histogram
if(iflog==False):
    a1.bar(center, hist, width=width);
    a1.set_ylabel(col1)
else:
    a1.bar(center, np.log(hist), width=width);
    a1.set_ylabel("log("+col1+")")

a1.axvline(limit, ymin=0.0, ymax = 2.0, linewidth
=2, color='r',ls='dashed')
a1.set_xlabel("Power (arb units)")
a1.ticklabel_format(style='sci', axis='y',
scilimits=(0,0))
a1.set_ylim(0,0.2*10)

b1.plot(data_temp.index*ns,data_temp);
b1.plot(d1.index*ns,d1,'r+');
b1.set_xlabel("ns");

#Save the file next to .dat
plot_file1 = os.path.splitext(file_name1)[0]+fig_ext
print "Saving to "+plot_file1
im1.savefig(plot_file1)
print "File saved"
# im1.show()
# plt.close(im1) #Closes figure when done...

```

```

def get_all_names(directory, decision='new'):
    file_paths = []
    for root, directories, files in os.walk(directory):
        for filename in files:
            #Join strings to get full path
            filepath = os.path.join(root, filename)
            file_ext = os.path.splitext(filepath)[-1]
            fig_name = os.path.splitext(filepath)[0]

            if (file_ext == '.dat'): #Only look at .dat
                files
                file_paths.append(filepath) #Add to the
                list

    return file_paths

#####
# find_array_value(data_array,value=-np.pi/4.0,
# value_error=0.9):
#     diff_in_data = (data_array-value)
#     signs = np.sign(diff_in_data)
#     #temp_val2 = signs.index[(signs[signs.index[0]:signs.
#         index[-2]]!=signs[signs.index[1]:signs.index[-1]])*(
#             signs[signs.index[0]:signs.index[-2]]== -1)*(

#             diff_in_E []<=phase_error)]


#Condition 1: difference passes through zero...
condition1 = (signs[signs.index[0]:signs.index[-2]]!=
    signs[signs.index[1]:signs.index[-1]])

#Condition 2: sign of i ==+1, sign of i+1 ==-1 (ignoring other way it can pass through zero
condition2 = (signs[signs.index[0]:signs.index
    [-2]]== -1)

#Condition 3: Discontinuities can be flagged as false

```

```

    poisitives!
condition3 = (np.abs(data_array[data_array.index[0]:data_array.index[-2]]-value)<=value_error)

vals = condition1*condition2*condition3
return data_array.index[vals]

def examine_and_count(data,phase_val=(-np.pi/4.0)):
    #Take sqrt to get modulus of E2..
    d_temp = np.sqrt(data["E2"])

    #find largest peak and assume there is at most one RW (
    #short time traces...)
    peak_index = d_temp.argmax()

#    d1,hist,bins,width,center,limit = examine_data(d_temp,
#b_num=50)
#    limit = np.sqrt(3.4) #from longer traces

    #check number of RW peaks..see if peak bigger than
    #limit...
    rws_vals = [i for i in range(len(bins)-1) if bins[i] >
    limit and hist[i]>0]
    rws = hist[rws_vals].sum()

    #look at phase
    temp_ph = np.arctan2(data["y[2]"],data["y[1]"])

    temp_val2 = find_array_value(temp_ph,value=-np.pi/4.0,
        value_error=0.9)

    #count only phases before rogue wave occurs..
    important_points = [x for x in temp_val2 if x <
    peak_index]

    #return [{rogue waves info},{phase==pi/4}]
    return [[rws,rws_vals,hist,bins,limit,peak_index],[important_points,temp_ph]]

def quick_examine_and_count(data,phase_val=(-np.pi/4.0)):
```

```

#Take sqrt to get modulus of E2..
d_temp = np.sqrt(data["E2"])

#find largest peak and assume there is at most one RW (
#short time traces...)
peak_index = d_temp.argmax()

limit = np.sqrt(3.4) #from longer traces

if d_temp[peak_index]<limit:
    return -1


#look at phase
temp_ph = np.arctan2(data["y[2]"][0:peak_index],data["y[1]"][0:peak_index])

important_points = find_array_value(temp_ph,value=-np.pi/4.0,value_error=0.9)
return len(important_points)


def find_local_max(data_temp):
#    #bigger than next point...
    b1 = data_temp[data_temp.index[1:-1]] > data_temp[
        data_temp.index[:-2]]

    #bigger than last point...
    b2 = data_temp[data_temp.index[1:-1]] > data_temp[
        data_temp.index[2:]]

    #pandas cannot handle numexpr, must handle arrays like
    #this...
    max_locs = b1.values*b2.values

    #return index of local max
    max_pts = data_temp.index[1:-1][max_locs]

    #incase there is no local max...
    if len(max_pts)==0:

```

```

        #take last coord
        max_pts = data_temp.index[1:-1][-1]

        return max_pts

def examine_data2(data_temp,limit):
    #find largest peak and assume there is at most one RW (
    #short time traces...)
    peak_index = data_temp.argmax()
    if data_temp[peak_index]<limit:
        #No rogue wave
        return -1

    #only need to look as far as the rogue wave
    max_pts_E = find_local_max(data_temp[data_temp.index[0:
        peak_index]])
    return len(max_pts_E)

#####
#Main
if __name__ == "__main__":
    len_args = len(sys.argv)
    list_args = sys.argv

    cols = ["E2"]

    print 'Number of arguments:', len_args , 'arguments.'
    print 'Argument List:', list_args

#Decide which timetraces to look at:
if (len(sys.argv) == 2):
    file_name1 = list_args[1]

    if file_name1 == "all":
        print "do all"
        decision = file_name1
        list_of_files = get_all_names(dir1,decision)

```

```

        elif file_name1 == "new":
            print "do new"
            decision = file_name1
            list_of_files = get_all_names(dir1,decision)
        else:
            "Reading file: "+file_name1
            list_of_files = [file_name1]

    elif (len(sys.argv) >= 2):
        print "do list"
        list_of_files = sys.argv[1:-1]

    else:
        file_name1 = 'data/0.4/timetrace_0.00913_0.dat'
        print "No file name passed. Using "+file_name1+"\n"

    for trace in list_of_files:
        print trace
        make_and_save_plot(trace,cols,b_num=50,iflog=True)

#make_and_save_plot(file_name1,cols,b_num=50,iflog=
#                    False)

#####

```

### B.3 Relation between $\Delta\omega$ and $\Delta\nu$

$$\Delta\omega_{CB} = \Delta\nu 2\pi \quad (B.1)$$

$$\Delta\omega = \frac{\Delta\omega_{CB}}{2\kappa} \quad (B.2)$$

$$\Delta\omega = \frac{\Delta\nu 2\pi}{2\kappa} \quad (B.3)$$

In Eq. B.3, the subscript  $CB$  refers to the definition of the dimensionless detuning from [8].  $\Delta\nu$  is the laser frequency, and  $\Delta\omega$  is the dimensionless detuning used predominately in this thesis.

# References

- [1] G. P. Agrawal, N. K. Dutta, and G. P. Agrawal. *Semiconductor lasers*. Van Nostrand Reinhold, New York, 1993.
- [2] J. Ahuja, D. B. Nalawade, J. Zamora-Munt, R. Vilaseca, and C. Masoller. Rogue waves in injected semiconductor lasers with current modulation: role of the modulation phase. *Optics Express*, 22(23):28377–28382, 2014.
- [3] N. Akhmediev, A. Ankiewicz, and M. Taki. Waves that appear from nowhere and disappear without a trace. *Physics Letters A*, 373(6):675 – 678, 2009.
- [4] N. Akhmediev, J. M. Dudley, D. R. Solli, and S. K. Turitsyn. Recent progress in investigating optical rogue waves. *Journal of Optics*, 15(6):060201, 2013.
- [5] J. Allen and L. Rabiner. A unified approach to short-time Fourier analysis and synthesis. *Proceedings of the IEEE*, 65(11):1558–1564, Nov 1977.
- [6] F. T. Arecchi, R. Meucci, G. Puccioni, and J. Tredicce. Experimental evidence of subharmonic bifurcations, multistability, and turbulence in a  $q$ -switched gas laser. *Phys. Rev. Lett.*, 49:1217–1220, Oct 1982.
- [7] R. B. Blackman and J. W. Tukey. The measurement of power spectra from the point of view of communications engineering — part i. *Bell System Technical Journal*, 37(1):185–282, 1958.
- [8] C. Bonatto, M. Feyereisen, S. Barland, M. Giudici, C. Masoller, J. R. R. Leite, and J. R. Tredicce. Deterministic optical rogue waves. *Phys. Rev. Lett.*, 107:053901, Jul 2011.
- [9] C. M. Bowden and G. P. Agrawal. Maxwell-bloch formulation for semiconductors: Effects of coherent coulomb exchange. *Phys. Rev. A*, 51:4132–4139, May 1995.

- [10] N. Brandonisio. *Dynamics of dual-mode semiconductor lasers with current modulation and delayed optical feedback*. PhD thesis, Department of Physics, National University Of Ireland, Cork., 2011.
- [11] N. Brandonisio, P. Heinricht, S. Osborne, A. Amann, and S. O'Brien. Bistability and all-optical memory in dual-mode diode lasers with time-delayed optical feedback. *Photonics Journal, IEEE*, 4(1):95–103, Feb 2012.
- [12] H. J. Caulfield and S. Dolev. Why future supercomputing requires optics. *Nat Photon*, 4(5):261–263, May 2010.
- [13] H. Chen and J. Liu. Open-loop chaotic synchronization of injection-locked semiconductor lasers with gigahertz range modulation. *Quantum Electronics, IEEE Journal of*, 36(1):27–34, Jan 2000.
- [14] W. Chow. Theory of line narrowing and frequency selection in an injection locked laser. *Quantum Electronics, IEEE Journal of*, 19(2):243–249, Feb 1983.
- [15] W. Chow, G. C. Dente, and D. Depatie. Saturation effects in semiconductor lasers. *Quantum Electronics, IEEE Journal of*, 23(8):1314–1320, Aug 1987.
- [16] W. W. Chow and S. W. Koch. *Semiconductor-laser fundamentals : physics of the gain materials*. Springer, Berlin; New York, 1999.
- [17] W. Cochran, J. W. Cooley, D. Favin, H. Helms, R. Kaenel, W. Lang, J. Maling, G.C., D. Nelson, C. Rader, and P. D. Welch. What is the fast Fourier transform? *Proceedings of the IEEE*, 55(10):1664–1674, Oct 1967.
- [18] A. Einstein. Zur Quantentheorie der Strahlung. *Physikalische Zeitschrift*, 18:121–128, 1917.
- [19] L. Enochson and R. Otnes. *Programming and Analysis for Digital Time Series Data*. Number v. 3 in Programming and Analysis for Digital Time Series Data. Shock and Vibration Information Center, 1969.
- [20] S. Eriksson. Dependence of the experimental stability diagram of an optically injected semiconductor laser on the laser current. *Optics communications*, 210(3):343–353, 2002.
- [21] S. Eriksson and Å. M. Lindberg. Observations on the dynamics of semiconductor lasers subjected to external optical injection. *Journal of Optics B: Quantum and Semiclassical Optics*, 4(2):149, 2002.

- [22] R. P. Feynman, R. B. Leighton, and M. L. Sands. *The Feynman lectures on physics*. Addison-Wesley Pub. Co., Reading, Mass., 1963.
- [23] D. Fitsios, K. Vyrskinos, A. Miliou, and N. Pleros. Memory speed analysis of optical ram and optical flip-flop circuits based on coupled SOA-MZI gates. *Selected Topics in Quantum Electronics, IEEE Journal of*, 18(2):1006–1015, March 2012.
- [24] A. G. Fox and T. Li. Resonant modes in a maser interferometer. *Bell System Technical Journal*, 40(2):453–488, 1961.
- [25] G. Friart, A. Gavrielides, and T. Erneux. Analytical stability boundaries of an injected two-polarization semiconductor laser. *Phys. Rev. E*, 91:042918, Apr 2015.
- [26] F. Friederich, G. Schuricht, A. Deninger, F. Lison, G. Spickermann, P. H. Bolívar, and H. G. Roskos. Phase-locking of the beat signal of two distributed-feedback diode lasers to oscillators working in the MHz to THz range. *Opt. Express*, 18(8):8621–8629, Apr 2010.
- [27] A. N. Ganshin, V. B. Efimov, G. V. Kolmakov, L. P. Mezhov-Deglin, and P. V. E. McClintock. Observation of an inverse energy cascade in developed acoustic turbulence in superfluid helium. *Phys. Rev. Lett.*, 101:065303, Aug 2008.
- [28] A. N. Ganshin, V. B. Efimov, G. V. Kolmakov, L. P. Mezhov-Deglin, and P. V. E. McClintock. Observation of an inverse energy cascade in developed acoustic turbulence in superfluid helium. *Phys. Rev. Lett.*, 101:065303, Aug 2008.
- [29] I. Gatare, M. Sciamanna, J. Buesa, H. Thienpont, and K. Panajotov. Nonlinear dynamics accompanying polarization switching in vertical-cavity surface-emitting lasers with orthogonal optical injection. *Appl. Phys. Lett.*, 88(10):101106, Mar 2006.
- [30] I. Gatare, M. Sciamanna, M. Nizette, H. Thienpont, and K. Panajotov. Mapping of two-polarization-mode dynamics in vertical-cavity surface-emitting lasers with optical injection. *Physical Review E*, 80(2):026218, 2009.
- [31] E. Gordon. Mode selection in GaAs injection lasers resulting from Fresnel reflection. *Quantum Electronics, IEEE Journal of*, 9(7):772–776, Jul 1973.

- [32] J. P. Gordon, H. J. Zeiger, and C. H. Townes. Molecular microwave oscillator and new hyperfine structure in the microwave spectrum of nh<sub>3</sub>. *Physical Review*, 95(1):282–284, 1954.
- [33] S. Gringeri, B. Basch, V. Shukla, R. Egorov, and T. Xia. Flexible architectures for optical transport nodes and networks. *Communications Magazine, IEEE*, 48(7):40–50, July 2010.
- [34] H. Haken. Analogy between higher instabilities in fluids and lasers. *Physics Letters A*, 53(1):77 – 78, 1975.
- [35] F. Harris. On the use of windows for harmonic analysis with the Discrete Fourier Transform. *Proceedings of the IEEE*, 66(1):51–83, Jan 1978.
- [36] P. Heinricht, B. Wetzel, S. OBrien, A. Amann, and S. Osborne. Bistability in an injection locked two color laser with dual injection. *Applied Physics Letters*, 99(1):011104–011104, 2011.
- [37] R. Höhmann, U. Kuhl, H.-J. Stöckmann, L. Kaplan, and E. J. Heller. Freak waves in the linear regime: A microwave study. *Phys. Rev. Lett.*, 104:093901, Mar 2010.
- [38] IEEE Computer Society. IEEE standard for floating-point arithmetic. *IEEE Std 754-2008*, pages 1–70, Aug 2008.
- [39] A. Javan, W. R. Bennett, and D. R. Herriott. Population inversion and continuous optical maser oscillation in a gas discharge containing a he-ne mixture. *Phys. Rev. Lett.*, 6:106–110, Feb 1961.
- [40] H. Kawaguchi. Bistable laser diodes and their applications: state of the art. *Selected Topics in Quantum Electronics, IEEE Journal of*, 3(5):1254–1270, 1997.
- [41] H. Kawaguchi, K. Inoue, T. Matsuoka, and K. Otsuka. Bistable output characteristics in semiconductor laser injection locking. *Quantum Electronics, IEEE Journal of*, 21(9):1314–1317, Sep 1985.
- [42] C. Kharif, E. N. Pelinovskii, and A. Slunyaev. *Rogue waves in the ocean*. Springer, Berlin, 2009.
- [43] N. Kim, J. Shin, E. Sim, C. W. Lee, D.-S. Yee, M. Y. Jeon, Y. Jang, and K. H. Park. Monolithic dual-mode distributed feedback semiconduc-

- tor laser for tunable continuous-wave terahertz generation. *Opt. Express*, 17(16):13851–13859, Aug 2009.
- [44] B. Krauskopf, S. Wieczorek, and D. Lenstra. Different types of chaos in an optically injected semiconductor laser. *Applied Physics Letters*, 77(11):1611–1613, 2000.
- [45] R. D. L. Kronig. On the theory of dispersion of x-rays. *J. Opt. Soc. Am.*, 12(6):547–556, Jun 1926.
- [46] M. M. Krstic, J. V. Crnjanski, M. L. Masanovic, L. A. Johansson, L. A. Coldren, and D. M. Gvozdic. Multivalued stability map of an injection-locked semiconductor laser. *Selected Topics in Quantum Electronics, IEEE Journal of*, 19(4):1501408–1501408, 2013.
- [47] H. K. . R. Ladenburg. Experimental proof of ‘negative dispersion.’. *Nature*, 122:438–439, 1928.
- [48] W. E. Lamb. Theory of an optical maser. *Phys. Rev.*, 134:A1429–A1450, Jun 1964.
- [49] R. Lang. Injection locking properties of a semiconductor laser. *Quantum Electronics, IEEE Journal of*, 18(6):976–983, Jun 1982.
- [50] C.-F. Lin and P.-C. Ku. Analysis of stability in two-mode laser systems. *Quantum Electronics, IEEE Journal of*, 32(8):1377–1382, Aug 1996.
- [51] M. Lindberg and S. W. Koch. Effective bloch equations for semiconductors. *Phys. Rev. B*, 38:3342–3350, Aug 1988.
- [52] L. Liu, R. Kumar, K. Huybrechts, T. Spuesens, G. Roelkens, E.-J. Geluk, T. de Vries, P. Regreny, D. Van Thourhout, R. Baets, and G. Morthier. An ultra-small, low-power, all-optical flip-flop memory on a silicon chip. *Nat Photon*, 4(3):182–187, Mar. 2010.
- [53] E. N. Lorenz. Atmospheric models as dynamical systems. *Perspectives in Nonlinear Dynamics*, pages 1–17, 1986.
- [54] T. H. Maiman. Stimulated optical radiation in ruby. *Nature*, 187(4736):493–494, Aug. 1960.
- [55] P. Mandel. *Theoretical Problems in Cavity Nonlinear Optics*. Cambridge University Press, 1997. Cambridge Books Online.

- [56] K. A. McIntosh, E. R. Brown, K. B. Nichols, O. B. McMahon, W. F. DiNatale, and T. M. Lyszczarz. Terahertz photomixing with diode lasers in low-temperature-grown GaAs. *Applied Physics Letters*, 67(26):3844–3846, 1995.
- [57] C. R. Mirasso, P. Colet, and P. García-Fernández. Synchronization of chaotic semiconductor lasers: Application to encoded communications. *Phot. Tech. Lett.*, 8:299–301, 1996.
- [58] C. Ning, R. Indik, and J. Moloney. Effective bloch equations for semiconductor lasers and amplifiers. *Quantum Electronics, IEEE Journal of*, 33(9):1543–1550, Sep 1997.
- [59] S. O 'Brien, A. Amann, R. Fehse, S. Osborne, E. P. O'Reilly, and J. M. Rondinelli. Spectral manipulation in Fabry-Perot lasers: perturbative inverse scattering approach. *J. Opt. Soc. Am. B*, 23(6):1046–1056, 2006.
- [60] S. O 'Brien, S. Osborne, D. Bitauld, N. Brandonisio, A. Amann, R. Phelan, B. Kelly, and J. O'Gorman. Optical synthesis of terahertz and millimeter-wave frequencies with discrete mode diode lasers. *Microwave Theory and Techniques, IEEE Transactions on*, 58(11):3083–3087, 2010.
- [61] S. O'Brien, S. Osborne, K. Buckley, R. Fehse, A. Amann, E. P. O'Reilly, L. P. Barry, P. Anandarajah, J. Patchell, and J. O'Gorman. Inverse scattering approach to multiwavelength fabry-pérot laser design. *Phys. Rev. A*, 74:063814, Dec 2006.
- [62] S. Ogita, A. J. Lowery, and R. S. Tucker. Influence of asymmetric nonlinear gain on the transient intensities of longitudinal modes in long wavelength fabry-perot laser diodes. *IEEE journal of quantum electronics*, 33(2):198–210, 1997.
- [63] S. Osborne, A. Amann, D. Bitauld, and S. O'Brien. On-off intermittency in an optically injected semiconductor laser. *Phys. Rev. E*, 85:056204, May 2012.
- [64] S. Osborne, A. Amann, K. Buckley, G. Ryan, S. Hegarty, G. Huyet, and S. O 'Brien. Antiphase dynamics in a multimode semiconductor laser with optical injection. *Physical Review A*, 79(2):023834, 2009.
- [65] S. Osborne, A. Amann, and S. O'Brien. Multimode dynamics in a semiconductor laser with optical injection. In *Lasers and Electro-Optics 2009*

and the European Quantum Electronics Conference. CLEO Europe - EQEC 2009. European Conference on, pages 1–1, June 2009.

- [66] S. Osborne, K. Buckley, A. Amann, and S. O'Brien. All-optical memory based on the injection locking bistability of a two-color laser diode. *Opt. Express*, 17(8):6293–6300, Apr 2009.
- [67] S. Osborne, P. Heinricht, N. Brandonisio, A. Amann, and S. O'Brien. Wavelength switching dynamics of two-colour semiconductor lasers with optical injection and feedback. *Semiconductor Science and Technology*, 27(9):094001, 2012.
- [68] D. O'Shea, S. Osborne, N. Blackbeard, D. Goulding, B. Kelleher, and A. Amann. Experimental classification of dynamical regimes in optically injected lasers. *Opt. Express*, 22(18):21701–21710, Sep 2014.
- [69] G. I. Papadimitriou, C. Papazoglou, and A. S. Pomportsis. Optical switching: switch fabrics, techniques, and architectures. *Lightwave Technology, Journal of*, 21(2):384–405, Feb 2003.
- [70] I. Park, I. Fischer, and W. Elsäßer. Highly nondegenerate four-wave mixing in a tunable dual-mode semiconductor laser. *Applied Physics Letters*, 84(25):5189–5191, 2004.
- [71] M. A. Parker. *Physics of optoelectronics*. Taylor & Francis, Boca Raton, FL, 2005.
- [72] S. Perrone, R. Vilaseca, J. Zamora-Munt, and C. Masoller. Controlling the likelihood of rogue waves in an optically injected semiconductor laser via direct current modulation. *Phys. Rev. A*, 89:033804, Mar 2014.
- [73] F. Ramos, E. Kehayas, J. M. Martinez, R. Clavero, J. Martí, L. Stamopoulos, D. Tsiokos, H. Avramopoulos, J. Zhang, P. V. Holm-Nielsen, N. Chi, P. Jeppesen, N. Yan, I. T. Monroy, A. M. J. Koonen, M. T. Hill, Y. Liu, H. J. S. Dorren, R. V. Caenegem, D. Colle, M. Pickavet, and B. R. ti. IST-LASAGNE: Towards all-optical label swapping employing optical logic gates and optical flip-flops. *J. Lightwave Technol.*, 23(10):2993, Oct 2005.
- [74] V. Ruban, Y. Kodama, M. Ruderman, J. Dudley, R. Grimshaw, P. McClintonck, M. Onorato, C. Kharif, E. Pelinovsky, T. Soomere, G. Lindgren, N. Akhmediev, A. Slunyaev, D. Solli, C. Ropers, B. Jalali, F. Dias, and

- A. Osborne. Rogue waves 2013 towards a unifying concept?: Discussions and debates. *The European Physical Journal Special Topics*, 185(1):5–15, 2010.
- [75] M. Sargent, M. O. Scully, and W. E. Lamb. *Laser physics*. Addison-Wesley Pub. Co., Advanced Book Program, Reading, Mass., 1974.
- [76] A. L. Schawlow and C. H. Townes. Infrared and optical masers. *Phys. Rev.*, 112:1940–1949, Dec 1958.
- [77] H. G. Schuster and K. Lüdge. *Nonlinear laser dynamics: from quantum dots to cryptography*. John Wiley & Sons, 2012.
- [78] M. Shats, H. Punzmann, and H. Xia. Capillary rogue waves. *Phys. Rev. Lett.*, 104:104503, Mar 2010.
- [79] T. Simpson. Mapping the nonlinear dynamics of a distributed feedback semiconductor laser subject to external optical injection. *Optics Communications*, 215(1–3):135–151, 2003.
- [80] P. Smith. Mode selection in lasers. *Proceedings of the IEEE*, 60(4):422–440, 1972.
- [81] H. G. Solari and G.-L. Oppo. Laser with injected signal: perturbation of an invariant circle. *Optics Communications*, 111(1):173 – 190, 1994.
- [82] D. R. Solli, C. Ropers, P. Koonath, and B. Jalali. Optical rogue waves. *Nature*, 450(7172):1054–1057, dec 2007. 10.1038/nature06402.
- [83] R. Steele. Optical phase-locked loop using semiconductor laser diodes. *Electronics Letters*, 19:69–71(2), January 1983.
- [84] S. Strogatz. *Nonlinear Dynamics and Chaos: With Applications to Physics, Biology, Chemistry and Engineering*, volume 272. Westview Press, 2001.
- [85] J. Toomey and D. Kane. Mapping the dynamic complexity of a semiconductor laser with optical feedback using permutation entropy. *Optics express*, 22(2):1713–1725, 2014.
- [86] J. Toomey, D. Kane, S. Valling, and A. Lindberg. Automated correlation dimension analysis of optically injected solid state lasers. *Optics express*, 17(9):7592–7608, 2009.

- [87] J. P. Toomey, C. Nichkawde, D. M. Kane, K. Schires, I. D. Henning, A. Hurtado, and M. Adams. Stability of the nonlinear dynamics of an optically injected vcsel. *Optics express*, 20(9):10256–10270, 2012.
- [88] A. Uchida. *Optical communication with chaotic lasers applications of nonlinear dynamics and synchronization*. Wiley-VCH, Hoboken, N.J., 2012.
- [89] G. D. VanWiggeren and R. Roy. Communication with chaotic lasers. *Science*, 279(5354):1198–1200, 1998.
- [90] J. Weber. Amplification of microwave radiation by substances not in thermal equilibrium. *Electron Devices, Transactions of the IRE Professional Group on*, PGED-3(3):1–4, June 1953.
- [91] C. O. Weiss and R. Vilaseca. Dynamics of lasers. *NASA STI/Recon Technical Report A*, 92:39875, Nov. 1991.
- [92] J. K. White, J. Moloney, A. Gavrielides, V. Kovanis, A. Hohl, and R. Kalmus. Multilongitudinal-mode dynamics in a semiconductor laser subject to optical injection. *Quantum Electronics, IEEE Journal of*, 34(8):1469–1473, 1998.
- [93] S. Wieczorek, B. Krauskopf, and D. Lenstra. A unifying view of bifurcations in a semiconductor laser subject to optical injection. *Optics Communications*, 172(1–6):279 – 295, 1999.
- [94] S. Wieczorek, B. Krauskopf, and D. Lenstra. Mechanisms for multistability in a semiconductor laser with optical injection. *Optics Communications*, 183(1 - 4):215 – 226, 2000.
- [95] S. Wieczorek, B. Krauskopf, and D. Lenstra. Unnested islands of period doublings in an injected semiconductor laser. *Phys. Rev. E*, 64:056204, Oct 2001.
- [96] S. Wieczorek, B. Krauskopf, and D. Lenstra. Multipulse excitability in a semiconductor laser with optical injection. *Phys. Rev. Lett.*, 88:063901, Jan 2002.
- [97] S. Wieczorek, B. Krauskopf, T. Simpson, and D. Lenstra. The dynamical complexity of optically injected semiconductor lasers. *Physics Reports*, 416(1):1–128, 2005.

- [98] S. Wieczorek, T. B. Simpson, B. Krauskopf, and D. Lenstra. Bifurcation transitions in an optically injected diode laser: theory and experiment. *Optics Communications*, 215(1–3):125 – 134, 2003.
- [99] A. Wolf, J. B. Swift, H. L. Swinney, and J. A. Vastano. Determining Lyapunov exponents from a time series. *Physica D: Nonlinear Phenomena*, 16(3):285 – 317, 1985.
- [100] D. Yanson, M. Street, S. McDougall, I. Thayne, J. Marsh, and E. Avrutin. Ultrafast harmonic mode-locking of monolithic compound-cavity laser diodes incorporating photonic-bandgap reflectors. *Quantum Electronics, IEEE Journal of*, 38(1):1–11, Jan 2002.
- [101] J. Zamora-Munt, B. Garbin, S. Barland, M. Giudici, J. R. R. Leite, C. Massoller, and J. R. Tredicce. Rogue waves in optically injected lasers: Origin, predictability, and suppression. *Phys. Rev. A*, 87:035802, Mar 2013.
- [102] R. Z. Zhdanov. Separation of variables in the nonlinear wave equation. *Journal of Physics A: Mathematical and General*, 27(9):L291, 1994.